ISBN 978-82-326-1942-9 (printed version)
ISBN 978-82-326-1943-6 (electronic version)
ISSN 1503-8181

Norwegian University of
Science and Technology

Niranjan Reddy Challabotla

Doctoral Thesis

Doctoral theses at NTNU, 20XX:XXX

NTNU
Norwegian University of
Science and Technology
Faculty of Engineering Science and Technology
Department of Energy and Process Engineering

NTNU

Doctoral theses at NTNU, 2016:302

Niranjan Reddy Challabotla

Nonspherical particle suspensions in wall turbulence

Norwegian University of
Science and Technology

Niranjan Reddy Challabotla

Nonspherical particle suspensions in wall turbulence

Thesis for the degree of Philosophiae Doctor

Trondheim, November 2016

Norwegian University of Science and Technology
Faculty of Engineering Science and Technology
Department of Energy and Process Engineering

NTNU
Norwegian University of
Science and Technology

NTNU
Norwegian University of Science and Technology

Thesis for the degree of Philosophiae Doctor

Faculty of Engineering Science and Technology
Department of Energy and Process Engineering

ISBN 978-82-326-1942-9 (printed version)
ISBN 978-82-326-1943-6 (electronic version)
ISSN 1503-8181

Doctoral theses at NTNU, 2016:302

Printed by Skipnes Kommunikasjon as

Dedicated to my late mother and grandparents.

Nonspherical particle suspensions in wall turbulence

Niranjan Reddy Challabotla
Fluids Engineering Division
Department of Energy and Process Engineering
Norwegian University of Science and Technology
NO-7491 Trondheim, Norway.

Abstract

In the present PhD thesis, we investigate the dynamics of small non-spherical particles suspended in a fully developed turbulent channel flow. Non-spherical particles are approximated as axisymmetric spheroidal and triaxial ellipsoidal particles, which are characterized by their inertia and shape. As a starting point, the rotational dynamics of an inertial oblate spheroidal particle suspended in a creeping linear shear flow is investigated, which is later used in interpreting the results obtained in complex turbulent flows. The three-dimensional turbulent flow field is obtained from the Navier-Stokes equations by means of direct numerical simulation in an Eulerian reference frame. The particles are tracked using Lagrangian point particle approach. Existing methodology to simulate the prolate spheroidal particles in wall-bounded turbulent channel flow is extended to investigate the dynamics of oblate spheroidal particles and triaxial ellipsoidal particles. The effects of particle inertia, particle shape, and fluid shear on particle rotation and orientation are reported with respect to both fluid and particle reference frame. Particles at the channel center and near the wall show different rotation patterns and surprisingly different effects of particle inertia. Finally, we report the systematic investigation of the gravity force effects on the dynamics of prolate spheroidal particles.

Descriptors: Wall turbulence, Particle-laden flows, Direct numerical simulations, Spheroidal particle, Triaxial ellipsiodal particle, Orientation, Rotation, Gravity.

Contents

Preface

The research work was carried out during the period July-2013 to August-2016 at the Department of Energy and Process Engineering (EPT), NTNU, Trondheim. I gratefully acknowledge Research Council of Norway for research fellowship project no 213917/F20 (Turbulent Particle Suspensions) and NOTUR for providing high-performance computational resources.

I would like to express my sincere gratitude to my advisor, Professor Helge I. Andersson, for his constant encouragement, guidance, and support. His extensive knowledge about the subject, enthusiasm, and motivation has been invaluable for my research work. He has been extremely supportive of my ideas and granted me the academic freedom which was necessary to accomplish this work. I am also indebted to him for providing me this opportunity to be a part of his group. I wish to thank my co-supervisor Professor Lihao Zhao for his continuous encouragement, support, and insightful discussions. I am very grateful to my co-authors Dr. Christopher Nilsen and Professor Evan A. Variano for their valuable contribution. I thank Professor Greg A. Voth for writing an article *Focus on Fluids* on our published JFM paper. I also acknowledge support from COST Action FP1005, which provided me a great platform to learn and exchange research activities related to fiber suspension flows.

I would like to thank all of my friends and colleagues at EPT for many interesting discussions and for the good time we had together. Special thanks to Afshin, Fengjian, Jørgen, Rahman, Kun, Elin, Srikanth Bojja, Shareq, Rohan, Arpit, Joana, and Vipin. I thank EPT administration for providing me quick assistance whenever needed. I thank EPTraining programme for giving me an opportunity to participate in various activities. A special thanks to Pavan and Prhashanna for proof reading my thesis. I would like to express my gratitude to Indian friends and well-wishers in Trondheim, special mention to Naresh, Koti, Pavan, Ravindra, Dheeraj, Giri, Krishnam Raju, Ram Prasad, Praveen, Abhijith, Sushil, Kumar and Rajesh for making my stay as memorable and enjoyable.

I would also like to thank my friends outside Norway, scattered around the globe Pavan Kumar M, Buchi Reddy, Jaipal, Sandeep, Chaitanya, Ravi Chandar, Rama Subba Reddy, Yashwanth, Prashant, Jasim, Samson, Harish and Sandeep Reddy N for nice company. I deeply thank all my family members, and relatives for their unconditional love, encouragement, and support. I thank my grandparents and uncles for supporting me in difficult times of my life. Last but not least, I would like to thank special person in my life, my wife, Sneha, for her care, love and support during the past few years.

List of articles

The thesis is based on and contains the following research articles.

Article 1. Challabotla, Niranjan Reddy, Nilsen, Christopher & Andersson, H. I. 2015 On rotational dynamics of inertial disks in creeping shear flow. *Physics Letters A*, **379**, 157-162.

Article 2. Challabotla, Niranjan Reddy, Zhao, Lihao & Andersson, H. I. 2015 Orientation and rotation of inertial disk particles in wall turbulence. *Journal of Fluid Mechanics*, **776**, R2.

Article 3. Challabotla, Niranjan Reddy, Zhao, Lihao & Andersson, H. I. 2015 Shape effects on dynamics of inertia-free spheroids in wall turbulence. *Physics of Fluids*, **27**, 61703.

Article 4. Zhao, Lihao, **Challabotla, Niranjan Reddy**, Variano, Evan A. & Andersson, H. I. 2015 Rotation of nonspherical particles in turbulent channel flow. *Physical Review Letters*, **115**, 244501.

Article 5. Challabotla, Niranjan Reddy, Zhao, Lihao & Andersson, H. I. 2016 Gravity effects on fiber dynamics in wall turbulence. *Flow, Turbulence and Combustion*, **In press doi:10.1007/s10494-016-9742-5**, 2016.

Article 6. Challabotla, Niranjan Reddy, Zhao, Lihao & Andersson, H. I. 2016 On fiber behavior in turbulent vertical channel flow. *Chemical Engineering Science*, **153**, 75-86.

Article 7. Challabotla, Niranjan Reddy, Zhao, Lihao & Andersson, H. I. Orientation and rotation dynamics of tracer triaxial ellipsoidal particles in wall turbulence. Submitted to *Physics of Fluids.*

Appendix. Challabotla, Niranjan Reddy. 2016 Rotation of inertial triaxial ellipsoidal particles in wall turbulence.

Part of the research work have been presented by author at:

11th **Euromech Fluid Mechanics Conference.**
12 – 16 September 2016, *Seville, Spain*

68th **Annual Meeting of the APS Division of Fluid Dynamics.**
22 – 24 November 2015, *Boston, Massachusetts, USA*

8th **International Symposium on Turbulence, Heat and Mass Transfer.**
15 – 18 September 2015, *Sarajevo, Bosnia and Herzegovina*

15th **European Turbulence Conference.**
25 – 28 August 2015, *Delft, The Netherlands*

Euromech Colloquium 566,
10 – 12 June 2015, *Trondheim, Norway*

15th **MekIT'15** 8th **National Conference on Computational Mechanics.**
18 – 20 May 2015, *Trondheim, Norway*

6th **COST FP1005 Meeting and SIG43 Workshop,**
23 – 25 October 2013, *Udine, Italy*

The author has participated in following summer schools:

Regular and Irregular Non-Spherical Particles in Laminar and Turbulent Flow.
COST FP1005 Training School
27 – 29 May 2015, *Halle (Saale), Germany*

Dynamics of Particles in Flows: Fundamentals and Applications.
Nordita Summer School
2 – 27 June 2014, *Albanova, Stockholm, Sweden*

Collective Dynamics of Particles: from Viscous to Turbulent Flows.
COST FP1005 Training School
26 – 30 May 2014, *Udine, Italy*

Part 1

Summary

CHAPTER 1

Introduction

Particle-laden flows are a class of two-phase flow, in which continuous/carrier phase exchanges mass, momentum, and energy with a dispersed particle phase. These kind of flows often encountered in industrial, environmental and biological applications such as: pulp fibers in paper making processes (Lundell et al. 2011), wood fibers in biomass combustion (Ma et al. 2007), pneumatic conveying (Hilton and Cleary 2011), flakes in flow visualization (Gauthier et al. 1998), ice crystals in clouds (Shaw 2003) and phytoplankton transport in the ocean (Guasto et al. 2012). A better understanding of the complex dynamics of non-spherical particles suspended in a fluid flow is necessary to make advances in these applications. In most of these applications, the continuous fluid flow is *turbulent*, and the particle shape is *non-spherical*. Several researchers contributed to advancement of this topic in the last decade. A brief introduction to turbulence and literature review on non-spherical particles suspensions in fluid flow are described in the following sections.

1.1. Turbulence

Turbulence is a fascinating topic of discussion among fluid dynamicists. Most of the flows encountered in our everyday life are turbulent, such as: smoke rising from a cigarette or chimney; wake behind ships, car or airplane wings; flow through pipelines and currents in the atmosphere or ocean etc. Turbulence is an irregular, three-dimensional, time-dependent motion characterized by the presence of three-dimensional vorticity, chaotic, diffusive and dissipative nature. Turbulent flows are also characterized by high Reynolds numbers Re, defined as $Re = ul/\nu$, where u, l and ν are characteristic velocity, length scale and kinematic viscosity respectively. The flow is laminar below the critical value of Re. Turbulent flows can often be observed to arise from laminar flows due to instabilities. This happens because small disturbances in the flow are no longer damped by the flow, but begin to grow by taking energy from the original laminar flow. Turbulent flow occurs over a wide range of length and timescales. The turbulent energy cascade theory describes the sequential energy transfer from large eddies to smaller eddies and all the way to the smallest turbulent length scale or Kolmogorov scale where the energy is ultimately dissipated by viscosity. The mathematical description of turbulence was described independently by Navier (1822) and Stokes (1845). Due to non-linear nature of these equations, there is no general solution that exists until now. The solution to turbulence remains an open question. Nobel Laureate Richard Feynman described turbuence as *the most important unsolved problem in classical physics.* Readers are suggested to refer to the textbooks (Tennekes and Lumley 1972; Pope 2000 and Davidson 2004) for detailed understanding of the turbulent flows.

1.2. Modeling of turbulent flows

With the advent of computers, fluid dynamicists continuously developed sophisticated numerical techniques to simulate turbulent flows. Now that computers are becoming even more powerful, increasingly larger numerical simulations can be performed. Numerical simulations of turbulent flows can be broadly divided into three main categories depending on the range of scales resolved.

- *Reynolds-Averaged NavierStokes (RANS)*, flow variables are split into mean and fluctuating parts using Reynolds-decomposition. The insertion of the decomposed variables into the NavierStokes equations, followed by an averaging of the equations, give rise to the closure problem of Reynolds-stress tensor. The topic of approximating Reynolds-stress tensor resulted in the development of various turbulence models such as zero equation, one equation, two equation and Reynolds stress transport models. In RANS models, all turbulent scales are modeled. RANS models are widely used in industrial applications where the geometry and physics of the problem are complicated, and the interest is in the averaged flow variables.

- *Large Eddy Simulations (LES)*, the large scale motions of turbulent flow are computed directly, and only small scale motions are modeled by using subgrid-scale models. The results obtained using LES are more accurate compared to RANS approach, since the large eddies contain most of the turbulent energy and are responsible for most of the momentum transfer and turbulent mixing. Often LES is a compromise between RANS and Direct Numerical Simulations (DNS) approach because of the computational time, data storage requirements, and the accuracy.

- *Direct Numerical Simulations*, complete NavierStokes equations are numerically solved directly without using any turbulence model with appropriate initial and boundary conditions. DNS requires a very fine mesh and small time step to capture all the scales present in turbulent flows. The computational requirements for DNS increases approximately with $Re^{11/4}$. Therefore DNS simulations are computationally very expensive and at present can be applied only to low Reynolds number flows of the order 10^4. However, most of the real life flows have high Reynolds number, and many of these flows are impossible to solve using DNS even with the existing state-of-the-art computational resources. Currently, DNS is mostly used by academic researchers to investigate the turbulent flows over simple geometries in great detail. Readers are suggested to refer to the textbooks (Wilcox 1994; Durbin and Reif 2001; Launder and Sandham 2002 and Sagaut 2006) for detailed understanding of the modeling of turbulent flows.

1.3. Non-spherical particle suspensions

Much of the knowledge on particle-laden flows is gained via theoretical, experimental or computational work under the hypothesis of perfectly spherical particles. The assumption of spherical shape greatly simplifies the challenge of mathematical and numerical treatment of the particle behavior in flow. Spherical particles are isotropic, thus the rotational motion of the particle does not affect the translational motion. Review of the research work related to spherical particles in different kind of flows was reported by Shirolkar et al. (1996); Loth (2000); Mashayek and Pandya (2003); Guha (2008); Toschi and Bodenschatz (2009) and Balachandar and Eaton (2010). Non-spherical particles suspensions in fluid flow have received considerably less attention compared to suspensions of spherical particles. The topic of non-spherical particles in turbulent flows is quite challenging due to the complex nature of turbulence and coupling between translational and rotational motion of particles. In the literature, small non-spherical particles were often approximated by axisymmetric spheroidal particles prolate (rod-like) and Obalte (disk-like) sperodial particles.

The dynamics of an ellipsoidal particle suspended in a creeping flow was first studied by Jeffery (1922), later several researchers (Brenner 1963, 1964; Harper and Chang 1968 and Gallily and Cohen 1979) have contributed to the advancement of the theory related to the translational and rotational motion of non-spherical particles in shear flows. In all these studies Stokes-flow conditions were assumed around the particle and both the effects of the fluid and the particle inertia were thus neglected. Lin et al. (2003) summarized the work related to the dynamics of non-spherical particles in laminar shear flows. In the absence of fluid inertia, particle inertia results in a drift towards tumbling of rods with modest inertia (Subramanian and Koch 2005 and Lundell and Carlsson 2010) whereas spinning was observed for heavy rods (Nilsen and Andersson 2013). Computer simulations using a lattice Boltzmann method were used to identify different rotational states of a spheroidal particle as a function of the particle Reynolds number (Qi and Luo 2003; Yu et al. 2007; Huang et al. 2012 and Rosén et al. 2014). Recently, Rosén et al. (2015) and Rosén et al. (2016) reported the different rotational states observed for a prolate spheroidal particle due to the combined effects of fluid and particle inertia.

The dynamics of non-spherical particles in homogeneous isotropic turbulence have been explored by experimental investigations (Bellani et al. 2012; Parsa et al. 2012 and Ni et al. 2015) and computational studies (Fan and Ahmadi 1995; Olson 2001; Shin and Koch 2005; Gustavsson et al. 2014; Marcus et al. 2014; Ni et al. 2014 and Byron et al. 2015). It has been shown that non-spherical particles preferentially align with respect to fluid vorticity and/or strain, which causes particle rotation to differ from that of fluid parcels, even though the particles are non-inertial. Rod-like particles preferentially align with the fluid vorticity vector and the vorticity component along the rod axis does not contribute to their tumbling. In contrast to the rod-like particles, disk-like particles align perpendicular to the fluid vorticity vector and this preferential orientation results in higher tumbling rates. In other words, *rods spin and disks tumble* (Byron et al. 2015). The Lagrangian fluid stretching in turbulence aligns the major axis of an anisotropic particle with the fluid vorticity (Ni et al. 2014). The variance of the total rotation rate of a spheroidal particle is almost independent of the particle shape (Byron et al. 2015). Strong effects of particle shape on tumbling and spinning were reported for small deviations from spherical shape. Orientation statistics, settling velocities (Siewert et al. 2014a) and collision rates (Siewert et al. 2014b) of inertial spheroids in decaying isotropic turbulence were reported.

Direct numerical simulations of the turbulent flow field coupled with a Lagrangian point-particle tracking methodology were successfully employed by different research groups to investigate the dynamics of non-spherical inertial particles in wall-bounded turbulent flows. The modelling of the translation and rotational motion of the rigid spheroidal particles relies on the analytical expressions for drag force (Brenner 1964) and torque (Jeffery 1922). These expressions were derived based on the assumption of Stokes flow conditions in the vicinity of the particle. Zhang et al. (2001), and later followed by several others (Mortensen et al. 2008; Marchioli et al. 2010; Zhao and Wachem 2013; Zhao et al. 2014) focused on the orientation, transport, and deposition of rod-like particles suspended in a turbulent channel flow over a wide range of particle parameters. The particle inertia resulted in accumulation of particles in the near-wall region and preferential concentration in the low-speed streaks. Particles in the near-wall region moreover tended to preferentially orient themselves in the streamwise direction and this tendency increased with aspect ratio. Yin et al. (2003) developed a methodology for modelling the dynamics of non-spherical particles in flows by assuming shape and orientation dependent drag and lift-force correlations, which is valid beyond the Stokes flow regime. Later this methodology along with Large-eddy simulations techniques has been adopted by Njobuenwu and Fairweather (2014, 2015, 2016) to investigate the influence of a wide range of particle shapes and inertia on the translational and rotational behavior of spheroidal particles in wall-bounded turbulent flows. Experimental studies on non-spherical particles in wall-bounded turbulent flows are scarce (Abbasi Hoseini et al. 2015). The readers are suggested to refer to the special journal issue on anisotropic particles (Andersson and Soldati 2013), and review article by Voth and Soldati (2017), which reports the state-of-the-art on anisotropic particles in turbulent flows.

Particle-resolved simulations using an immersed boundary method for finite-sized spherical particles (Lucci et al. 2010 and Uhlmann 2008) and Lattice Boltzmann method for spheroidal particles (Do-Quang et al. 2014) have recently emerged. At present these computationally expensive approaches are unable to handle suspensions of millions of small size particles, as often required to obtain reliable particle statistics in turbulent flows.

1.4. Objectives

The main goal of the PhD work is to extend the knowledge of the small non-spherical particles suspended in wall turbulence by using Direct numerical simulations coupled with Lagrangian point particle tracking method. We explored the effects of particle inertia, particle shape, and fluid shear on orientaional and rotational dynamics of axisymmetric spheroidal and triaxial ellipsoidal particles.

CHAPTER 2

Governing equations and numerical methods

The Eulerian-Lagrangian methodology is adopted to simulate the particle-laden turbulent channel flow. The flow field is obtained by direct numerical simulations (DNS) of the Navier-Stokes equations in an Eulerian framework. The non-spherical particles are tracked in a Lagrangian framework using a point particle approach.

2.1. Fluid flow

In the present work, fully developed turbulent channel flow is considered. Turbulent channel flow is one of the canonical wall-bounded flows, together with turbulent pipe and boundary layer flow. The fluid flow is assumed to be incompressible, Newtonian and isothermal which is governed by the mass and momentum conservation equations,

$$\frac{\partial u_i}{\partial x_i} = 0 \tag{2.1}$$

$$\frac{\partial u_i}{\partial t} + u_j \frac{\partial u_i}{\partial x_j} = -\frac{\partial p}{\partial x_i} + \frac{1}{\mathrm{Re}_\tau} \frac{\partial^2 u_i}{\partial x_j \partial x_j} \tag{2.2}$$

where u_i is the i^{th} component of the velocity vector, $\partial p/\partial x_i$ is pressure gradient that drives the flow and $Re_\tau = u_\tau h/\nu$ is the Reynolds number based on the shear velocity, u_τ , and on the half channel height, h. The variables in equation (2.1) and (2.2) are normalized by the viscous scale for velocity (u_τ), length (ν/u_τ), and time (ν/u_τ^2).

2.1.1. *Numerical methodology*

A pseudo-spectral DNS code is used to simulate the fully developed turbulent channel flow. The code is written in FORTRAN language, and it was originally developed at TU Delft by Prof. Boersma and Dr. Gillessen and later developed in Prof. Helge I. Andersson's group at NTNU (Mortensen 2007 and Zhao 2011).

The channel flow geometry is shown in Figure (2.1) with dimensions $L_x = 12h$; $L_y = 6h$ and $L_z = 2h$ in streamwise (x), spanwise (y) and wall-normal (z) directions, respectively. Periodic boundary conditions are imposed in homogeneous streamwise and spanwise directions. No-slip boundary conditions are imposed at the channel walls (at $z = 0$ and $2h$). The flow is driven by a constant pressure gradient in the streamwise direction, which ensures that the mass flux through the channel remains constant. Frictional Reynolds number of the flow $Re_\tau = 180$. More recently, DNS of higher Reynolds number turbulent channel flow was reported by Lee and Moser (2015) up to $Re_\tau \approx$5200.

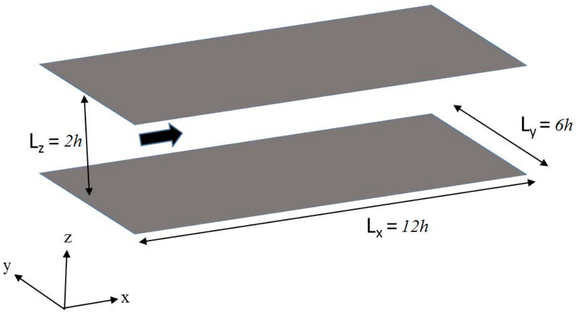

FIGURE 2.1. Geometry of the channel flow computational domain.

The computational domain is discretized with N_x= 192, N_y= 192 and N_z=192 grid points in x, y and z directions, respectively. Staggered grid system is used in the present code with velocity components u, v and pressure p are imposed at the cell center and the velocity component w is defined at the cell-face center. Grid resolution in the streamwise and spanwise directions are Δx^+=11.3 and Δy^+=5.6. Non-uniform mesh is adopted in the wall-normal direction using hyperbolic tangent stretching function. The first mesh point away from the wall is at $z^+ = 0.9$, and the maximum spacing at the centerline of the channel is 2.86 wall units. The time step used is $\Delta t^+ = 0.036$.

In the homogeneous streamwise and spanwise directions, spatial derivatives are computed with a pseudo-spectral method by transforming variables into spectral space, using Fourier series representation. For example, the velocity vector u_i can be expressed as ,

$$u_i(x_i, t) = \sum_k \hat{u}_k(t) e^{ikx_i} \tag{2.3}$$

where $x_i = (x,\, y,\, z)$ is the position vector in physical space and $k = (k_x,\, k_x,\, z)$ is the wave number in spectral space. In spectral space, the first and second derivatives for example in the streamwise direction are determined by multiplying the transformed terms with ik_x and $-k_x^2$. The computed derivatives in spectral space are then transformed back into the physical space. In the wall-normal direction, the derivatives are computed by a second-order central finite difference method.

The Navier-Stokes equations (2.2) are advanced in time with a standard second-order explicit Adams-Bashforth scheme. Standard projection method is used to enforce the mass conservation, which is summarized as,

Step 1: Time integration of the Navier-Stokes equations (2.2) gives

$$\frac{{u_i}^{n+1} - {u_i}^n}{\Delta t} = \frac{3}{2} T({u_i}^n) - \frac{1}{2} T({u_i}^{n-1}) - \frac{\partial p^{n+1}}{\partial x_i}, \tag{2.4}$$

where $T({u_i}^n) = -{u_j}^n \frac{\partial {u_i}^n}{\partial x_j} + \frac{1}{\mathrm{Re}_\tau} \frac{\partial^2 {u_i}^n}{\partial x_j \partial x_j}$

Step 2: Compute the intermediated velocity u_i^* at time between t^n and t^{n+1} by neglecting pressure p^n as,

$$\frac{{u_i}^* - {u_i}^n}{\Delta t} = \frac{3}{2}T({u_i}^n) - \frac{1}{2}T({u_i}^{n-1}) \tag{2.5}$$

Step 3: The difference between equations (2.4) and (2.5) gives,

$${u_i}^{n+1} - {u_i}^* = -\Delta t \frac{\partial p^{n+1}}{\partial x_i} \tag{2.6}$$

Step 4: By applying the divergence of the above equation and the continuity equation at the new time level, which results in pressure Poisson equation

$$\nabla^2 p^{n+1} = \frac{\rho \nabla . u^*}{\Delta t}. \tag{2.7}$$

The above equation (2.7) is solved by using fast Fourier transform (FFT) in the homogeneous directions and with tridiagonal matrix algorithm in the wall-normal direction. After computing the pressure at new time level p^{n+1}, equation (2.4) is solved to obtain the velocity at the new time level ${u_i}^{n+1}$.

2.2. Particle dynamics

This section describes the governing equations and numerical methods for simulating the dynamics of non-spherical particles suspended in turbulent channel flow. Particles are tracked at each time step in Lagrangian framework by computing forces and torques acting on the particle. The point-particle methodology is adopted which can be justified for particle size smaller than the Kolmogorov length scale of the fluid flow, such that the neighboring fluid flow can be assumed as Stoksian or creeping flow. Hence, the particle Reynolds number should satisfy the following criteria:

$$\mathrm{Re}_p = \frac{|u_i - v_i|\, d}{\nu} < 1 \tag{2.8}$$

where, $(u_i - v_i)$ is the slip-velocity, defined as the difference between local fluid (u_i) and particle (v_i) velocity, d is the characteristic particle size. In the literature, there exist analytical expressions for different forces and torques acting on the particles suspended in Stokes flow conditions. These expressions can be utilized to compute the particle dynamics by coupling with direct numerical simulations of fluid flow without actually resolving the particle.

In the present work, non-spherical particles are represented as axisymmetric spheroidal particles as shown in Figure 2.2. A spheroidal particle with three semi-axes a, b and c is characterized by aspect ratio defined as $\lambda = c/a$ which distinguishes between prolate $(\lambda > 1)$ and oblate $(\lambda < 1)$ spheroids, whereas $\lambda = 1$ corresponds to an isotropic particle, i.e. a sphere. Governing equations and methodology for modeling of spheroidal particles is discussed in the following section. Generalization of this methodology to triaxial ellipsoids is described in article 7 and appendix 1.

Three different Cartesian coordinates are introduced to describe the particle dynamics as shown in Figure 2.3. The inertial frame $x_i = < x,\ y,\ z >$ is used to

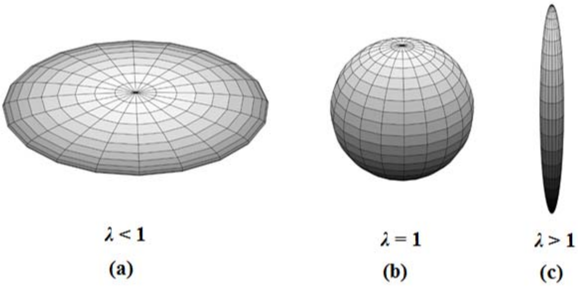

FIGURE 2.2. Spheroidal particles (a) oblate (or disk-like), (b) sphere and (c) prolate (or rod-like).

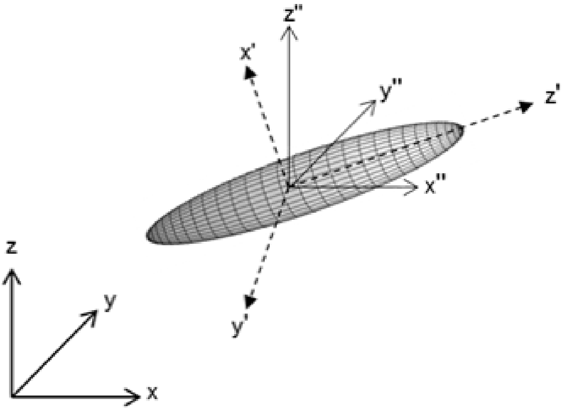

FIGURE 2.3. Cartesian coordinate systems: inertial frame x, particle frame x', and co-moving frame x''.

describe the continuous fluid flow and the translational motion of the particle. The particle frame $x_i' = < x', y', z' >$ with its origin at the particle mass center and aligned with principal axes is used to describe the particle rotational motion. The co-moving frame $x_i'' = < x'', y'', z'' >$ with its origin coinciding with that of the particle frame and its axes being parallel to the corresponding axes of the inertial frame. Euler angles (ϕ, θ, ψ) are used to represent the orientation of the particle. The transformation between the co-moving and the particle frame of reference is given by the rotational matrix R_{Eul} as (Goldstein 1980):

$$x_i' = R_{Eul} x_i'' \tag{2.9}$$

where the rotational matrix R_{Eul} is given by

$$R_{Eul} = \left[\begin{array}{ccc} \cos\psi\cos\varphi - \cos\theta\sin\varphi\sin\psi & \cos\psi\sin\varphi + \cos\theta\cos\varphi\sin\psi & \sin\psi\sin\theta \\ -\sin\psi\cos\psi - \cos\theta\sin\varphi\cos\psi & -\sin\psi\sin\varphi + \cos\theta\cos\varphi\cos\psi & \cos\psi\cos\theta \\ \sin\theta\sin\varphi & -\sin\theta\cos\varphi & \cos\theta \end{array} \right]. \tag{2.10}$$

Euler parameters or quaternions are introduced to avoid singularities (Goldstein 1980),

$$\begin{aligned} e_0 &= \cos\tfrac{(\psi+\varphi)}{2}\cos\tfrac{\theta}{2}, \\ e_1 &= \cos\tfrac{(\psi-\varphi)}{2}\sin\tfrac{\theta}{2}, \\ e_2 &= \sin\tfrac{(\psi-\varphi)}{2}\sin\tfrac{\theta}{2}, \\ e_3 &= sin\tfrac{(\psi+\varphi)}{2}\cos\tfrac{\theta}{2}. \end{aligned} \tag{2.11}$$

The Euler parameters are dependent and should satisfy the following constraint

$$e_0^2 + e_1^2 + e_2^2 + e_3^2 = 1. \tag{2.12}$$

The transformation matrix R_{Eul} in equation (2.10) can be rewritten in terms of Euler parameters

$$R_{Eul} = \left[\begin{array}{ccc} e_0^2 + e_1^2 - e_2^2 - e_3^2 & 2\left(e_1e_2 + e_0e_3\right) & 2\left(e_1e_3 - e_0e_2\right) \\ 2\left(e_1e_2 - e_0e_2\right) & e_0^2 - e_1^2 + e_2^2 - e_3^2 & 2\left(e_2e_3 + e_0e_1\right) \\ 2\left(e_1e_3 + e_0e_2\right) & 2\left(e_2e_3 - e_0e_1\right) & e_0^2 - e_1^2 - e_2^2 + e_3^2 \end{array} \right]. \tag{2.13}$$

2.2.1. *Translational Dynamics*

The generalized equation governing the motion of a rigid spherical particle in an unsteady non-uniform flow at low Reynolds number is given by Maxey and Riley (1983) as,

$$\begin{aligned} m_p\tfrac{dv_i}{dt} = (m_p - m_F)g\delta_{x,i} + m_F\tfrac{Du_i}{Dt} - \tfrac{1}{2}m_F\tfrac{d}{dt}\left\{(v_i - u_i) - \tfrac{a^2}{10}\nabla^2 u_i\right\} \\ -6\pi a\mu\left\{(v_i - u_i) - \tfrac{a^2}{6}\nabla^2 u_i\right\} - 6\pi a^2\mu\int_0^t \frac{\frac{d}{dt}\left\{(v_i - u_i) - \frac{a^2}{6}\nabla^2 u_i\right\}}{[\pi\nu(t-\tau)]^{1/2}}d\tau \end{aligned} \tag{2.14}$$

where v_i is the velocity of the particle, u_i is the undisturbed velocity of the fluid, g is gravitational acceleration, m_F is the mass of displaced fluid, μ is the dynamic viscosity and ν is the kinematic viscosity of the fluid. Right-hand side of the equation (2.14) represents the five different kinds of fluid forces acting on the particle, from left to right are: gravity and buoyancy force, pressure gradient force, added mass force, Stokes drag force, and Basset history force. The similar generalized equation as (2.14) is not yet known for non-spherical particle. In case of gas-solid flows with high particle-to-fluid density ($\rho_p/\rho_f >> 1$), only Stokes drag force and gravity forces are dominant, and we can neglect all other forces in the equation .

Unlike a spherical particle, the translational and rotational motion of spheroidal particles are strongly coupled through its orientation. The translational motion of a single spheroidal particle is governed by,

$$m_p\frac{dv_i}{dt} = \pi\mu a K_{ij}\,\Delta u_j \pm \left(1 - \frac{1}{D}\right)m_p g\delta_{x,i} \tag{2.15}$$

where $\Delta u_j = u_j - v_j$ is the slip velocity defined as the difference between fluid velocity u_j at the particle location and the particle velocity v_j, m_p is the particle mass, $D = \rho_p/\rho_f$ is the ratio between the particle and fluid densities, and K_{ij} is the resistance tensor defined in the inertial frame of reference which is related to the resistance tensor K'_{ij} in the particle frame of reference as $K_{ij} = R^T_{Eul} K'_{ij} R_{Eul}$. K'_{ij} is a diagonal matrix with its elements given by Gallily and Cohen (1979) and Siewert et al. (2014a) as shown in Table 2.1, which are uniquely determined by the particle geometry. The first term on the right-hand side of equation (2.15) represents the hydrodynamic drag force from the surrounding fluid acting on a spheroidal particle as derived by Brenner (1964). This expression for the drag force is valid only when the particle Reynolds number Re_p is low, such that the force acting on the particle is linearly dependent on the slip velocity Δu_j. The second term in equation (2.15) represents the gravity and buoyancy forces.

TABLE 2.1. Analytical expressions for resistance tensor components

	$\lambda < 1$	$\lambda = 1$	$\lambda > 1$
$k_{x'x'} = k_{y'y'}$	$\frac{32\pi a\sqrt{(1-\lambda^2)}^3}{(3-2\lambda^2)(\pi-C)-2\lambda\sqrt{(1-\lambda^2)}}$	$6\pi a$	$\frac{16\pi a\sqrt{(\lambda^2-1)}^3}{(2\lambda^2-3)\ln\left(\lambda+\sqrt{(\lambda^2-1)}\right)+\lambda\sqrt{(\lambda^2-1)}}$
$k_{z'z'}$	$\frac{16\pi a\sqrt{(1-\lambda^2)}^3}{(1-2\lambda^2)(\pi-C)+2\lambda\sqrt{(1-\lambda^2)}}$	$6\pi a$	$\frac{8\pi a\sqrt{(\lambda^2-1)}^3}{(2\lambda^2-1)\ln\left(\lambda+\sqrt{(\lambda^2-1)}\right)-\lambda\sqrt{(\lambda^2-1)}}$

where $C = 2tan^{-1}\left(\lambda\left(1-\lambda^2\right)^{-1/2}\right)$.

The translational displacement of the particle at each time step is determined by

$$\frac{dx_i}{dt} = v_i \tag{2.16}$$

2.2.2. *Rotational Dynamics*

The rotational motion of the particle is governed by Euler's equations expressed in the particle frame of reference

$$I'_{ij}\frac{d\omega'_j}{dt} + \epsilon_{ijk}\omega'_j I'_{kl}\omega'_l = N'_i \tag{2.17}$$

where ω'_i is the angular velocity of the particle and I'_{ij} is the moment of inertia tensor. For spheroidal particles, moment of inertia components along the principal axes of the particle are

$$I'_{xx} = I'_{yy} = \frac{\left(1+\lambda^2\right)ma^2}{5};\; I'_{zz} = \frac{2ma^2}{5}. \tag{2.18}$$

The torque components N'_i for a triaxial ellipsoidal particle in creeping shear flow originally derived by Jeffery (1922) and simplify for a spheroid to

$$\begin{aligned} N'_x &= \tfrac{16\pi\mu a^3\lambda}{3(\beta_0+\lambda^2\gamma_0)}\left[\left(1-\lambda^2\right)S'_{yz}+\left(1+\lambda^2\right)\left(\Omega'_x-\omega'_x\right)\right] \\ N'_y &= \tfrac{16\pi\mu a^3\lambda}{3(\alpha_0+\lambda^2\gamma_0)}\left[\left(\lambda^2-1\right)S'_{xz}+\left(1+\lambda^2\right)\left(\Omega'_y-\omega'_y\right)\right] \\ N'_z &= \tfrac{32\pi\mu a^3\lambda}{3(\alpha_0+\beta_0)}\left(\Omega'_z-\omega'_z\right). \end{aligned} \tag{2.19}$$

Here, S'_{ij} and Ω'_i denote the fluid rate-of-strain tensor and rate-of-rotation vector, defined as

$$\begin{aligned} S'_{yz} &= \tfrac{1}{2}(u'_{z,y}+u'_{y,z}) \\ S'_{xz} &= \tfrac{1}{2}(u'_{x,z}+u'_{z,x}) \end{aligned} \qquad \begin{aligned} \Omega'_x &= \tfrac{1}{2}(u'_{z,y}-u'_{y,z}) \\ \Omega'_y &= \tfrac{1}{2}(u'_{x,z}-u'_{z,x}) \\ \Omega'_z &= \tfrac{1}{2}(u'_{y,x}-u'_{x,y}) \end{aligned}$$

The analytically derived expressions for shape factors α_0, β_0, and γ_0 for spheroidal particle were shown in Table 2.2 (Gallily and Cohen 1979 and Siewert et al. 2014a).

Table 2.2. Analytical expressions for shape factors

	$\lambda < 1$	$\lambda = 1$	$\lambda > 1$
$\alpha_0 = \beta_0$	$\frac{-\lambda}{2\sqrt{(1-\lambda^2)}^3}\left(C-\pi+2\lambda\sqrt{(1-\lambda^2)}\right)$	$\frac{2}{3}$	$\frac{\lambda^2}{\lambda^2-1}+\frac{\lambda}{2\sqrt{(\lambda^2-1)}^3}K$
γ_0	$\frac{1}{\sqrt{(1-\lambda^2)}^3}\left(\lambda C-\lambda\pi+2\sqrt{(1-\lambda^2)}\right)$	$\frac{2}{3}$	$-\frac{2}{\lambda^2-1}-\frac{\lambda}{\sqrt{(\lambda^2-1)}^3}K$

where $K = ln\left(\frac{\lambda-\sqrt{(\lambda^2-1)}}{\lambda+\sqrt{(\lambda^2-1)}}\right)$.

Time rate of change of the Euler parameters is related to the particle angular velocity and represented as

$$\begin{pmatrix} \dot{e}_0 \\ \dot{e}_1 \\ \dot{e}_2 \\ \dot{e}_3 \end{pmatrix} = \frac{1}{2}\begin{pmatrix} e_0 & -e_1 & -e_2 & -e_3 \\ e_1 & e_0 & -e_3 & e_2 \\ e_2 & e_3 & e_0 & -e_1 \\ e_3 & -e_2 & e_1 & e_0 \end{pmatrix}\begin{pmatrix} 0 \\ \omega'_x \\ \omega'_y \\ \omega'_z \end{pmatrix} \tag{2.20}$$

In summary, the dynamics of the spheroidal particle is completely described by solving thirteen coupled equations: three for translational velocity (equation 2.15), three for angular velocity (equation 2.17), three for particle position (equation 2.16), and four for particle orientation (equation 2.20). These equations are solved at each time step along with the integration of the Navier-Stokes equations.

2.2.3. *Particle response time*

The ability of an inertial particle to adjust to the ambient flow field can be estimated in terms of a particle response time τ_p. Shapiro and Goldenberg (1993) introduced a translational relaxation time based on the assumption of isotropic particle orientation. Later this time scale has been adopted by Marchioli et al. (2010); Mortensen et al. (2008) and other researchers. In the present work, we have derived expression for disk-like particles. By means of the elements of the translational resistance tensor in Table 2.1, we obtain expressions for particle response time,

$$\begin{aligned}
\tau_{p,\,prolate} &= 2\pi a\lambda \left(\frac{(\pi - K)\left(1-\lambda^2\right)}{16\pi a \sqrt{(1-\lambda^2)}^3} \right) \frac{2Da^2}{9\nu}; \\
\tau_{p,\,oblate} &= \frac{2Da^2}{9\nu} \frac{\lambda(\pi - C)}{2\sqrt{(1-\lambda^2)}}.
\end{aligned} \tag{2.21}$$

A Stokes number St is then be defined as the ratio between the particle response time τ_p and the viscous timescale $\tau_v = \nu/u_\tau^2$ and thus representative of the near-wall turbulence.

2.2.4. *Numerical Methodology*

The translational (equation 2.15) and rotational (equation 2.17) equations of the particle motion are solved using a mixed differencing procedure (Fan and Ahmadi 1995). Particle position and orientation are updated using a second-order Adams-Bashforth scheme. Time step size used during the integration of the particle equations is the same as that used in Navier-Stokes equations. The velocity field at particle location is obtained by means of a second-order quadratic interpolation scheme. The particle boundary conditions are periodic in the two homogeneous directions. Particle-wall collisions are fully elastic, similar to the collision model adopted by Mortensen et al. (2008); Marchioli et al. (2010) and Zhao et al. (2014). This implies that particle keeps its linear and angular momentum in the homogeneous directions upon touching the wall. A collision is defined to occur every time that the distance from the center of mass of a spheroid to the closest wall becomes less than the semi-axis a. It is also assumed that the particle suspension is sufficiently dilute that one-way coupled simulations can be justified and particle-particle collisions are rare and therefore neglected. The size of the spheroids does not exceed the Kolmogorov length scale. The assumption of Stokes flow in the immediate vicinity of a particle, on which the expressions for the force and torque components in equation (2.15) and equation (2.17) are based, can thus be justified.

2.3. Parallelization of Computer Code

The current FORTRAN computer code is parallelized by using the Message Passing Interface (MPI). The computational domain is divided into slices in the wall-normal direction, and the derivatives were computed by communicating the variables to the adjacent slices. Furthermore, the computational domain in the streamwise direction is also divided into slices to solve the Fourier transformed Poisson equation. The total number of particles tracked is divided equally between the processors, i.e. each processor computes the same amount of particles. Simulations were performed using 64 processors on NOTUR super computers Vilje and Stallo.

CHAPTER 3

Summary of articles

This chapter presents a brief summary of the main findings reported in seven appended articles and appendix. Outline of the scientific articles is shown in Figure 3.1.

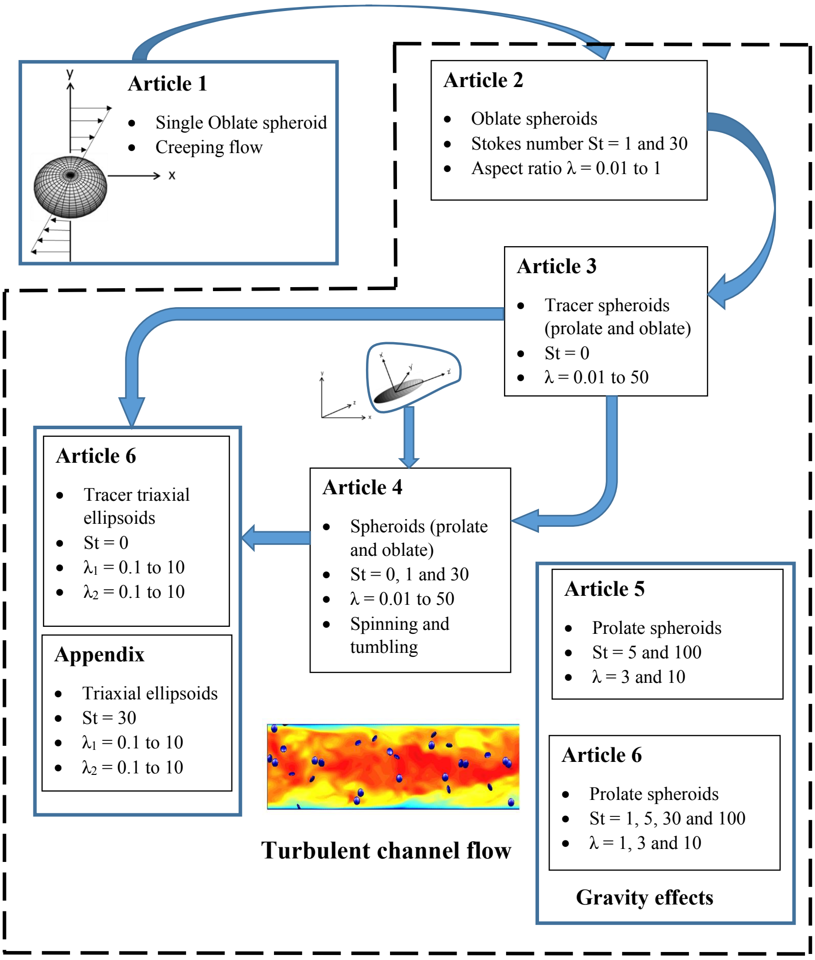

FIGURE 3.1. Outline of the scientific articles.

Article 1

On rotational dynamics of inertial disks in creeping shear flow.

Niranjan Reddy Challabotla, Christopher Nilsen & Helge I. Andersson

In this paper, rotational dynamics of single oblate spheroidal or disk-like particle suspended in creeping shear flow has been investigated over a wide range of particle aspect ratios and Stoke numbers. Nonlinear coupled ODEs governing the particle motion are solved using MATLAB. A shape-dependent time scale is proposed for rotation of an oblate spheroid about its symmetric axis in the flow gradient plane. Irrespective of the particle aspect ratio, Stokes number, and initial orientation, an oblate spheroid finally reaches a steady state rotation in flow-gradient plane. Two qualitatively different stages were observed during the drift of the orientation of the rotation axis towards the fluid vorticity vector. First, the wobbling drift towards rotation in the velocity-gradient plane becomes slower with increasing particle inertia, except for the least inertial spheroids. The duration of the second stage, during which the spheroid spins up to match the fluid angular velocity, becomes independent of the aspect ratio for relatively flat particles. This work is also a starting point for understanding the dynamics of oblate spheroidal particles suspended in wall-bounded turbulent flows, which is the topic of article 2.

Article 2

Orientation and rotation of inertial disk particles in wall turbulence.

Niranjan Reddy Challabotla, Lihao Zhao & Helge I. Andersson

In the literature, vast majority of studies have focused on rod-like particles due to their relevance in many applications. In contrast, investigations of the dynamics of disk-like particles are scarce. This motivated us to work on this topic. Numerical methodology was developed and implemented in the existing in-house FORTRAN code to simulate the disk-like particles. The methodology was validated by comparing results in creeping shear flow reported in article 1. The orientation and rotational dynamics of inertial oblate spheroids suspended in a fully developed turbulent channel flow have been explored. Strong influence of the particle shape was observed on the orientation and rotation of light inertial particles with $St = 1$ and this effect was damped as the particle inertia increased to $St = 30$. The symmetry axis of the inertial disk-like particles exhibited a strong preferential alignment with the mean fluid vorticity vector or spanwise direction in the near-wall region which was qualitatively different from the preferred orientation of rod-like particles in the streamwise direction. This article was selected as *Focus on Fluid Article in JFM.*

Article 3

Shape effects on dynamics of inertia-free spheroids in wall turbulence.

Niranjan Reddy Challabotla, Lihao Zhao & Helge I. Andersson

Strong shape effects observed on the dynamics of low inertial disk-like particles at $St = 1$ reported in article 2 and the earlier results reported in the literature for rod-like particles motivated us to work on this topic. This article reported results for inertia-free spheroidal particles suspended in a turbulent channel flow. Although the inertia-free spheroids passively translate along with the fluid, the particle orientation and rotation strongly depend on the particle shape. A wide range of aspect ratios from $\lambda = 0.01$ to 50, i.e., from flat disks to long rods, are covered for the first time in order to provide a comprehensive coverage of the shape effects on the particle dynamics. The flattest disks were strongly aligned in the wall-normal direction, whereas the longest rods aligned themselves with the wall. The strong mean spanwise spin observed for spherical particles ($\lambda = 1$) decreased with increasing asphericity both for rod-like and disk-like spheroids. The substantial reduction of the mean spin of spheroids with high asphericity was attributed to Jeffery-like orbiting.

Article 4

Rotation of nonspherical particles in turbulent channel flow.

Niranjan Reddy Challabotla, Lihao Zhao, Helge I. Andersson & Evan A. Variano

This work is a major step forward in understanding of the complex dynamics of non-spherical particle suspensions in wall-bounded turbulent flows. In this article, we investigated the dynamics of spheroidal particles in particle reference frame. Channel flow allowed us to examine the transition in behavior from nearly isotropic turbulence at the channel center to highly sheared anisotropic turbulence near the channel wall. In the channel center, we have found that inertia-free spheroids were tumbling and spinning just as in homogeneous isotropic turbulence, whereas inertia reduced the preferential spinning or tumbling and led to a more isotropic rotation. Spheroids in the wall region were affected both by mean shear and anisotropic fluid vorticity, and their rotational behavior is totally different from at channel center.

Article 5 & Article 6

Gravity effects on fiber dynamics in wall turbulence.
On fiber behavior in turbulent vertical channel flow.

Niranjan Reddy Challabotla, Lihao Zhao & Helge I. Andersson

In article 5 & 6, we investigated the dynamic behavior of inertial rod-like particles or fibers suspended in a turbulent vertical channel flow. Gravity is inevitably present in all industrial applications and experimental studies, but in most of the computational investigations reported in the literature ignored the gravity force. This motivated us to simulate fiber suspensions in the downward and upward flow configurations and compare with results from channel flow simulations in which gravity is neglected. Article 5 consists of preliminary results for $St = 5$ and 100. Results were reported for gravity effects on the fiber orientations, velocities, and slip velocities. This work was initially presented at THMT-2015 conference and later published as an invited paper in a special issue of FTAC journal. Detailed results including more Stokes numbers and comparison with spherical particles were reported in article 6. In article 5, we have fixed the particle size and varied the particle density to keep Stokes number as constant (see equation 2.21) and opposite approach was adopted in article 6 which is more realistic when considering the gravity force. However, the difference between results obtained by both methods is negligible. The results showed that gravity has a negligible effect for fibers with modest inertia, i.e. low Stokes numbers, whereas gravity turned out to have a major impact on the dynamics of highly inertial fibers. Irrespective of the bulk flow direction, a preferential alignment of the inertial fibers with the gravity force was found in the channel center where fibers have been known to orient randomly in absence of gravity. In the downward channel flow, the drift velocity of the fibers towards the walls was substantially higher for fibers than for spheres and also higher than when gravity was neglected. In the upward flow configuration, the modest drift velocity of inertial spheres was totally quenched for all fibers irrespective of shape.

Article 7

Orientation and rotation dynamics of tracer triaxial ellipsoidal particles in wall turbulence.

Niranjan Reddy Challabotla, Lihao Zhao & Helge I. Andersson

In this article, we extended the methodology used in article 3 to investigate the dynamics of more general triaxial ellipsoidal particles suspended in wall-bounded turbulent flows. The triaxial ellipsoids were characterized by two independent shape parameters λ_1 and λ_2 that both were varied from 0.1 to 10. The tumbling rates observed in the channel center closely resembled tumbling of triaxial ellipsoids in homogeneous isotropic turbulence. The particle enstrophy turned out to be almost independent of particle shape. In the near-wall region, however, the particle enstrophy was highest for spherical particles and diminished with increasing asphericity. The reduction of the enstrophy was by far more pronounced for triaxial ellipsoids than for axisymmetric particles. We also inferred that triaxial ellipsoids exhibited a dual nature, namely tumbling like a disk about one axis and as a rod about another axis.

Appendix 1

Rotation of inertial triaxial ellipsoidal particles in wall turbulence.

Niranjan Reddy Challabotla

The main objective of this appendix was to extend the present numerical code to simulate the inertial triaxial ellipsoidal particles suspended in fully developed turbulent channel flow. This work represents a generalization of our earlier simulations on axisymmetric particles and aims to uncover the influence of triaxiality on the particle dynamics. Simulations were performed for wide range of particle shapes and fixed Stokes number St = 30. Statistics for rotation rates of particles were reported.

CHAPTER 4

Conclusions

4.1. Summary

- The present thesis contributed to advancing the knowledge of small-non spherical particles suspended in wall turbulence by addressing some of the open questions in this research community.

- DNS coupled with Lagrangian point particle methodology adopted in the present work is successful in obtaining reliable statistics for dynamics of ellipsoidal particle suspensions in a fully developed turbulent channel flow. First time, this methodology has been extended to study the dynamics of disk-like (article 2) and more general triaxial particles (article 7). Results obtained for particles in channel center are in close agreement with the experimental measurements reported by Parsa et al. (2012) and other computational investigations for homogeneous isotropic turbulence.

- In the near-wall region, inertia-free disk-like particles exhibited preferential alignment with the wall-normal direction whereas inertial disk-like particles aligned preferentially with the spanwise direction. Preferential alignment of inertial disk-like particles is consistent with our finding in article 1 that a single inertial disk-like particle in uniform shear flow ultimately rotates in flow gradient plane. The preferential alignment of these particles combined with the strong velocity gradients in the near-wall region resulted in interesting rotational statistics: mean spanwise rotation of inertia-free particles is damped, whereas inertial particles attained rotation rate which almost equal to mean fluid rotation. The particle aspect ratio has a strong influence on the dynamics of inertia-free particles and this has been diminished for inertial particles.

- In the near-wall region, spheroidal particle rotation is affected both by mean shear and anisotropic fluid vorticity, and their rotational behavior is totally different from at channel center. Particle enstrophy is independent of the particle aspect ratio in channel center, however, near-wall particle enstrophy is strongly dependent on shape with lower particle enstrophy as the particle asphericity increases.

- In the channel center region, all particles approached an isotropic orientation irrespective of the particle aspect ratio and inertia. Preferential tumbling for disks and spinning for rods has been observed similar to homogeneous isotropic turbulence, whereas inertia damped the preferential tumbling or spinning and led to a more isotropic rotation.

- The present work reported in article 5 & 6 strongly suggested that the actual gravity configuration might play an important role in the distribution of particles across the channel.

- The dynamics of triaxial tracer particles is similar to that of disk-like particles in a certain direction, but resembles that of rod-like particles in another direction in both the Lagrangian particle frame and in the Eulerian laboratory frame, but the underlying physical mechanisms are different. The strong alignment of the major axis in the streamwise direction and of the minor axis in the wall-normal direction in the near-wall region resulted in a substantial reduction of the mean angular rotation rate.

4.2. Future work

- In our work, only the drag and gravity forces were considered. Development of reliable models for other forces acting on the non-spherical particle such as lift, added mass, and basset-history force can be an important research topic.

- We adopted drag force correlation which is valid strictly in the Stoke regime i.e. $Re_p < 1$. Recently, some attempts have been made to establish reliable correlations for the drag force and torque on spheroidal particles (Hölzer and Sommerfeld 2008; Ouchene et al. 2015 and Zastawny et al. 2012) outside the Stokes flow regime, i.e. for $Re_p > 1$, which can be integrated with the current DNS point particle methodology.

- In all our simulations, particle concentration is assumed to be dilute i.e. only the effect of turbulence on particle is considered and the feedback from particle on flow is neglected. Including particle-particle collision, particle-wall collision models can improve the capability of the present code to predict the higher concentration particle suspensions. Recently some of these aspects were looked at by other groups (Zhao et al. 2015 and Zhao and Wachem 2013).

- It has been shown that the preferential alignment of spheroid particle major axis is in the strongest Lagrangian stretching direction (Ni et al. 2014) in homogeneous isotropic turbulent flows. Similar physical understanding is not yet known for preferential alignment of spheroids in the near-wall region of wall-bounded turbulent flows.

Bibliography

Abbasi Hoseini, A., Lundell, F. & Andersson, H.I. 2015 Finite-length effects on dynamical behavior of rod-like particles in wall-bounded turbulent flow. *Int. J. Multiphase Flow* **76**, 13-21.

Andersson, H.I. & Soldati, A. 2013 Anisotropic particles in turbulence: status and outlook. *Acta Mechanica* **224**, 2219-2223.

Balachandar, S. & Eaton, J. K. 2010 Turbulent dispersed multiphase flow. *Annu. Rev. Fluid Mech.* **42**, 111-133.

Bellani, G., Byron, M.L., Collignon, A.G., Meyer, C.R. & Variano, E.A. 2012 Shape effects on turbulent modulation by large nearly neutrally buoyant particles. *J. Fluid Mech.* **712**, 41-60.

Brenner, H. 1963 The Stokes resistance of an arbitrary particle. *Chem. Engng Sci.* **18**, 1-25.

Brenner, H. 1964 The Stokes resistance of an arbitrary particle IV: Arbitrary fields of flow. *Chem. Engng Sci.* **19**, 703-727.

Byron, M., Einarsson, J., Gustavsson, K., Voth, G., Mehlig, B. & Variano, E. 2015 Shape-dependence of particle rotation in isotropic turbulence. *Phys. Fluids* **27**, 035101.

Davidson, P. A. 2004 Turbulence - An introduction for scientists and engineers. *Oxford University Press.*

Do-Quang, M., Amberg, G., Brethouwer, G. & Johansson, A.V. 2014 Simulation of finite-size fibers in turbulent channel flows. *Phys. Rev. E* **89**, 013006.

Durbin, P.A. & Reif, B.A.P. 2001 Statistical theory and modeling for turbulent flows. *Wiley.*

Fan, F.-G. & Ahmadi, G. 1995 Dispersion of ellipsoidal particles in an isotropic pseudo-turbulent flow field. *J. Fluids Eng.* **117**, 154-161.

Gallily, I. & Cohen, A.-H. 1979 On the orderly nature of the motion of nonspherical aerosol particles. II. Inertial collision between a spherical large droplet and an axially symmetrical elongated particle. *J. Colloid Interface Sci.* **68**, 338-356.

Gauthier, G., Gondret, P. & Rabaud, M. 1998 Motions of anisotropic particles: application to visualization of three-dimensional flows. *Phys. Fluids* **10**, 2147-2154.

Goldstein, H. 1980 Classical mechanics, 2nd ed. *Addison Wesley.*

Guasto, J.S., Rusconi, R. & Stocker, R. 2012 Fluid mechanics of planktonic microorganisms. *Annu. Rev. Fluid Mech.* **44**, 373-400.

Guha, A. 2008 Transport and deposition of particles in turbulent and laminar flow. *Annu. Rev. Fluid Mech.* **40**, 311-341.

Gustavsson, K., Einarsson, J. & Mehlig, B. 2014 Tumbling of small axisymmetric particles in random and turbulent flows. *Phys. Rev. Lett.* **112**. 014501

Harper, E.Y. & Chang, I.-D. 1968 Maximum dissipation resulting from lift in a slow viscous shear flow. *J. Fluid Mech.* **33**, 209-225.

Hilton, J.E. & Cleary, P.W. 2011 The influence of particle shape on flow modes in pneumatic conveying. *Chem. Engng Sci.* **66**, 231-240.

Hölzer, A. & Sommerfeld, M. 2008 New simple correlation formula for the drag coefficient of non-spherical particles. *Powder Tech.* **184**, 361-365.

Huang, H., Yang, X., Krafczyk, M. & Lu, X.-Y. 2012 Rotation of spheroidal particles in Couette flows. *J. Fluid Mech.* **692**, 369-394.

Jeffery, G. B. 1922 The motion of ellipsoidal particles immersed in a viscous fluid. *Proc. Roy. Soc.* A **102**, 161-179.

Launder, B.E. & Sandham, N.D. 2002 Closure Strategies for Turbulent and Transitional Flows. *Cambridge University Press.*

Lee, M. & Moser, R.D. 2015 Direct numerical simulation of turbulent channel flow up to ≈ 5200. *J. Fluid Mech.* **774**, 395-415.

Lin, J., Shi, X. & Yu, Z. 2003 The motion of fibers in an evolving mixing layer. *Int. J. Multiphase Flow* **29**, 1355-1372.

Loth, E. 2000 Numerical approaches for motion of dispersed particles, droplets and bubbles. *Progress in Energy and Combustion Science* **26**, 161-223.

Lucci, F., Ferrante, A. & Elghobashi, S. 2010 Modulation of isotropic turbulence by particles of Taylor length-scale size. *J. Fluid Mech.* **650**, 5-55.

Lundell, F. & Carlsson, A. 2010 Heavy ellipsoids in creeping shear flow: transitions of the particle rotation rate and orbit shape. *Phys. Rev. E* **81**, 016323.

Lundell, F., Söderberg, L.D. & Alfredsson, P.H. 2011 Fluid mechanics of papermaking. *Annu. Rev. Fluid Mech.* **43**, 195-217.

Ma, L., Jones, J.M., Pourkashanian, M. & Williams, A. 2007 Modelling the combustion of pulverized biomass in an industrial combustion test furnace. *Fuel* **86**, 1959-1965.

Marchioli, C., Fantoni M. & Soldati, A. 2010 Orientation, distribution, and deposition of elongated, inertial fibers in turbulent channel flow. *Phys. Fluids* **22**, 033301.

Marcus, G.G., Parsa, S., Kramel, S., Ni, R. & Voth, G.A. 2014 Measurements of the solid-body rotation of anisotropic particles in 3D turbulence. *New J. Phys.* **16**, 102001.

Mashayek, F. & Pandya, R.V.R. 2003 Analytical description of particle/droplet-laden turbulent flows. *Prog. Energy Combust. Sci.* **29**, 329-378.

Maxey, M.R. & Riley, J.J. Soldati, A. 1983 Equation of motion for a small rigid sphere in a nonuniform flow. *Phys. Fluids* **26**, 883-889.

Mortensen, P.H. 2007 Particle dynamics in wall-bounded turbulence. PhD thesis, Norwegian University of Science and Technology, ISBN 978-82-471-5921-7.

Mortensen, P.H., Andersson, H.I., Gillissen, J.J.J. & Boersma, B.J. 2008 Dynamics of prolate ellipsoidal particles in a turbulent channel flow. *Phys. Fluids* **20**, 093302.

Ni, R., Kramel, S., Ouellette, N.T. & Voth, G.A. 2015 Measurements of the coupling between the tumbling of rods and the velocity gradient tensor in turbulence. *J. Fluid Mech.* **766**, 202-225.

Ni, R., Ouellette, N.T. & Voth, G.A. 2014 Alignment of vorticity and rods with Lagrangian fluid stretching in turbulence. *J. Fluid Mech.* **743**, R3.

Nilsen, C. & Andersson, H.I. 2013 Chaotic rotation of inertial spheroids in oscillating shear flow. *Phys. Fluids* **25**, 013303.

Njobuenwu, D.O. & Fairweather, M. 2014 Effect of shape on inertial particle dynamics in a channel flow. *Flow Turbul. Combust.* **92**, 83-101.

Njobuenwu, D.O. & Fairweather, M. 2015 Dynamics of single, non-spherical ellipsoidal particles in a turbulent channel flow. *Chem. Engng Sci.* **123**, 265-282.

Njobuenwu, D.O. & Fairweather, M. 2016 Simulation of inertial fibre orientation in turbulent flow. *Phys. Fluids* **28**, 063307.

Olson, J.A. 2001 The motion of fibres in turbulent flow, stochastic simulation of isotropic homogeneous turbulence. *Int. J. Multiphase Flow* **27**, 2083-2103.

Ouchene, R., Khalij, M., Arcen, B. & Tanire, A. 2016 A new set of correlations of drag, lift and torque coefficients for non-spherical particles and large Reynolds numbers. *Powder Technology* **In press**, doi:10.1016/j.powtec.2016.07.067.

Ozolins, A. & Strautins, U. 2014 Simple models for wall effect in fiber suspension flows. *Mathematical Modelling and Analysis* **19**, 75-84.

Parsa, S., Calzavarini, E., Toschi, F. & Voth, G.A. 2012 Rotation rate of rods in turbulent fluid flow. *Phys. Rev. Lett.* **109**, 134501

Pope, S. B. 1972 Turbulent flows. *Cambridge University Press.*

Qi, D. & Luo, L.-S. 2003 Rotational and orientational behaviour of three-dimensional spheroidal particles in Couette flows. *J. Fluid Mech.* **477**, 201-213.

Rosén, T., Nordmark, A., Aidun, C.K., Do-Quang, M. & Lundell, F. 2016 Quantitative analysis of the angular dynamics of a single spheroid in simple shear flow at moderate Reynolds numbers. *Phys. Rev. Fluid* **1**, 044201.

Rosén, T., Do-Quang, M., Aidun, C.K. & Lundell, F. 2015 The dynamical states of a prolate spheroidal particle suspended in shear flow as a consequence of particle and fluid inertia. *J. Fluid Mech.* **771**, 115-158.

Rosén, T., Lundell, F. & Aidun, C.K. 2014 Effect of fluid inertia on the dynamics and scaling of neutrally buoyant particles in shear flow. *J. Fluid Mech.* **738**, 563-590.

Sagaut, P. 2006 Large eddy simulation for incompressible flows *Springer-Verlag, Berlin/Heidelberg.*

Shapiro, M. & Goldenberg, M. 1993 Deposition of glass fiber particles from turbulent air flow in a pipe. *J. Aero. Sci.* **24**, 65-87.

Shaw, R.A. 2003 Particle-turbulence interactions in atmospheric clouds. *Annu. Rev. Fluid Mech.* **35**, 183-227.

Shin, M. & Koch, D.L. 2005 Rotational and translational dispersion of fibres in isotropic turbulent flows. *J. Fluid Mech.* **540**, 143-173.

Shirolkar, J.S., Coimbra, C.F.M. & Queiroz McQuay, M. 1996 Fundamental aspects of modeling turbulent particle dispersion in dilute flows. *Prog. Energy Combust. Sci.* **22**, 363-399.

Siewert, C., Kunnen, R.P.J., Meinke, M. & Schröer, W. 2014a Orientation statistics and settling velocity of ellipsoids in decaying turbulence. *Atmos. Res.* **142**, 45-56.

Siewert, C., Kunnen, R.P.J. & Schröder, W. 2014b Collision rates of small ellipsoids settling in turbulence. *J. Fluid Mech.* **758**, 686-701.

Subramanian, G. & Koch, D.L. 2005 Inertial effects on fibre motion in simple shear flow. *J. Fluid Mech.* **535**, 383-414.

Tennekes, H. & Lumley, J. L. 1972 A first course in turbulence. *MIT Press.*

Toschi, F. & Bodenschatz, E. 2009 Lagrangian properties of particles in turbulence. *Annu. Rev. Fluid Mech.* **41**, 375-404.

Uhlmann, M. 2008 Interface-resolved direct numerical simulation of vertical particulate channel flow in the turbulent regime. *Phys. Fluids* **20**, 053305.

Voth, G.A. & Soldati, A. 2017 Anisotropic Particles in Turbulence. *Annu. Rev. Fluid Mech.* **49**, In Press.

Wilcox, D.C. 1994 Turbulence Modeling for CFD. *DCW Industries.*

YIN, C., ROSENDAHL, L., KNUDSEN KÆR, S. & SØRENSEN, H. 2003 Modelling the motion of cylindrical particles in a nonuniform flow. *Chem. Engng Sci.* **58**, 3489-3498.

YU, Z., PHAN-THIEN, N. & TANNER, R. 2007 Rotation of a spheroid in a Couette flow at moderate Reynolds numbers. *Phys. Rev. E* **76**, 026310

ZASTAWNY, M., MALLOUPPAS, G., ZHAO, F. & VAN WACHEM, B. 2012 Derivation of drag and lift force and torque coefficients for non-spherical particles in flows. *Int. J. Multiphase Flow* **39**, 227-239.

ZHANG, H., AHMADI, G. & FAN, F. G. & MCLAUGHLIN, J.B. 2001 Ellipsoidal particle transport and deposition in turbulent channel flows. *Int. J. Multiphase Flow* **27**, 971-1009.

ZHAO, F., GEORGE, W.K. & WACHEM, B.G.M.V. 2015 Four-way coupled simulations of small particles in turbulent channel flow: The effects of particle shape and Stokes number. *Phys. Fluids* **27**, 083301.

ZHAO, F., WACHEM & B.G.M.V. 2013 Direct numerical simulation of ellipsoidal particles in turbulent channel flow. *Acta Mechanica* **224**, 2331-2358.

ZHAO, L. 2011 Particles in wall turbulence. PhD thesis, Norwegian University of Science and Technology, ISBN 978-82-471-3293-7.

ZHAO, L., MARCHIOLI, C. & ANDERSSON, H.I. 2014 Slip velocity of rigid fibers in turbulent channel flow. *Phys. Fluids* **26**, 063302.

Part 2

Articles

Article 1

On rotational dynamics of inertial disks in creeping shear flow

Niranjan Reddy Challabotla, Christopher Nilsen &
Helge I. Andersson

Physics Letters A, **379**, 157-162, 2015.

Physics Letters A 379 (2015) 157–162

Contents lists available at ScienceDirect

Physics Letters A

www.elsevier.com/locate/pla

On rotational dynamics of inertial disks in creeping shear flow

Niranjan Reddy Challabotla [*], Christopher Nilsen, Helge I. Andersson

Department of Energy and Process Engineering, The Norwegian University of Science and Technology, NO-7491 Trondheim, Norway

ARTICLE INFO

Article history:
Received 16 June 2014
Received in revised form 15 October 2014
Accepted 21 October 2014
Available online 18 November 2014
Communicated by F. Porcelli

ABSTRACT

The rotational motion of an inertial disk-like particle in a creeping linear shear flow is investigated. A disk-like particle in a linear shear flow tends to rotate in the velocity-gradient plane as do rod-like particles. Unlike prolate spheroids, however, oblate spheroids always attain the same steady rotation in the shear plane irrespective of their initial orientation. The drift of the orientation of the rotation axis towards the vorticity vector consists of two qualitatively different stages. First, the wobbling drift towards rotation in the velocity-gradient plane becomes slower with increasing particle inertia, except for the least inertial spheroids. The duration of the second stage, during which the spheroid spins up to match the angular fluid velocity, becomes independent of the aspect ratio for relatively flat particles, provided that a new shape-dependent Stokes number is used.

1. Introduction

The rotational dynamics of inertial spheroidal particles crucially depends on the aspect ratio as well as the inertia of the particle. A bi-axial ellipsoid, i.e. a spheroid, is a frequently adopted model shape for non-spherical particles. The aspect ratio k, defined as the ratio between the two equal axes and the symmetry axis, distinguishes between rod-like particles (prolate spheroids with $k < 1$) and disk-like particles (oblate spheroids with $k > 1$) and $k = 1$ corresponds to spherical particles. The rotational motion of single or many rod-like particles have recently received renewed attention of which the studies reported by Mortensen et al. [1], Lundell and Carlsson [2], Bellani et al. [3], Parsa et al. [4], Andersson et al. [5], and Nilsen and Andersson [6] are relevant examples. A topical journal issue was devoted to the dynamics of anisotropic particles in turbulent flows; see Andersson and Soldati [7].

The literature reporting the rotational dynamics of disk-like particles is comparatively scarce. Although the rotational motion of disk-like particles seems to be simpler than the intricate rotation of rod-like particles, see e.g. Qi and Luo [8], the dynamics of disk-like particles still require further exploration. Anisometric particles resembling thin disks immersed in a viscous fluid are encountered in nature (e.g. seeds, human red blood cells). A great interest in the behaviour of platelets exists in biomedical research, e.g. microcirculation flow (Mody and King [9]). Thin reflective flakes are commonly used for experimental flow visualization studies; e.g. Savaş [10], Gauthier et al. [11], and Philippe et al. [12].

Analytical and numerical investigations of anisometric particles are usually based on the analytical derivations made by Jeffery [13] for tri-axial ellipsoidal particles in a creeping shear flow. Disk-like particles are thus modeled as oblate spheroids where the ratio between the two equal major axes and the minor axis is the aspect ratio $k > 1$ which is a dimensionless measure of the flatness of the spheroidal particle.

Let us first take a look at earlier findings for *massless* disk-like particles. According to the Jeffery theory, the time evolution of a unit vector $\mathbf{p}$ parallel to the particle symmetry axis is governed by

$$\frac{d\mathbf{p}}{dt} = \boldsymbol{\Omega} \cdot \mathbf{p} - \frac{k^2 - 1}{k^2 + 1}\big[\mathbf{S} \cdot \mathbf{p} - \mathbf{p} \cdot (\mathbf{p} \cdot \mathbf{S} \cdot \mathbf{p})\big]. \tag{1}$$

The direction of the unit vector $\mathbf{p}$ identifies the orientation of the axisymmetric particle and $\boldsymbol{\Omega}$ and $\mathbf{S}$ are the anti-symmetric and symmetric parts of the fluid velocity gradient tensor in the particle frame, respectively, i.e. the rate-of-rotation and rate-of-strain tensors. This equation is valid for inertia-free axisymmetric ellipsoids irrespective of whether $k < 1$ or $k > 1$; see e.g. Leal and Hinch [14] and Gauthier et al. [11]. A disk-like particle spends most of the time with $\mathbf{p}$ along the shear axis, whereas the particle orientation vector is mostly along the flow axis for a rod-like particle. These motions are in accordance with experimental studies of Goldsmith and Mason [15] in laminar Taylor–Couette flow in a coaxial cylinder apparatus.

Recent DNS studies of anisometric particles with k in the range from 0.01 to 100 in homogeneous and isotropic turbulence by Parsa et al. [4] showed that the mean square rotation rate $\langle \dot{p}_i \dot{p}_i \rangle$ of disk-like particles ($k > 1$) is much larger than for spheres ($k = 1$). This can be qualitatively understood as the additional contribution

---

[*] Corresponding author.
E-mail address: niranjan.r.challabotla@ntnu.no (N.R. Challabotla).

http://dx.doi.org/10.1016/j.physleta.2014.10.045
0375-9601/

of strain **S** to the rotation rate in Eq. (1). Disk-like particles also show some effects of alignment with the vorticity vector $2\boldsymbol{\Omega}$ although their mean square rotation rate is substantially closer to the randomly oriented case

$$\frac{\langle \dot{p}_i \dot{p}_i \rangle}{\langle \varepsilon \rangle/\nu} = \frac{1}{6} + \frac{1}{10}\left(\frac{k^2-1}{k^2+1}\right)^2 \tag{2}$$

derived from Eq. (1) than are rod-like particles. Here, ε is the energy dissipation rate $2\nu S_{ij}S_{ij}$ and ν is the kinematic viscosity of the fluid.

The orientation of disk-like particles was utilized in an experimental study of the Taylor–Couette instability by Philippe et al. [12]. A preferential orientation of the suspended clay particles (flakes) was reported. As soon as the Taylor–Couette vortices appeared, the average orientation of the particles was slightly shifted under secondary flow effect depending on their positions in the vortices. These experimental observations are consistent with the analysis of Angilella [16] who showed that a massless and infinitely thin circular disk (i.e. $k \to \infty$) has a stable equilibrium position with **p** in the shear plane and perpendicular to the velocity.

Investigations of the dynamics of *inertial* spheroids have mostly been concerned with the translational and rotational motion of prolate spheroids. Qi and Luo [8] studied the rotation of neutrally buoyant spheroids by means of lattice Boltzmann simulations. At low particle Reynolds numbers *Re* the oblate spheroid eventually spins at a constant rate around its minor axis, which is parallel to the flow vorticity vector. This state is called ‘spinning’. However, a transition occurs at $Re \approx 220$ beyond which the oblate spheroid still spins about its minor axis, but the minor axis has now a finite inclination with the vorticity. This is called ‘inclined spinning’ and the inclination angle increases monotonically with *Re*. Yu et al. [17] called the ‘spinning’ mode of Qi and Luo [8] a ‘log-rolling’ mode and they reported a rather different critical transition Reynolds number. They also found a second transition to a ‘motionless mode’ not observed by Qi and Luo [8]. Huang et al. [18] used a lattice Boltzmann method to simulate neutrally buoyant spheroids in laminar Couette flow. They found that the tumbling period of an oblate spheroid increased with *Re*. In addition to the transition reported by Qi and Luo [8], they also found a second transition to the ‘motionless mode’ first reported by Yu et al. [17]. Einarsson et al. [19] very recently derived an asymptotic equation of motion for small Stokes numbers (modest inertia) for the orientation vector **p** valid for both prolate and oblate spheroids.

The aim of the present study is to examine the rotational dynamics of inertial disk-like particles in a creeping linear shear flow. The objective is to explore how the particle dynamics are affected by the particle shape (aspect ratio $k > 1$) and particle inertia (to be quantified by a new shape-dependent Stokes number *St*). The mathematical modeling closely follows the recent work by Lundell and Carlsson [2] in which the effect of inertia and aspect ratio on rod-like particles ($k < 1$) in creeping shear was studied. Although gravity might affect the rotational dynamics of the heavier particles ($St \gg 1$) the effect of gravity is not included in this work.

2. Problem statement

We consider the linear shear flow $u' = \kappa z'$ in the (x', z') plane. The shear rate κ is constant here, as in Lundell and Carlsson [2], whereas a time-varying shear rate was considered by Nilsen and Andersson [6]. The Reynolds number $Re = \kappa a^2/\nu \ll 1$ in order to justify the assumption of creeping fluid motion in the vicinity of the particles, i.e. that the flow is inertia-free. $2a$ is the minor axis, i.e. the symmetry axis, of the oblate spheroid whose surface is described by

$$\frac{x^2}{a^2} + \frac{y^2}{b^2} + \frac{z^2}{b^2} = 1 \tag{3}$$

in a particle frame of reference. The particle aspect ratio $k = b/a$ is thus the essential non-dimensional geometric parameter.

The Stokes number St_{LC} is defined as the ratio between the particle time scale $\tau = a^2\rho_p/\mu_f$ and the time scale κ^{-1} of the shear flow

$$St_{LC} = \frac{\kappa a^2}{\nu}\frac{\rho_p}{\rho_f} = Re\frac{\rho_p}{\rho_f}. \tag{4}$$

The Stokes number is therefore known for a given Reynolds number *Re* and particle-to-fluid density ratio ρ_p/ρ_f. This Stokes number, which is the same as that used by Lundell and Carlsson [2], does not necessarily allow physical interpretations in the same way as in turbulent flows. This is partly due to the time scale κ^{-1} of the flow, which is not representative for any dynamics. Aside from a factor 2/9 the particle time scale τ used here is the relaxation time for translational motion of a spherical particle with radius a, although it is likely that the dynamic response of a disk-like particle to changes in the flow field depends also on the orientation and shape of the particle.

3. Mathematical modelling

3.1. Kinematics

The orientation of a spheroid is represented by a quaternion

$$\mathbf{e} = [e_0\ e_1\ e_2\ e_3]^T, \tag{5}$$

which is defined by means of the Euler angles (ϕ, θ, ψ) in accordance with the x-convention of Goldstein [20]; see also Ref. [21]. An orthogonal rotation matrix **R** can be defined in terms of the components of the quaternion (5) as

$$\mathbf{R} = \mathbf{E}\mathbf{G}^T \tag{6}$$

where

$$\mathbf{E} = \begin{bmatrix} -e_1 & e_0 & -e_3 & e_2 \\ -e_2 & e_3 & e_0 & -e_1 \\ -e_3 & -e_2 & e_1 & e_0 \end{bmatrix} \quad \text{and}$$

$$\mathbf{G} = \begin{bmatrix} -e_1 & e_0 & e_3 & -e_2 \\ -e_2 & -e_3 & e_0 & e_1 \\ -e_3 & e_2 & -e_1 & e_0 \end{bmatrix}. \tag{7}$$

A vector $\mathbf{a}'$ in the fixed coordinate system is now related to the vector **a** in the coordinate system fixed to the particle according to $\mathbf{a}' = \mathbf{R}\mathbf{a}$. A flow field $\mathbf{u}' = \mathbf{K}\mathbf{x}'$ in the inertial system now becomes

$$\mathbf{u} = \mathbf{R}^{\mathbf{T}}\mathbf{K}\mathbf{R}\mathbf{x} \tag{8}$$

in the particle frame of reference. Here, the velocity gradient tensor **K** is $K_{ij} = \kappa\delta_{i1}\delta_{3j}$ for the present shear flow case.

3.2. Dynamics

The rotation $\boldsymbol{\omega}$ of a spheroid is governed by the non-dimensional Euler's equation

$$\mathbf{I}\cdot\dot{\boldsymbol{\omega}} + \boldsymbol{\omega}\times(\mathbf{I}\cdot\boldsymbol{\omega}) = \frac{16\pi}{3St_{LC}}\mathbf{M} \tag{9}$$

together with the time-variation (denoted by a dot) of the quaternion

$$\dot{\mathbf{e}} = \frac{1}{2}\mathbf{G}^T\boldsymbol{\omega}. \tag{10}$$

The moment of inertia for an oblate spheroid is

$$\mathbf{I} = \frac{4}{15}\pi k^2 \begin{bmatrix} 2k^2 & 0 & 0 \\ 0 & 1+k^2 & 0 \\ 0 & 0 & 1+k^2 \end{bmatrix}. \tag{11}$$

The non-dimensional torque $\mathbf{M}$ from the shearing fluid flow on a tri-axial ellipsoidal particle was originally derived by Jeffery [13]. For the axisymmetric ellipsoid (3) the Jeffery-torque simplifies to:

$$\mathbf{M} = \begin{bmatrix} 2(\beta_0+\gamma_0)^{-1}(\Omega_{zy}-\omega_x) \\ (k^2\gamma_0+\alpha_0)^{-1}\{(k^2-1)S_{xz}+(k^2+1)(\Omega_{xz}-\omega_y)\} \\ (\alpha_0+k^2\beta_0)^{-1}\{(1-k^2)S_{xy}+(1+k^2)(\Omega_{yx}-\omega_z)\} \end{bmatrix}, \tag{12}$$

where $\mathbf{S}$ and $\boldsymbol{\Omega}$ now are the non-dimensionalized fluid rate-of-strain and rate-of-rotation tensors in the particle frame-of-reference. Similarly the expressions for the non-dimensional coefficients simplify to:

$$\alpha_0 = \int_0^\infty \frac{d\lambda}{(1+\lambda)^{3/2}(k^2+\lambda)} \quad \text{and}$$

$$\beta_0 = \gamma_0 = \int_0^\infty \frac{d\lambda}{(k^2+\lambda)^2(1+\lambda)^{1/2}}, \tag{13}$$

see Gallily and Cohen [22] and Lundell and Carlsson [2]. The vector equations (9) and (10) govern the rate-of-change with time of the angular velocity $\boldsymbol{\omega}$ and the quaternion $\mathbf{e}$ and comprise seven non-linearly coupled ordinary differential equations (ODEs).

4. Analytical solution and time scale considerations

Let us first look at the rotation of an oblate spheroid about its minor axis in the flow gradient plane. Since the two semi-major axes are equal for an oblate spheroid, M_x in Eq. (12) has simplified such that the x-component of Euler's equation (9) can be solved analytically. If ω_x is initially set to zero, we obtain the analytical solution:

$$\omega_x = \Omega_{zy}\left(1-e^{-t/\tau_{rot}}\right), \tag{14}$$

where t is dimensionless time normalized with κ^{-1}. For the simple shear flow considered in the present study, the fluid rate-of-rotation in the particle frame non-dimensionalized with the shear rate κ in the inertial frame becomes 1/2. The relaxation time τ_{rot} for rotation about the x-axis can be expressed as:

$$\tau_{rot} = \frac{\tau}{10}k^4\beta_0 \tag{15}$$

where τ_{rot} and τ are both normalized by means of the time scale κ^{-1} of the linear shear flow. The new time scale τ_{rot} in Eq. (15), which is proportional to the time scale $2\tau/9$ which characterizes the translational motion of spherical particles, exhibits a strong explicit dependence on the flatness k of the disk-like particle. Moreover, τ_{rot} also depends implicitly on the particle shape through the dimensionless coefficient β_0 defined in Eq. (13). Here the dimensional τ is as defined in conjunction with Eq. (4). Let us recall, however, that the rotational response time for spherical particles is 3/10 of the translational relaxation time $2\tau/9$, i.e. $\tau/15$; see Zhao and Andersson [23].

In view of the preceding arguments, a physically more relevant Stokes number St should be based on τ_{rot} defined in Eq. (15) rather than on τ. This gives the new Stokes number

$$St = \frac{St_{LC}}{10}k^4\beta_0 \tag{16}$$

where St_{LC} is the Stokes number already defined in Eq. (4). The Stokes number St is believed to be a better choice than St_{LC} for parameterization of the rotational dynamics of oblate spheroids since it involves the aspect ratio k explicitly and also indirectly through the shape factor β_0 defined in Eq. (13). The ratio St/St_{LC} increases monotonically from $1/15 \approx 0.07$ for spherical particles ($k=1$) to 1.39 and 15.5 for $k=10$ and 100, respectively.

In computer simulations of rod-like particles suspended in a turbulent flow field, a particle relaxation time based on the assumption of an isotropic particle orientation due to Shapiro and Goldenberg [24] is routinely used by, for instance, Mortensen et al. [1] and Andersson et al. [5].

5. Computed results

The two-parameter problem defined in the mathematical modelling section has been solved for Stokes numbers St in the range from 0.1 to 100 and particle aspect ratios k in the range from 1.5 to 60. It is noteworthy that the analysis is based on the Stokes number St defined in Eq. (16) rather than on the shape-independent Stokes number St_{LC} used by Lundell and Carlsson [2]. The set of ODEs (9), (10) is integrated forward in time by means of the built-in MATLAB functions ode15s and ode45; see Ref. [25]. Irrespective of Stokes number and aspect ratio, the oblate spheroid is initially positioned with its symmetry axis almost in the z'-direction so that the particle orientation vector $\mathbf{p}$ is nearly perpendicular to the fluid vorticity vector. Since the particular orientation $\phi=\theta=\psi=0$ is neutrally stable, we considered the slightly perturbed initial orientation $\phi=0$, $\theta=0.001$, and $\psi=0.001$. The effect of different initial orientations on the rotational motion is examined in Appendix A where it is shown that an oblate spheroid eventually attains the same state of steady rotation in the flow gradient plane irrespective of its initial orientation.

The trajectory of a point on the equator of a spheroidal particle is shown in Fig. 1. At $St=1$ the modestly oblate spheroid ($k=1.5$) to the left in Fig. 1(b) rapidly flips away from its initial orientation and rotates about its minor axis x, i.e. the symmetry axis, which gradually becomes perpendicular to the shear plane (x', z'). For the higher Stokes numbers $St=10$ and 100, a wobbling motion of the oblate spheroid persists over a relatively long time interval until the spheroid eventually spins up and rotates in the shear plane. The behaviour of the spheroid with the least inertia in Fig. 1(a) exhibits the same trend as the most inertial spheroid in Fig. 1(d). The rotational motion of a more disk-like spheroid ($k=10$) is displayed to the right in Fig. 1. The disk at $St=1$ takes longer time before aligning in the flow-gradient plane in comparison with the rapid transition observed in Fig. 1(b). At higher Stokes numbers the flatter spheroids ($k=10$) in Fig. 1(g, h) reach a steady state faster than the only modestly flat particles ($k=1.5$) in Fig. 1(c, d).

The particle trajectories shown in Fig. 1(e) are different from the findings of Gauthier et al. [11] for non-inertial disks with $k=10$. They found that the orientation vector $\mathbf{p}$ described a closed orbit, a so-called Jeffery-orbit, with $\mathbf{p}$ most of the time along the shear direction z'. The Jeffery-orbit of an inertia-free disk is determined by its initial conditions which are never forgotten, whereas the effect of the initial orientation is eventually forgotten by inertial disks (this essential issue is addressed in Appendix A). The differences between the trajectories found here and those in Ref. [11] are therefore due to the inclusion of particle inertia in the present case. Inertia forces the oblate spheroid towards the flow gradient plane, as is also the case for prolate spheroids (Lundell and Carlsson [2]).

The time evolution of the angular velocity ω_x about the symmetry axis and the angular velocity $\omega_{yz} \equiv (\omega_y^2+\omega_z^2)^{1/2}$ about an axis perpendicular to the symmetry axis are shown in Fig. 2 for $St=1$ (left) and for $St=100$ (right) for three different aspect

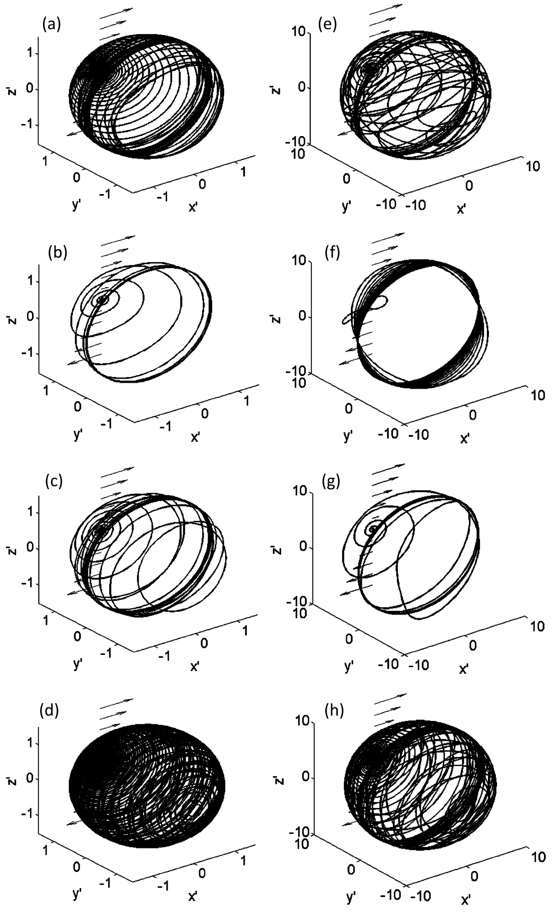

Fig. 1. Trajectory of a point on the equator of an oblate spheroid during spin-up. Aspect ratio $k = 1.5$ to the left and $k = 10$ to the right for some different Stokes numbers. $St = 0.1$ (a, e), $St = 1$ (b, f), $St = 10$ (c, g), and $St = 100$ (d, h).

ratios k. In all cases the oblate spheroid is set into rotation from its initial state $\boldsymbol{\omega} = \mathbf{0}$. During an initial stage of the particle rotation, the resultant angular velocity ω_{yz} varies periodically whereas the angular velocity about the symmetry axis $\omega_x \approx 0$. Somewhat later, however, ω_x increases monotonically towards the asymptotic limit 0.5 while ω_{yz} gradually decays to zero. These trends reflect the wobbling of the oblate spheroid before the stable rotation with the symmetry axis perpendicular to the shear-plane (x', z') and period 4π has been established. This is the same rotation period as for an inertial sphere $(k = 1)$. Independent of aspect ratio k, a oblate spheroid is spun up to the same steady rotation as a spherical particle. However, a disk-like particle with only modest inertia $(St = 1.0)$ approaches the flow-gradient plane more slowly as k is increased, whereas the opposite trend is observed for large inertia $(St = 100)$. These trends refer to the first stage of the transient rotation during which $\omega_x \ll 0.5$. Inertia has been shown before by Lundell and Carlsson [2] to induce a drift of the particle orientation of prolate spheroids $(k < 1)$ towards the flow-gradient plane and Nilsen and Andersson [6] showed that the rotation period of a prolate spheroid was crucially dependent on the Stokes number and the aspect ratio and qualitatively different from the present results for an oblate spheroid.

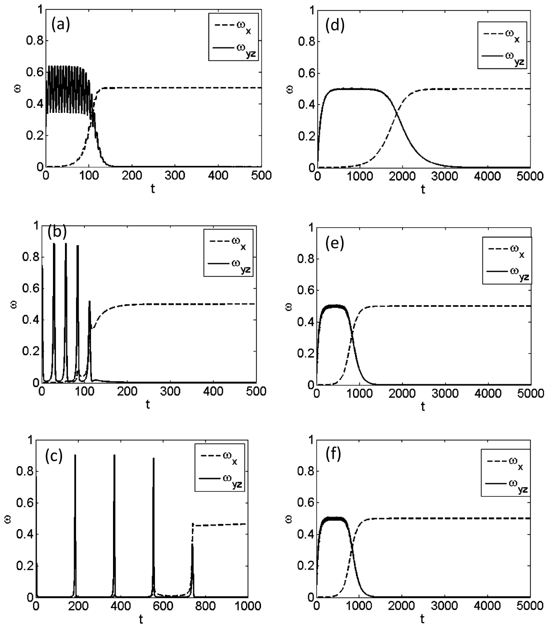

Fig. 2. Evolution of the angular velocity of an oblate spheroid during spin-up. Stokes number $St = 1.0$ to the left (panels a, b, and c) and $St = 100$ to the right (panels d, e, and f) for some different aspect ratios. $k = 1.5$ (a, d), $k = 10$ (b, e), $k = 60$ (c, f).

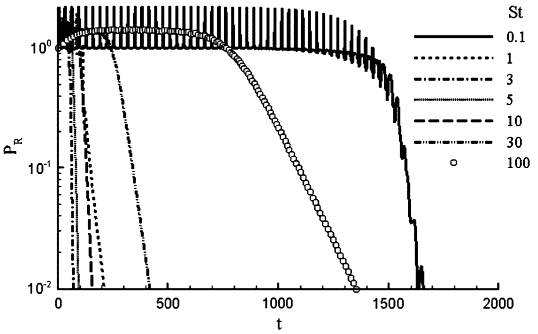

Fig. 3. Evolution of P_R with time for oblate spheroids with $k = 10$ for different Stokes numbers.

In view of the behaviour of the angular velocities in Fig. 2 we now define a rotation parameter

$$
\begin{aligned}
P_R &= 2\left[\left(0.5 - |\omega_x|\right)^2 + \omega_y^2 + \omega_z^2\right]^{1/2} \\
&= 2\left[\left(0.5 - |\omega_x|\right)^2 + \omega_{yz}^2\right]^{1/2}
\end{aligned}
\tag{17}
$$

such that P_R varies from the initial value 1.0 for a non-rotating spheroid to 0 at large times when ω_x tends to either $+0.5$ or -0.5 while ω_y and ω_z approach zero. The results in Fig. 3 show how an oblate spheroid with aspect ratio $k = 10$ adjusts from the non-rotating initial condition to the ultimate state of steady rotation. The duration of the transient stage from $\boldsymbol{\omega} = \mathbf{0}$ to $\boldsymbol{\omega}_\infty = 0.5\mathbf{e}_x$ depends severely on the Stokes number. The distinctly different transient behaviour for $St = 1$ and $St = 100$ spheroids could be observed already by comparing panels (b) and (e) in Fig. 2. With increasing inertia, i.e. higher Stokes number St, the spheroid

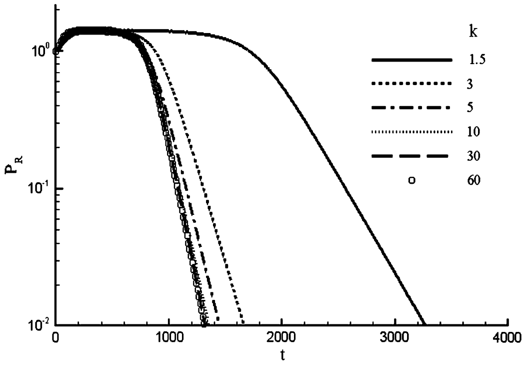

Fig. 4. Evolution of P_R with time for oblate spheroids with Stokes number $St = 100$ for different aspect ratios k.

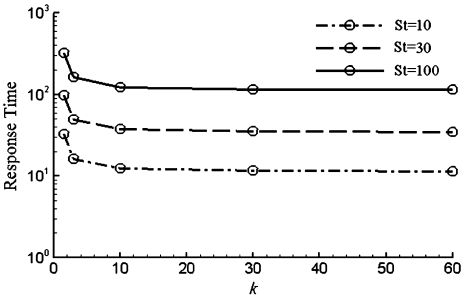

Fig. 5. Duration of the last part of the spin-up process for different aspect ratios k and three different Stokes numbers. Dotted line: $St = 10$; broken line: $St = 30$; solid line: $St = 100$.

generally requires a substantially longer time to spin up from rest and attain its ultimate steady-state rotation about its minor axis. This monotonic trend applies for $St \geq 3$. However, at the lowest Stokes number considered, i.e. $St = 0.1$, the spheroid approaches the flow-gradient plane even more slowly than the most inertial spheroid. This is attributed to the exceptionally slow growth of tiny perturbations during the first stage of the transient. After the long first stage of adaptation, the last stage of the spin-up process, during which P_R decays to zero, is short and fully in accordance with the very modest inertia of the $St = 0.1$ spheroid. It is worthwhile to recall that the time to reach the final state of rotational motion is shortest for intermediate Stokes numbers also for prolate spheroids; see Fig. 7 in Lundell and Carlsson [2].

The time evolution of the rotation parameter P_R is also shown in Fig. 4 for different particle aspect ratios k and Stokes number $St = 100$. It is readily observed that a nearly spherical spheroid ($k = 1.5$) spins up slowly and ultimately reaches the asymptotic state of steady rotation $P_R = 0$. However, the more disk-like particles, i.e. the flatter spheroids with $k > 1.5$, approach the steady rotational state substantially faster. As the aspect ratio k increases above five, the overall spin-up time seems to be independent of the aspect ratio and of the order of 1000 non-dimensional time units. It is noteworhty that this collapse of the spin-up histories for $k > 5$ at a given Stokes number has been achieved by adopting the shape-dependent Stokes number defined in Eq. (16).

Although an oblate spheroid spins up to the same ultimate state of steady rotation in the flow-gradient plane (see Appendix A), the spin-up time depends on the initial orientation of the spheroid relative to that plane, as well as on the Stokes number St and the aspect ratio k. For a given initial orientation the results displayed in Figs. 2–4 suggest that the duration of the transient period from rest to the ultimate rotation in the plane of shear consists of a first stage with unsteady rotation with $\omega_{yz}^2 \gg \omega_x^2$ and a subsequent spin-up during which ω_{yz} decays to zero and ω_x tends to $\pm 1/2$, i.e. stable rotation about the x-axis in the (x', z')-plane. The numerical solutions in Figs. 3 and 4 furthermore suggest that after the first stage with unsteady rotation the remaining approach towards the asymptotically steady state is almost exponential. Recall also the exponential evolution given by the analytical solution (14). The decay rates, i.e. the slopes in Fig. 4, increase with k. The flatter the disk, the higher the spin-up rate. The disks are rotating with non-zero components of the angular velocity vector $\boldsymbol{\omega}$ along all three directions of the particle frame of reference; see Fig. 2. The analytical solution (14) is, however, valid only if ω_x and ω_y both are zero. On the other hand, if the orientation vector $\mathbf{p}$ is initially perpendicular to the flow gradient plane (i.e. aligned with flow vorticity vector), the spin-up is truly exponential and matches the analytical solution (14). See the effect of some different initial orientations in Fig. A.1.

The duration T of this final stage of adaptation of the particle rotation can be defined as the time lapse from $P_R = 0.5$ to $P_R = 0.01$. The variation of T in the (St, k) parameter space is shown in Fig. 5. As expected, T increases with increasing inertia, i.e. higher Stokes numbers. For a given Stokes number, on the other hand, T is almost independent of the flatness of the spheroid for $k > 10$. This observation provides further support of the new shape-dependent Stokes number defined in Eq. (16). The duration T of the final spin-up process increases rapidly with decreasing flatness for $k < 10$, i.e. as the spheroid approaches spherical shape.

6. Conclusions

The rotational motion of inertial disk-like particles in creeping linear shear flow has been studied over a wide range of particle aspect ratios k and Stokes numbers St. The present study of the dynamics of oblate spheroids may therefore be considered as a sequel to the investigation by Lundell and Carlsson [2] of three-dimensional rotation of prolate spheroids in shear flow.

Starting from rest at an arbitrarily chosen initial state, a disk-like particle eventually tends to rotate in the velocity-gradient plane, as did the prolate spheroids. However, contrary to spheroidal particles with $k < 1$, the oblate spheroids with $k > 1$ rotates about their symmetry axis. The present findings for inertial spheroids are different from the observations of non-inertial spheroids by Gauthier et al. [11] who found that inertia-free disk-like particles oriented with $\mathbf{p}$, and thus the particle symmetry axis, mostly along the z'-direction. The distinctly different behaviour of the present spheroids is ascribed to particle inertia. Qi and Luo [8] studied the rotational motion of finite-sized inertial spheroids at Reynolds numbers well above unity using the lattice-Boltzmann method. Neutrally buoyant oblate spheroids with aspect ratio $k = 2$ turned out to spin up to a state of steady rotation about its minor axis with $\mathbf{p}$ aligned with the vorticity vector, i.e. in keeping with the present findings for $Re \ll 1$.

It is noteworthy that the drift of the orientation of the rotation axis towards the vorticity vector consists of two qualitatively different stages. The time scale of the first stage, in which the particle orientation changes from its arbitrary initial state to partial alignment with the vorticity vector, turns out to depend on the flatness and inertia of the disk-like particle. The last stage of the transient represents the spin-up of the axial rotation to the angular velocity of the fluid. If the particle is initially in the flow gradient plane, this spin-up is described by the analytical solution (14). In terms of a new Stokes number St based on the relaxation time τ_{rot} for rotation about the symmetry axis, as defined in Eq. (15), the duration of the spin-up stage becomes independent of particle shape

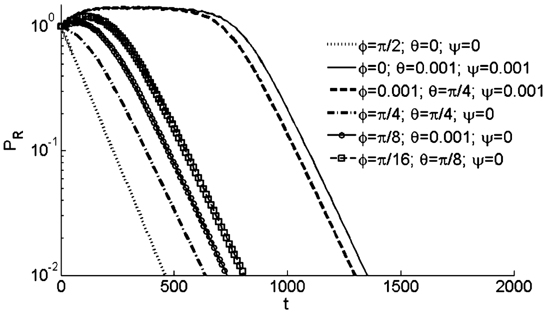

Fig. A.1. Spin-up of an inertial spheroid with $St = 100$ and $k = 10$ for six different initial orientations. The dotted line corresponds to an initial orientation with **p** perpendicular to the flow gradient plane and matches with the analytical solution (14). The solid line corresponds to the initial orientation of the oblate spheroids in Figs. 1–5.

for k greater than about 10 for a given Stokes number. Irrespective of its initial orientation, a prolate spheroid ultimately reaches the same state of steady rotation about the minor axis. The transient period required to achieve this stable steady state depends not only on the Stokes number St and the aspect ratio k but also on the initial orientation.

In a recent study of triaxial ellipsoids in linear shear flow, Lundell [26] showed that elongated ellipsoids can exhibit chaotic rotation even if they are almost axisymmetric, i.e. near-perfect prolate spheroids. On the contrary, rotation around the shortest axis of a flattened ellipsoid turned out to be stable even though they are almost axisymmetric, i.e. near-perfect oblate spheroids. Thus, compared with the prolate spheroid, the oblate spheroid has a considerable stability margin. Minute deviations from the perfect spheroidal shape do not give rise to instabilities which alter the solutions and conclusions presented in the present paper.

Acknowledgements

Funding by The Research Council of Norway through projects No. 213917/F20 “Turbulent particle suspensions” and No. 231444/F20 “Particle transport and clustering in stratified turbulence” is gratefully acknowledged. Øyvind W. Hanssen-Bauer (M.Sc.) carried out some preliminary calculations. Motivating discussions enabled by COST Action FP1005 funded by the European Science Foundation are appreciated.

Appendix A

Calculations are also performed to investigate the effect of the initial orientation of the spheroid on the rotational dynamics. The time evolutions of the rotational parameter P_R for different initial orientations are shown in Fig. A.1 for the particular parameter combination $St = 100$ and $k = 10$ case. The dotted line corresponds to a case in which the oblate spheroid is initially oriented with **p** aligned with the vorticity axis. The spheroid therefore rotates only about its minor axis, i.e. $\omega_{yz} = 0$, and asymptotically spins up to the state of steady rotation. The linear decay of P_R in the semi-logarithmic plot in Fig. A.1 is fully consistent with the exponential spin-up given by the analytical solution (14). In all other cases, in which the initial orientation of **p** is inclined with respect to the vorticity vector, the disk-like spheroid first undergoes a wobbling motion about a major axis which gradually decays to zero before the spheroid is spun up to steady rotation about its minor axis. This observation is consistent with Huang et al. [18] who recently concluded that oblate spheroid dynamics is insensitive to the initial orientation of the spheroid. It is noteworthy that exponential spin-up is observed irrespective of the initial orientation of the oblate spheroid in Fig. A.1 and, furthermore, that the spin-up rate in the final stage of spin-up process seems to be independent of the initial orientation provided that the spheroid is not oriented with **p** aligned with the fluid vorticity vector from the very beginning.

Although an oblate spheroid spins up to the same ultimate state of steady rotation in the flow-gradient plane, the overall spin-up time depends on the initial orientation of the spheroid relative to that plane, as well as on the Stokes number St and the aspect ratio k. The fastest adaptation to the rotation of the linear shear flow takes place when the spheroid is initially in the shear plane.

References

[1] P.H. Mortensen, H.I. Andersson, J.J.J. Gillissen, B.J. Boersma, Dynamics of prolate ellipsoidal particles in turbulent channel flow, Phys. Fluids 20 (2008) 093302.
[2] F. Lundell, A. Carlsson, Heavy ellipsoids in creeping shear flow: transitions of the particle rotation rate and orbit change, Phys. Rev. E 81 (2010) 016323.
[3] G. Bellani, M.L. Byron, A.G. Collignon, C.R. Meyer, E.A. Variano, Shape effects on turbulent modulation by large nearly buoyant particles, J. Fluid Mech. 712 (2012) 41–60.
[4] S. Parsa, E. Calzavarini, F. Toschi, G.A. Voth, Rotation rate of rods in turbulent fluid flow, Phys. Rev. Lett. 109 (2012) 134501.
[5] H.I. Andersson, L. Zhao, M. Barri, Torque-coupling and particle-turbulence interactions, J. Fluid Mech. 696 (2012) 319–329.
[6] C. Nilsen, H.I. Andersson, Chaotic rotation of inertial spheroids in oscillating shear flow, Phys. Fluids 25 (2013) 013303.
[7] H.I. Andersson, A. Soldati, Anisotropic particles in turbulence: status and outlook, Acta Mech. 224 (2013) 2219–2223.
[8] D. Qi, L.-S. Luo, Rotational and orientational behaviour of three-dimensional spheroidal particles in Couette flows, J. Fluid Mech. 477 (2003) 201–213.
[9] A.N. Mody, M.R. King, Three-dimensional simulations of a platelet-shaped spheroid near a wall in shear flow, Phys. Fluids 17 (2005) 113302.
[10] Ö. Savaş, On flow visualization using reflective flakes, J. Fluid Mech. 152 (1985) 235–248.
[11] G. Gauthier, P. Gondret, M. Rabaud, Motions of anisotropic particles: application to visualization of three-dimensional flows, Phys. Fluids 10 (1998) 2147–2154.
[12] A.M. Philippe, C. Baravian, M. Jenny, F. Meneau, L.J. Michot, Taylor–Couette instability in anisotropic clay suspensions measured using small-angle x-ray scattering, Phys. Rev. Lett. 108 (2012) 254501.
[13] G.B. Jeffery, The motion of ellipsoidal particles immersed in a viscous fluid, Proc. R. Soc. Lond. A 102 (1922) 161–179.
[14] L.G. Leal, E.J. Hinch, The rheology of a suspension of nearly spherical particles subject to Brownian motions, J. Fluid Mech. 55 (1972) 745–765.
[15] H.L. Goldsmith, S.G. Mason, Particle motions in sheared suspensions XIII. The spin and rotation of disks, J. Fluid Mech. 12 (1962) 88–96.
[16] J.R. Angilella, On the orientation of flat triaxial objects in shear flows, in: 2nd COST FP1005 Workshop on “Fibre Suspension Flow Modelling”, Nancy, France, 13–14 October 2011, http://www.fp1005.cism.it/presentations/nancy/JeanRegisAngilella.pdf.
[17] Z. Yu, N. Phan-Thien, R.I. Tanner, Rotation of a spheroid in a Couette flow at moderate Reynolds numbers, Phys. Rev. E 76 (2007) 026310.
[18] H. Huang, X. Yang, M. Krafczyk, X.-Y. Lu, Rotation of spheroidal particles in Couette flows, J. Fluid Mech. 692 (2012) 369–394.
[19] J. Einarsson, J.R. Angilella, B. Mehlig, Orientation dynamics of weakly inertial axisymmetric particles in steady viscous flow, Physica D 278–279 (2014) 79–85.
[20] H. Goldstein, Classical Mechanics, 2nd ed., Addison-Wesley, Reading, MA, 1980, “The Euler angles” and “Euler angles in alternate conventions”, §4-4 and Appendix B, pp. 143–148, 606–610.
[21] http://mathworld.wolfram.com/EulerAngles.html.
[22] I. Gallily, A.-H. Cohen, On the orderly nature of the motion of nonspherical aerosol particles II. Inertial collision between a spherical large droplet and an axially symmetrical elongated particle, J. Colloid Interface Sci. 68 (1979) 338–356.
[23] L. Zhao, H.I. Andersson, On particle spin in two-way coupled turbulent channel flow simulations, Phys. Fluids 23 (2011) 093302.
[24] M. Shapiro, M. Goldenberg, Deposition of glass fiber particles from turbulent air flow in a pipe, J. Aerosol Sci. 24 (1993) 65–87.
[25] http://www.mathworks.se/help/matlab/ordinary-differential-equations.html.
[26] F. Lundell, The effect of particle inertia on triaxial ellipsoids in creeping shear: from drift toward chaos to a single periodic solution, Phys. Fluids 23 (2011) 011704.

Article 2

Orientation and rotation of inertial disk particles in wall turbulence

Niranjan Reddy Challabotla, Lihao Zhao & Helge I. Andersson

Journal of Fluid Mechanics, **776**, R2, 2015.

Article 3

Shape effects on dynamics of inertia-free spheroids in wall turbulence

Niranjan Reddy Challabotla, Lihao Zhao & Helge I. Andersson

Physics of Fluids, **27**, 61703, 2015.

PHYSICS OF FLUIDS **27**, 061703 (2015)

Shape effects on dynamics of inertia-free spheroids in wall turbulence

Niranjan Reddy Challabotla, Lihao Zhao, and Helge I. Andersson
Department of Energy and Process Engineering, Norwegian University of Science and Technology (NTNU), 7491 Trondheim, Norway

(Received 23 March 2015; accepted 5 June 2015; published online 22 June 2015)

The rotational motion of inertia-free spheroids has been studied in a numerically simulated turbulent channel flow. Although inertia-free spheroids were translated as tracers with the flow, neither the disk-like nor the rod-like particles adapted to the fluid rotation. The flattest disks preferentially aligned their symmetry axes normal to the wall, whereas the longest rods were parallel with the wall. The shape-dependence of the particle orientations carried over to the particle rotation such that the mean spin was reduced with increasing departure from sphericity. The streamwise spin fluctuations were enhanced due to asphericity, but substantially more for prolate than for oblate spheroids. © *2015 AIP Publishing LLC.* [http://dx.doi.org/10.1063/1.4922864]

Understanding the dynamics of non-spherical particles suspended in turbulent flows is a key in making advances in several engineering and environmental applications such as clouds in the atmosphere, plankton dynamics in the ocean, combustion systems, and paper making, to name a few. Non-spherical particles react on turbulent flow structures in complex ways which depend both on particle shape and inertia. Inertia-free particles with size smaller than the Kolmogorov length scale are expected to behave as tracers which passively follow the fluid motion, whereas inertial particles will have trajectories different from those of tracer particles in the same flow field. A bi-axial ellipsoid, i.e., a spheroid, is widely adopted to closely represent non-spherical particles and the shape of a spheroid is readily parameterized by the aspect ratio $\lambda = 2b/2a$ defined as the ratio between the symmetry axis and the two equal axes.

The dynamics of inertia-free spheroidal particles in homogeneous isotropic turbulence has been subject to several numerical studies[1–6] and also a few experimental investigations.[7–9] It has been observed that disk-like particles tumble more than rod-like particles.[4,5,7,8] Rod-like particles preferentially align with the fluid vorticity vector and the vorticity component along the rod axis does not contribute to their tumbling.[2,3,6,7] In contrast to the rod-like particles, disks align perpendicular to the fluid vorticity vector and this preferential orientation results in higher tumbling rates.[5,9] The Lagrangian fluid stretching in turbulence aligns the major axis of an anisotropic particle with the fluid vorticity.[6] The variance of the total rotation rate of a spheroidal particle is almost independent of the particle shape.[4] Strong effects of particle shape on tumbling and spinning were reported for small deviations from spherical shape in the range of $0.1 < \lambda < 10$. The particle rotation rates turned out to be almost insensitive to the changes in particle shape outside of this interval.[4]

Recently, orientation statistics, settling velocities,[10] and collision rates[11] of inertial spheroids in decaying isotropic turbulence were reported from direct numerical simulations (DNSs). However, the majority of previous studies on dynamics of inertial spheroidal particles have been performed in turbulent channel flows. In particular, the dynamical behaviour of inertial rod-like particles has been explored by means of DNS along with the Lagrangian point-particle methodology.[12–17] The orientational and rotational dynamics of inertial disk-like particles in channel flow turbulence have only very recently been reported.[18] In all these studies, the spheroidal particles were characterized by the aspect ratio λ and a Stokes number, St, based on the viscous time scale. For St ≤ 1, the orientation of rod-like particles ($\lambda > 1$) was essentially independent of the particle inertia[17] and the particles almost passively followed the fluid motion. Most earlier studies focused on spheroids with little

($0 < \mathrm{St} \leq 1$) and moderate ($1 < \mathrm{St} < 100$) inertia. Inertia effects on particle dynamics were substantial for $\mathrm{St} > 1$, whereas shape effects were significant for $\mathrm{St} \leq 1$. The orientation of inertia-free rods $\mathrm{St} = 0$ has been addressed by means of alternative approaches based on a Fokker-Planck-type equation[19] or second-moments of the fiber orientation vector[20] and a detailed comparison between these two methods was made by Gillissen *et al.*[21]

This letter presents results for inertia-free spheroidal particles suspended in a turbulent channel flow. Although the inertia-free spheroids passively translate along with the fluid, the particle orientation and rotation strongly depend on the particle shape. Earlier studies have focused on either prolate ($\lambda > 1$) or oblate ($\lambda < 1$) inertial spheroids. In the present study of inertia-free spheroids, a wide range of aspect ratios from 0.01 to 50, i.e., from flat disks to long rods, is covered for the first time in order to provide a comprehensive coverage of the shape effects on the particle dynamics.

We adopt an Eulerian-Lagrangian approach to study the dynamics of inertia-free spheroidal particles suspended in a fully developed turbulent channel flow. The continuous fluid phase is governed by the incompressible Navier-Stokes equations that are integrated numerically in a DNS approach with the same Navier-Stokes solver as in our earlier studies.[13,16]

Inertia-free spheroidal point-particles are suspended in the continuous fluid flow similarly as in several earlier studies.[12–18] The translational motion of the spheroids coincides with the fluid flow and the rotational motion adjusts such that the Jeffery-torques[22] vanish exactly, i.e.,

$$\begin{aligned} \omega'_x &= -\Lambda S'_{yz} + \Omega'_x, \\ \omega'_y &= \Lambda S'_{xz} + \Omega'_y, \\ \omega'_z &= \Omega'_z. \end{aligned} \tag{1}$$

This set of equations demonstrates the coupling between the particle rotation vector ω'_i, fluid rotation vector Ω'_i, and the fluid strain rate tensor S'_{ij}. The shape parameter $\Lambda = (\lambda^2 - 1)/(\lambda^2 + 1)$ is a measure of the degree of asphericity and $\Lambda = 0$ for spheres. Equation (1) is formulated in the particle frame-of-reference $\boldsymbol{x}' = \langle x', y', z' \rangle$ with origin at the particle center of mass and coordinate axes aligned with the principal directions of inertia.

The frictional Reynolds number based on the channel half-height h and the friction velocity u_τ is $Re_\tau = 180$. The friction velocity is defined in terms of the wall shear stress τ_w as $u_\tau = (\tau_w/\rho)^{1/2}$, where τ_w is proportional with the prescribed driving mean pressure gradient. All variables are normalized by viscous scales for velocity (u_τ), length (ν/u_τ), and time (ν/u_τ^2). The size of the computational domain is $12h \times 6h \times 2h$ in the streamwise, spanwise, and wall-normal directions, respectively, and 192 grid points are used in each direction. The grid resolution in the streamwise and spanwise directions becomes $\Delta x^+ = 11.3$ and $\Delta y^+ = 5.6$, while the non-uniform grid spacing in the wall-normal direction varies from $\Delta z^+ = 0.9$ next to the walls to 2.86 in the channel center. The time integration is performed with a constant time step $\Delta t^+ = 0.036$. Periodic boundary conditions are used in the two homogeneous directions and no-slip and impermeability conditions are imposed at the channel walls.

The suspension of spheroids is assumed to be dilute and the particle size is smaller than the Kolmogorov length. These assumptions justify the one-way coupled simulation where the feedback from the spheroidal particles on the fluid phase is ignored as well as neglection of particle-particle collisions and the use of the Jeffery torques. Particle-wall collisions are fully elastic so that a spheroid keeps its linear and angular momentum in the two homogeneous directions after a collision. A collision occurs every time the center of a spheroid comes closer to the wall than a distance equal to the semi-axis a. Simulations of inertia-free spheroids ($\mathrm{St} = 0$) are performed for seven different particle shapes $\lambda = 0.01, 0.33, 0.5, 1, 3, 10$, and 50 all with $a^+ = 0.36$. At time $t^+ = 0$, 500 000 spheroids of each shape are randomly injected into the same turbulence field. Orientational and rotational particle statistics are computed by averaging instantaneous data in time between $720\,\nu/u_\tau^2$ and $2520\,\nu/u_\tau^2$ and also in the homogeneous streamwise and spanwise directions. Particle-wall collisions are rare with only about 5 collisions with each of the walls during a viscous time unit (ν/u_τ^2).

Inertia-free spheroidal particles translate passively along with the local fluid irrespective of particle shape. However, the shape parameterized by λ or Λ has a strong influence on particle orientation and the rotation dynamics, as illustrated by the instantaneous plots in Figure 1. In contrast to the

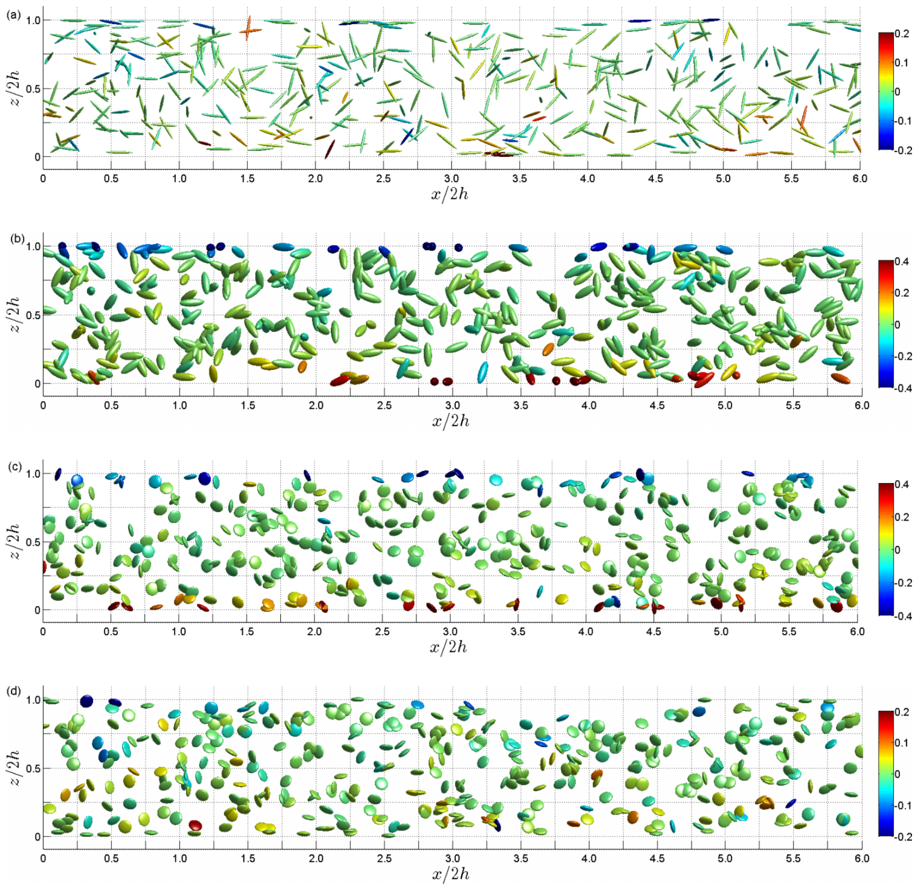

FIG. 1. Instantaneous distribution of rod-like particles with aspect ratios (a) $\lambda = 50$ and (b) $\lambda = 3$ and disk-like particles with aspect ratios (c) $\lambda = 0.5$ and (d) $\lambda = 0.01$. The spheroidal particles are projected into the (x, z)-plane and the shape reflects the particle orientation and colour-coding indicates the particles' spanwise angular velocity ω_y normalized by the viscous time scale.

preferential concentration of inertial spheroids,[13,16,18] the present inertia-free particles are uniformly distributed across the channel. Randomly orientated spheroids can be observed in the central region of the channel and attributed to the almost isotropic fluid vorticity.[23] The shape effect becomes essential away from the core region of the channel and, in particular, in the near-wall regions where the vorticity field is highly anisotropic. The preferential orientation of the rod-like particles in Figures 1(a) and 1(b) is qualitatively different from the preferential orientation of the disk-like particles in Figs. 1(c) and 1(d). The longest rods with aspect ratio $\lambda = 50$ exhibit a strong preferential alignment in the streamwise direction which is hardly observed for $\lambda = 3$. Similarly, disks with $\lambda = 0.01$ show a strong preferential orientation with their symmetry axis in the wall-normal direction and this tendency is also reduced for $\lambda = 0.5$. The colour-coding reveals that the highest rates of spanwise rotation occur in the vicinity of the channel walls, obviously associated with the high level of fluid vorticity. To further address the role of the particle shape on the particle dynamics, orientational and rotational statistics are presented next.

The variations of the absolute values of the mean direction cosines from the wall to the channel center are shown in Figure 2 for the entire range of aspect ratios from $\lambda = 0.01$ to 50. A direction cosine $\cos\theta_i$ is defined as the projection of the particle orientation unit vector onto the x_i-direction. Throughout the viscous sub-layer and the buffer layer which extends to $z^+ \approx 30$, rod-like particles are orientated distinctly different from disk-like particles. It can be observed from Figure 2(a) that the preferred orientation of the spheroids varies monotonically from misalignment towards

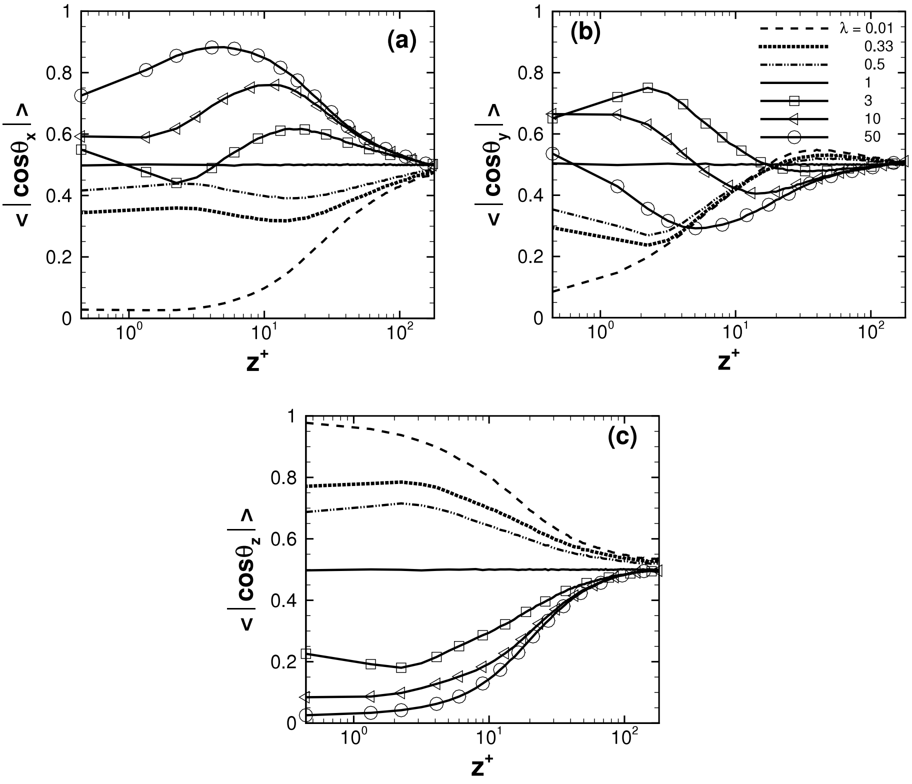

FIG. 2. The mean absolute values of the direction cosines $\langle|\cos\theta_i|\rangle$ for seven different particle aspect ratios λ. (a) Streamwise direction, (b) spanwise direction, and (c) wall-normal direction.

alignment in the streamwise direction as the aspect ratio increases from 0.01 to 50. The flattest disks (λ = 0.01) are preferentially orientated perpendicular to the flow direction, whereas the longest rods with λ = 50 are preferentially aligned with the mean flow. The opposite trend is observed in Figure 2(c), which shows that the flattest inertia-free disks preferentially align their symmetry axes normal to the wall. This tendency is gradually weakened as the flatness is reduced and the shape approaches that of a sphere. This finding is consistent with an observation made by Gustavsson *et al.*[5] that inertia-free disks in homogeneous isotropic turbulence preferentially align their symmetry axes orthogonal to the fluid vorticity vector. However, Challabotla *et al.*[18] reported that inertial disks exhibited a strong preferential orientation in the spanwise direction, i.e., $|\cos\theta_y| \approx 1$, whereas the flattest disks (λ = 0.01) with only modest inertia (St = 1) surprisingly exhibited a strong preference for wall-normal orientation, i.e., in keeping with $|\cos\theta_z| \approx 1$ for the present inertia-free disks.

Less clear-cut variations are seen in Figure 2(b). Rod-like spheroids in the viscous sub-layer $z^+ < 5$ exhibit a preferential orientation in the spanwise direction for moderate aspect ratios λ = 3 and 10, whereas the longest rods mostly align themselves in the streamwise direction. These observations for inertia-free spheroids agree with earlier findings[13,14,17] for low-inertia rod-like particles (St ≤ 1). In the core region of the channel, however, $|\cos\theta_x| \approx |\cos\theta_y| \approx |\cos\theta_z| \approx 0.5$ irrespective of particle shape. This suggests that both inertia-free rods and disks orient themselves randomly in the almost isotropic vorticity field.

The strongly anisotropic fluid vorticity field in the near-wall region,[23] in combination with the preferential particle orientations observed in Fig. 2, makes the rotational dynamics of the spheroidal particles crucially shape-dependent. The mean particle spin or angular velocity about the spanwise axis is shown in Figure 3(a), whereas the mean spin in the two other directions is zero. An exceptionally strong shape effect on $\langle\omega_y\rangle$ is seen in the vicinity of the walls, but this shape dependency gradually fades away outside of the buffer region. The spherical particles rotate faster than any of

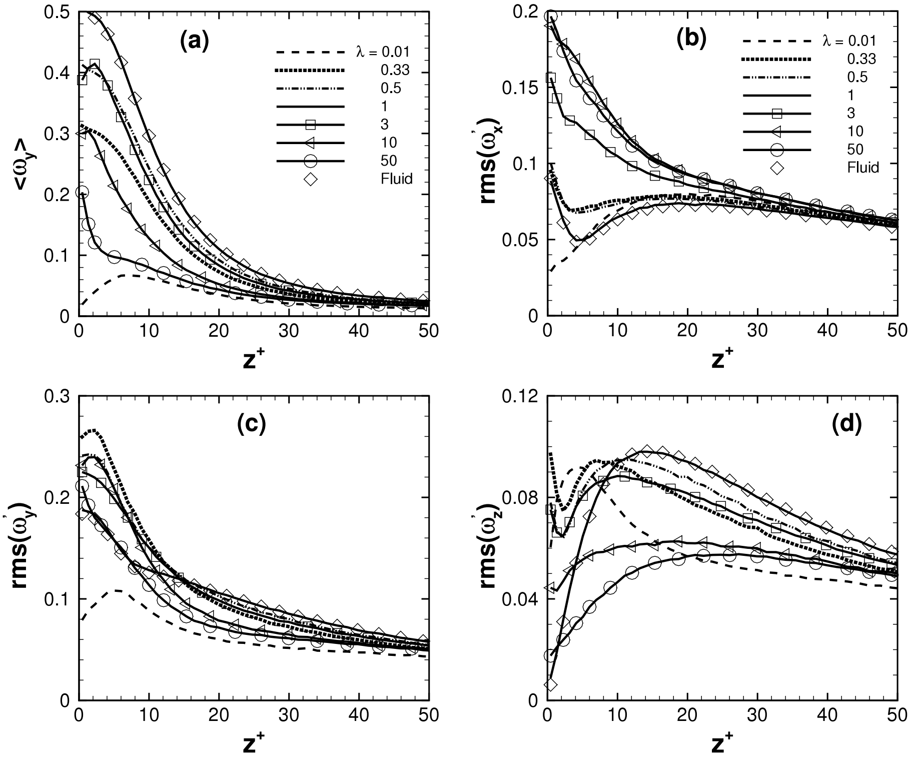

FIG. 3. Mean and fluctuating particle angular velocity components normalized by the viscous time scale. The corresponding fluid vorticity components are shown as ◊ symbols. (a) Mean spanwise angular velocity $\langle \omega_y \rangle$, (b) angular velocity fluctuations in the streamwise direction rms(ω'_x), (c) angular velocity fluctuations in the spanwise direction rms(ω'_y), and (d) angular velocity fluctuations in the wall-normal direction rms(ω'_z).

the other particle shapes and the spinning of the inertia-free spheres inevitably matches the fluid spin. The mean spin decreases with increasing asphericity Λ and the flattest disks (λ = 0.01) and the longest rods (λ = 50) rotate substantially slower than the spheres. This phenomenon can be attributed to their preferential orientation. The strong preferential orientation of highly aspherical spheroids, i.e., $|\Lambda| \approx 1$, makes the observed orientation and rotation in the viscous sub-layer qualitatively consistent with spheroids in Jeffery orbits in linear shear flow. Voth[24] argued that disk-shaped particles in orbits that bring their symmetry axis near the wall-normal direction will spend a long time in this orientation before tumbling. Here, we similarly observed that rod-like particles orbiting with their symmetry axis almost aligned in the streamwise direction rarely tumble. The substantial reduction of the mean spin of spheroids with high asphericity can therefore be attributed to Jeffery-like orbiting.

Figures 3(b)–3(d) show the shape dependence of the particle angular velocity fluctuations. The distinct shape effects on the root-mean-square (rms) values gradually diminish with the distance from the wall, as did the mean spin. From Figure 3(b), we observe that aspherical particles, i.e., λ ≠ 1, exhibit stronger fluctuations of the streamwise angular velocity ω_x than spheres in the buffer region and in the logarithmic region. This phenomenon cannot be caused by the particles' preferential sampling of low- or high-vorticity regions since the present inertia-free particles do not concentrate preferentially but are evenly distributed throughout the fluid. From Figure 2(a), we learned that the longer (λ ≥ 10) rod-like spheroids aligned in the streamwise direction. This preferential orientation enables the high level of spin about the x-axis of the long rods as compared with the shorter λ = 3 particles and the oblate spheroids.

More complex shapes effects are observed in Figures 3(c) and 3(d). In general, however, the spin fluctuations in the spanwise and wall-normal directions tend to decrease outside of $z^+ \approx 15$ with increasing asphericity Λ, i.e., as the rod-like particles become longer and the disk-like particles become flatter. The strong spin anisotropy observed in the near-wall region is obviously a combined effect of the anisotropic fluid vorticity and the preferential particle orientation.

In this letter, orientation and rotation statistics of inertia-free spherodial particles in wall-bounded turbulence have been reported. Seven different spheroidal tracers were considered, ranging from oblate disk-like particles ($\lambda = 0.01$) to prolate rod-like particles with $\lambda = 50$. The flattest disks were strongly aligned in the wall-normal direction, whereas the longest rods aligned themselves with the wall. The inertia-free particles were evenly distributed across the channel, but the shape-dependence of their preferred orientations carried over to their angular velocities. The strong mean spanwise spin observed for spherical particles ($\lambda = 1$) decreased with increasing asphericity both for rod-like and disk-like spheroids. The anisotropic mean and fluctuating fluid vorticity resulted in particle spin anisotropies which exhibited a complex dependence on λ caused by the shape-dependent preferential orientation of the spheroidal particles. The substantial reduction of the mean spin of spheroids with high asphericity was attributed to Jeffery-like orbiting.

This study has been supported by the Research Council of Norway through research fellowships to N.R.C. and L.Z.(Project No. 213917/F20 Turbulent Particle Suspensions) and grants of computing time (Programme for Supercomputing). COST Action FP1005 is gratefully acknowledged.

[1] M. Shin and D. L. Koch, "Rotational and translational dispersion of fibres in isotropic turbulent flows," J. Fluid Mech. **540**, 143 (2005).
[2] A. Pumir and M. Wilkinson, "Orientation statistics of small particles in turbulence," New J. Phys. **13**, 093030 (2011).
[3] L. Chevillard and C. Meneveau, "Orientation dynamics of small, triaxial–ellipsoidal particles in isotropic turbulence," J. Fluid Mech. **737**, 571 (2013).
[4] M. Byron, J. Einarsson, K. Gustavsson, G. Voth, B. Mehlig, and E. Variano, "Shape-dependence of particle rotation in isotropic turbulence," Phys. Fluids **27**, 035101 (2015).
[5] K. Gustavsson, J. Einarsson, and B. Mehlig, "Tumbling of small axisymmetric particles in random and turbulent flows," Phys. Rev. Lett. **112**, 014501 (2014).
[6] R. Ni, N. T. Ouellette, and G. A. Voth, "Alignment of vorticity and rods with Lagrangian fluid stretching in turbulence," J. Fluid Mech. **743**, R3 (2014).
[7] G. G. Marcus, S. Parsa, S. Kramel, R. Ni, and G. A. Voth, "Measurements of the solid-body rotation of anisotropic particles in 3D turbulence," New J. Phys. **16**, 102001 (2014).
[8] S. Parsa, E. Calzavarini, F. Toschi, and G. A. Voth, "Rotation rate of rods in turbulent fluid flow," Phys. Rev. Lett. **109**, 134501 (2012).
[9] R. Ni, S. Kramel, N. T. Ouellette, and G. A. Voth, "Measurements of the coupling between the tumbling of rods and the velocity gradient tensor in turbulence," J. Fluid Mech. **766**, 202 (2015).
[10] C. Siewert, R. P. J. Kunnen, M. Meinke, and W. Schröder, "Orientation statistics and settling velocity of ellipsoids in decaying turbulence," Atmos. Res. **142**, 45 (2014).
[11] C. Siewert, R. P. J. Kunnen, and W. Schröder, "Collision rates of small ellipsoids settling in turbulence," J. Fluid Mech. **758**, 686 (2014).
[12] H. Zhang, G. Ahmadi, F.-G. Fan, and J. B. McLaughlin, "Ellipsoidal particles transport and deposition in turbulent channel flows," Int. J. Multiphase Flow **27**, 971 (2001).
[13] P. H. Mortensen, H. I. Andersson, J. J. J. Gillissen, and B. J. Boersma, "Dynamics of prolate ellipsoidal particles in a turbulent channel flow," Phys. Fluids **20**, 093302 (2008).
[14] C. Marchioli, M. Fantoni, and A. Soldati, "Orientation, distribution, and deposition of elongated, inertial fibers in turbulent channel flow," Phys. Fluids **22**, 033301 (2010).
[15] C. Marchioli and A. Soldati, "Rotation statistics of fibers in wall shear turbulence," Acta Mech. **224**, 2311 (2013).
[16] L. Zhao, C. Marchioli, and H. I. Andersson, "Slip velocity of rigid fibers in turbulent channel flow," Phys. Fluids **26**, 063302 (2014).
[17] L. H. Zhao, H. I. Andersson, and J. J. J. Gillissen, "On inertial effects of long fibers in wall turbulence: Fiber orientation and fiber stresses," Acta Mech. **224**, 2375 (2013).
[18] N. R. Challabotla, L. Zhao, and H. I. Andersson, "Orientation and rotation of inertial disk particles in wall turbulence," J. Fluid Mech. **766**, R2 (2015).
[19] M. Manhart, "Rheology of suspensions of rigid-rod like particles in turbulent channel flow," J. Non-Newtonian Fluid Mech. **112**, 269 (2003).
[20] J. S. Paschkewitz, C. D. Dimitropoulos, Y. X. Hou, V. S. R. Somandepalli, M. G. Mungal, E. S. G. Shaqfeh, and P. Moin, "An experimental and numerical investigation of drag reduction in a turbulent boundary layer using a rigid rodlike polymer," Phys. Fluids **17**, 085101 (2005).
[21] J. J. J. Gillissen, B. J. Boersma, P. H. Mortensen, and H. I. Andersson, "On the performance of the moment approximation for the numerical computation of fiber stress in turbulent channel flow," Phys. Fluids **19**, 035102 (2007).
[22] G. B. Jeffery, "The motion of ellipsoidal particles immersed in a viscous fluid," Proc. R. Soc. A **102**, 161 (1922).
[23] H. I. Andersson, L. Zhao, and E. A. Variano, "On the anisotropic vorticity in turbulent channel flows," ASME J. Fluids Eng. **137**, 084503 (2015).
[24] G. A. Voth, "Disks aligned in a turbulent channel," J. Fluid Mech. **772**, 1 (2015).

Article 4

Rotation of nonspherical particles in turbulent channel flow

Lihao Zhao, Niranjan Reddy Challabotla, Evan A. Variano & Helge I. Andersson

Physical Review Letters, **115**, 244501, 2015.

PRL **115,** 244501 (2015) PHYSICAL REVIEW LETTERS week ending 11 DECEMBER 2015

Rotation of Nonspherical Particles in Turbulent Channel Flow

Lihao Zhao,[1] Niranjan Reddy Challabotla,[1] Helge I. Andersson,[1] and Evan A. Variano[2]
[1]*Department of Energy and Process Engineering, Norwegian University of Science and Technology, 7491 Trondheim, Norway*
[2]*Department of Civil and Environmental Engineering, University of California, Berkeley, California 94720, USA*

(Received 25 February 2015; published 11 December 2015)

The effects of particle inertia, particle shape, and fluid shear on particle rotation are examined using direct numerical simulation of turbulent channel flow. Particles at the channel center (nearly isotropic turbulence) and near the wall (highly sheared flow) show different rotation patterns and surprisingly different effects of particle inertia. Oblate particles at the center tend to rotate orthogonally to their symmetry axes, whereas prolate particles rotate around their symmetry axes. This trend is weakened by increasing inertia so that highly inertial oblate spheroids rotate nearly isotropically about their principle axes at the channel center. Near the walls, inertia does not move the rotation of spheroids towards isotropy but, rather, reverses the trend, causing oblate spheroids to rotate strongly about their symmetry axes and prolate spheroids to rotate normal to their symmetry axes. The observed phenomena are mostly ascribed to preferential orientations of the spheroids.

DOI: 10.1103/PhysRevLett.115.244501 PACS numbers: 47.55.Kf, 47.27.ek, 47.27.nd

Aspherical particles are encountered in many natural and industrial processes: sediment transport in estuaries [1], ice crystals in the atmosphere [2,3], pulp fibers in paper making [4], and planktonic and swimming microorganisms in the ocean [5,6]. Furthermore, all of these example particles have non-negligible inertia, meaning that they do not instantly adjust to equilibrium with the dynamic behavior of the fluids in which they are embedded.

Previous studies have revealed the dynamics of inertia-free aspherical particles in homogeneous isotropic turbulence [7–14]. These have shown particles to preferentially align with respect to fluid vorticity and/or strain, which causes particle rotation to differ from that of fluid parcels, even though the particles are noninertial. Specifically, rods tend to align their symmetry axis with the local fluid vorticity vector, which leads them to rotate preferentially around their symmetry axis [9]. Disks align one of their long axes with the local fluid vorticity, leading to minimal rotation about their symmetry axis. In other words, “rods spin and disks tumble” [13].

Inertial particles have been investigated in homogeneous isotropic turbulence [15,16] and (more commonly) in turbulent channel flow [17–22]. Analysis has focused on particle clustering, turbophoresis, and particle motion. The analyses of particle motion in channel flow have been conducted entirely in the laboratory frame and have not yet considered the interesting behavior that can be seen by examining particle motion with respect to their principle axes.

These recent studies leave the following questions unanswered: To what extent will particle inertia affect the partition between tumbling and spinning in homogeneous isotropic turbulence? How does strong fluid shear change the tumbling and spinning? Does the tumbling and spinning of spheroids seen in isotropic turbulence also occur in the nearly isotropic core region of a turbulent channel flow? Finally, do aspherical particles orient preferentially, and if so, where?

In this Letter, we, therefore, examine the motion of aspherical inertial particles in turbulent channel flow with respect to their local axes. Channel flow allows us to examine the transition in behavior from nearly isotropic turbulence at the channel center to highly sheared anisotropic turbulence near the channel wall. In this flow, we consider the combined effects of particle shape (from oblate to prolate) and particle inertia. These results serve to extend and unite the hitherto disparate studies of channel flow and homogeneous isotropic turbulence.

Direct numerical simulation (DNS) with a pseudospectral method was performed to simulate a turbulent channel flow closely matching that of Kim *et al.* [23]. The flow is periodic in streamwise (x) and cross-stream (y) directions and has no-slip boundaries at the top and bottom walls. The Reynolds number is based on the wall friction velocity (u_τ), and the channel half-height (h) is 180 [18,21]. We consider two regions of the flow: a region near the channel center ($z^+ = 180$), where turbulence is nearly homogeneous and isotropic [24], and a region near the channel wall ($z^+ = 10$), which is in the buffer layer. At this location, the flow has a strong mean shear, large values for the Reynolds shear stress -$\langle uw \rangle$, and the velocity fluctuation magnitudes are maximized.

In the simulation, swarms of 500 000 noninteracting particles of each type are randomly injected into the fully developed turbulent channel flow at $t^+ = 0$ (t^+ is normalized by the wall-shear time scale νu_τ^{-2}), and the statistics are computed by averaging instantaneous data in homogeneous directions over a time window of $7200 < t^+ < 9000$ for inertial spheroids and $720 < t^+ < 2520$ for tracer spheroids. The particle motion is computed using a one-way coupling scheme, in which Lagrangian particle paths in the Eulerian DNS field are determined using Newtonian mechanics. Forces and torques acting on a spheroid are taken from Brenner [25] and Jeffery [26], respectively, who give expressions assuming steady flow in the creeping flow regime. These drag-type forces are the only ones considered in the present study; gravity, added mass force, and history force are considered second order in importance. All particle dimensions are smaller than (or on the order of) the Kolmogorov length scale. The numerical methods and validation are described in Ref. [18] for prolate spheroids and Ref. [21] for oblate spheroids.

The translational Stokes numbers (St) are derived based on a particle time scale (τ) that assumes isotropic particle orientation relative to the ambient flow [18,21,27]:

$$\tau = \begin{cases} \frac{2Da^2}{9\nu}\frac{\lambda\{\pi - 2tan^{-1}[\lambda(1-\lambda^2)^{-1/2}]\}}{2(1-\lambda^2)^{\frac{1}{2}}} & \lambda \le 1 \\ \frac{2Da^2}{9\nu}\frac{\lambda \ln\left[\lambda + \sqrt{(\lambda^2-1)}\right]}{\sqrt{(\lambda^2-1)}} & \lambda \ge 1 \end{cases}, \qquad (1)$$

where D is the density ratio between particle and fluid, and the aspect ratio $\lambda = 2c/2a$ is the ratio between the symmetry axis (length $2c$) and the two equal axes (length $2a$). Particles are selected to sample a range of λ values, from 0.01 (oblate) to 50 (prolate). For each λ value, three different particle densities are considered in order to sample a range of translational Stokes numbers. The Stokes numbers are set to zero, 0.074, and 2.222 (based on the Kolmogorov time scale τ_η at the channel centerline) or, equivalently, to zero, 1, and 30 (based on the channel wall-shear time scale).

The rotational Stokes numbers differ from the translational ones, because the time scale over which a particle reaches rotational equilibrium with the surrounding flow depends on the moment-of-inertia tensor. A first-order calculation of rotational response time can be made by considering a flow with zero fluid strain and using the steady-flow torque equations of Jeffery [26] to examine a particle approaching equilibrium with the local flow. From this, we see that spheroids approach rotational equilibrium faster than they approach translational equilibrium, regardless of particle shape and which principle axis is being considered. For example, given three spheroids with identical translational relaxation times τ that are coming to rotational equilibrium about their symmetry axis (z'), a prolate spheroid (aspect ratio $\lambda = 10$) will come to rotational equilibrium in 0.13τ, a sphere (aspect ratio $\lambda = 1$) in 0.3τ, and an oblate spheroid (aspect ratio $\lambda = 0.1$) in 0.4τ.

Let ω_i and Ω_i denote the angular velocity of a particle and a fluid element, respectively. We decompose the particle enstrophy ($\langle\omega_i\omega_i\rangle$) into "spin" and "tumbling" components, where spin describes only the rotation about a spheroid's symmetry axis (z') as $\langle\omega_{z'}\omega_{z'}\rangle$, and tumbling describes rotation about the other two axes (x' and y') as $\langle\omega_{x'}\omega_{x'}\rangle + \langle\omega_{y'}\omega_{y'}\rangle$. We observe from Fig. 1(a) that for $\mathrm{St} = 0$ particles at the channel center, oblate spheroids tumble more than prolate spheroids; this result is consistent with the previous findings in homogeneous isotropic turbulence [9–11,13]. The other results in Fig. 1 show that inertia reduces particle enstrophy and makes rotation more isotropic with respect to the particles' principle axes, i.e., weakening the tendency of disks to preferentially tumble and rods to preferentially spin. Figure 1(c) also shows that local fluid enstrophy decreases with increasing particle inertia, indicating that inertial spheroids preferentially sample regions of low fluid vorticity, in contrast to tracers which are distributed randomly.

Spheroids' tendency to emphasize specific components of rotation can be explained by examining their orientation relative to fluid vorticity; the inner product between a particle's orientation vector and the local fluid vorticity vector yields an angle α shown in Fig. 2 for the nearly isotropic channel center. For $\mathrm{St} = 0$ particles, the results replicate previous observations [8–14] for disks and rods. Disks tend to align with their symmetry axis (z') orthogonal to the fluid vorticity, causing strong tumbling [8–14] and

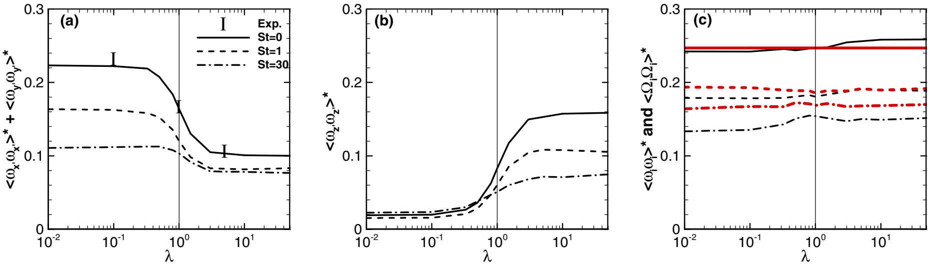

FIG. 1 (color online). Channel-center results of (a) tumbling components, (b) spinning component, and (c) total particle enstrophy versus aspect ratio λ. Tumbling (a) has a strong response to inertia for disks and a weak response to inertia for rods. Spinning (b) has a weak response to inertia for disks and a strong response to inertia for rods. The black lines and thick red lines (c) represent the particle enstrophy $\langle\omega_i\omega_i\rangle$ and the fluid enstrophy $\langle\Omega_i\Omega_i\rangle$ sampled by the particles (Eulerian fluid enstrophy is $0.247\tau_\eta^{-2}$), respectively. Star quantities are normalized with Kolmogorov time scale τ_η; symbols in (a) are laboratory data by Parsa *et al.* [9] and Marcus *et al.* [10].

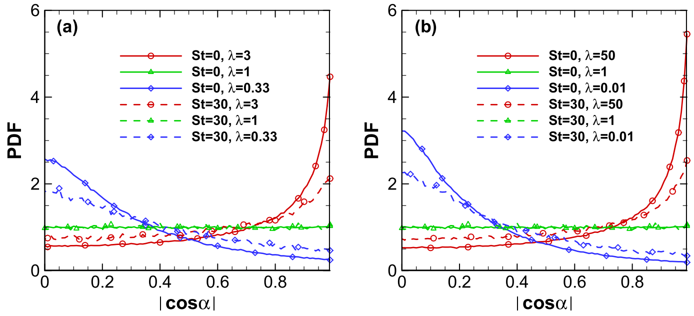

FIG. 2 (color online). Channel-center distributions of particles' instantaneous alignment α with local fluid vorticity for (a) moderate asphericity and (b) extreme asphericity. Solid lines are inertia-free; dashed lines are inertial. Blue lines with diamond symbols are disks, red lines with circle symbols are rods, and green lines with triangle symbols are spheres.

weak spinning [11,13]. Rods align parallel to local vorticity [8,10–14] and, thus, spin along with it. The most recent studies [12–14] also showed that the preferential alignment of the major axis of tracer spheroids in the direction of the fluid vorticity vector arises because both independently tend to align with the strongest Lagrangian stretching direction. This alignment effect becomes slightly stronger for particles with greater departure from sphericity, which can be seen by comparing corresponding lines between Figs. 2(a)and 2(b).

Increased particle inertia weakens the alignment effect for all shapes studied, making rods less likely to emphasize spinning and disks less likely to emphasize tumbling (Fig. 1). This tendency could be caused by two mechanisms. First, when inertial spheroids avoid sampling regions of strong vorticity [see Fig. 1(c)], they also avoid regions where they will experience strong alignment, because strain-vorticity alignment is strongest in the presence of strong vorticity [12,13]. Second, because inertial particles do not follow the flow passively [20,28,29] (even an inertial sphere does not rotate along with the local fluid rotation [28]), it is likely that spheroids' inertia induces a temporal filter on the rotational motion and, thus, prevents the particle from extracting all available vorticity from the flow. Roughly, inertial spheroids will not align with or rotate along with motions whose duration is less than the particle relaxation time, which leads to less alignment and less emphasis on either tumbling or spinning.

Results for the near-wall region ($z^+ = 10$) are seen in Fig. 3, which is analogous to Fig. 1 but shows very different behavior. Weakly inertial ($\mathrm{St} = 0$ and 1) disks tumble, especially when their aspect ratio is near 1, but they also exhibit a fair amount of spinning as well. Strongly inertial disks almost exclusively spin. Short and weakly inertial rods almost equally spin and tumble, and the amount of spinning increases with length. As inertia increases, both short and long rods emphasize tumbling more than spinning, which indicates that the inertia effect is more dominant than the shape effect.

Similar to the case of the channel center, particle enstrophy near the wall [black lines in Fig. 3(c)] is less than that of the surrounding fluid [thick red lines in Fig. 3(c)]. Unlike the channel center, however, near-wall particle enstrophy is strongly dependent on shape. Stronger asphericity leads to lower particle enstrophy. The effect of inertia

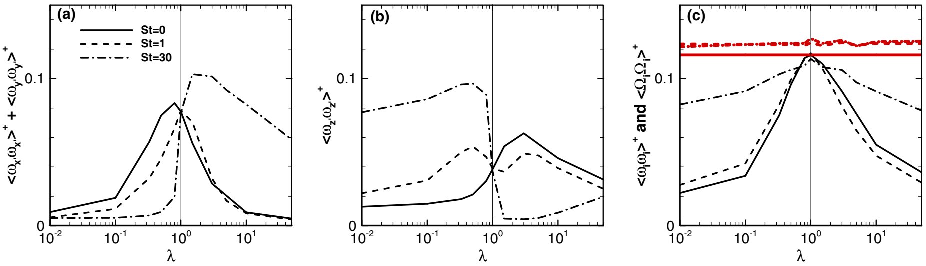

FIG. 3 (color online). Near-wall results of the (a) tumbling and (b) spinning component of particle enstrophy and (c) total particle and fluid enstrophy. The black lines and thick red lines (c) represent the particle enstrophy $\langle \omega_i \omega_i \rangle$ and the fluid enstrophy $\langle \Omega_i \Omega_i \rangle$ sampled by the particles, respectively. Plus quantities are normalized by $\nu^{-2} u_\tau^4$.

in the near-wall region (enstrophy increasing with particle inertia) is opposite to the case seen at the channel center (enstrophy decreasing with particle inertia). The thick red lines in Fig. 3(c) provide a partial explanation of this effect, showing that particle inertia causes spheroids to preferentially sample high-vorticity flow structures in the near-wall region. Such preferential sampling is related to particle clustering, and near-wall clustering has been discussed previously in the literature [20].

The preferential sampling seen near the wall is opposite to that at the channel center, suggesting that different mechanisms dominate particle clustering in isotropic turbulence than in highly sheared near-wall turbulence. Because both types of preferential sampling are shape independent [the thick red lines are nearly flat in Figs. 1(c) and 3(c)], our data suggest that the strong shape dependence of particle enstrophy in the near-wall region is caused by more than particle clustering. To explain this behavior, we examine spheroid alignment relative to local vorticity (Fig. 4). When their inertia is increased, disks will switch from perpendicular ($\mathrm{St} = 0$) to parallel ($\mathrm{St} = 30$) alignment relative to fluid vorticity [21] and, therefore, emphasize spinning induced by the mean fluid shear [Fig. 3(b)]. A similar effect is seen for rods: when their inertia is increased, rods switch from parallel (or partly parallel) [19,20,30] to perpendicular alignment relative to vorticity, thereby emphasizing tumbling [Fig. 3(a)].

Alignment between spheroids and fluid vorticity is caused by a different mechanism near the wall than in the channel center. Near the channel wall, the large mean velocity gradient $d\langle U\rangle/dz$ provides a strong mean vorticity in the cross-stream y direction, and the local turbulence field is anisotropic, with vorticity fluctuations being strongest in the y direction and weakest in the x direction [23,24]. Recent work on the rotational dynamics of a single oblate spheroid in a uniform shear flow revises the concept of Jeffery orbits to show that an inertial disk eventually rotates in the shear plane irrespective of its initial conditions [31]. Similarly, a prolate spheroid drifts towards rotation in the x-z plane [32]. Similar behaviors of inertial spheroids ($\mathrm{St} = 30$) in wall turbulence are observed here; i.e., disks emphasize spinning in the x-z plane (aligned with the vorticity vector), whereas rods emphasize tumbling in the x-z plane (aligned normal to the vorticity vector). These observations suggest that inertial spheroids in near-wall turbulence behave just like those in a linear shear flow. The likely reason is that the inertial spheroids filter the effect of small-scale turbulent fluctuations and only respond effectively to the largest flow structures and the mean shear. In other words, inertia causes the mean-shear effect to dominate the rotational dynamics of inertial spheroids in wall turbulence.

Tracer spheroids in the wall region, in contrast to inertial spheroids discussed above, exhibit more complex rotational dynamics, and their preferential alignment is caused by other mechanisms. First, we observe from Fig. 4(b) that inertia-free spheroids tend to align with their symmetry axis normal to the vorticity vector, typically in the streamwise direction. This preferential alignment is consistent with numerical [18–22] and experimental findings [30] in wall turbulence. However, the preferential orientation of the $\mathrm{St} = 0$ spheroids in the near-wall region cannot explain the emphasized tumbling or spinning; e.g., both tracer disks and rods only weakly tumble [Fig. 3(a)] even though they both align [Fig. 4(b)] normal to mean vorticity vector. This observation suggests that an inertia-free spheroid does not respond efficiently to mean shear. Recently, Voth [33] argued that a weakly inertial oblate spheroid aligned near the wall-normal direction will spend a long time in this orientation before tumbling. Challabotla *et al.* [34] similarly observed that prolate tracers with their symmetry axis almost aligned in the streamwise direction rarely tumble, and the observed orientation and rotation of tracer spheroids in the viscous sublayer was qualitatively consistent with spheroids in Jeffery orbits in linear shear flow. Thus, we conclude that the weak tumbling and spinning for inertia-free spheroids with a high aspect ratio can be attributed to Jeffery-like orbiting. However, the mechanism

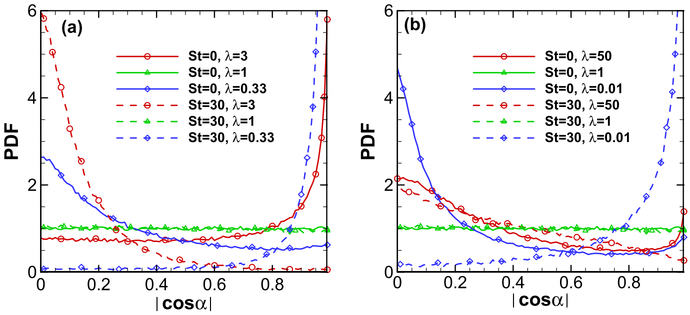

FIG. 4 (color online). Near-wall distributions of particles' instantaneous alignment α with local fluid vorticity for (a) moderate asphericity and (b) extreme asphericity. Solid lines are inertia-free; dashed lines are inertial. Blue lines with diamond symbols are disks, red lines with circle symbols are rods, and green lines with triangle symbols are spheres.

that aligns such particles preferentially in that orientation remains an open question.

A possible explanation for the preferential alignment is suggested by recent findings concerning preferential alignment of a spheroid's major axis in the Lagrangian strongest stretching direction in homogeneous isotropic turbulence [12,13]. Lagrangian coherent structures (LCSs) [35] act as organizers of transport in fluid flows having a clear impact on the particle trajectories [36]. Near-wall LCSs have been studied in channel flow turbulence [36–38] and "curved legs" of the coherent streamwise structure inclined in the streamwise direction with about 20° were reported [38]. In the present study, the major axis of the inertia-free spheroids and the near-wall quasistreamwise vortices' vector are both almost aligned in the streamwise x direction. Just as in the channel center, this preferred alignment of the spheroids with the quasistreamwise vortices makes disks tumble more than spin and rods spin more than tumble. We, therefore, hypothesize that the light spheroids are captured by, and partially move along with, the coherent vortices in the wall turbulence and, therefore, preferentially align in the streamwise direction.

In conclusion, we have explored rotation about the principle axes of spheroids suspended in turbulent channel flow. In the channel center, we have found that inertia-free spheroids were tumbling and spinning just as in homogeneous isotropic turbulence [9,10], whereas inertia reduced the preferential spinning or tumbling and led to a more isotropic rotation. This observation is likely caused by preferential clustering of the inertial spheroids in low-vorticity regions and inertial filtering of the local vorticity.

Spheroids in the wall region are affected both by mean shear and anisotropic fluid vorticity, and their rotational behavior is totally different from at channel center. We argue that inertial spheroids respond strongly to the mean shear, whereas inertia-free spheroids do not. The complex rotation of these tracers is a consequence of the preferential orientation of the inertia-free spheroids. We hypothesize that the preferential orientation of these particles is caused by interactions with the coherent vortex structures in wall turbulence.

This material is based upon work supported by the National Science Foundation under Grant No. OCE-1334788 (E. V.) and by the Research Council of Norway under Project No. 213917/F20 (H. I. A.) and Programme for Supercomputing. Support and motivation was provided by the Peder Sather Center for Advanced Study at University of California, Berkeley.

[1] A. J. Mehta, *An Introduction to Hydraulics of Fine Sediment Transport* (World Scientific Publishing Company, Singapore, 2013).
[2] R. A. Shaw, Annu. Rev. Fluid Mech. **35**, 183 (2003).
[3] A. Korolev and G. Isaac, J. Atmos. Sci. **60**, 1795 (2003).
[4] F. Lundell, L. D. Söderberg, and P. H. Alfredsson, Annu. Rev. Fluid Mech. **43**, 195 (2011).
[5] J. S. Guasto, R. Rusconi, and R. Stocker, Annu. Rev. Fluid Mech. **44**, 373 (2012).
[6] T. J. Pedley and J. O. Kessler, Annu. Rev. Fluid Mech. **24**, 313 (1992).
[7] M. Shin and D. L. Koch, J. Fluid Mech. **540**, 143 (2005).
[8] A. Pumir and M. Wilkinson, New J. Phys. **13**, 093030 (2011).
[9] S. Parsa, E. Calzavarini, F. Toschi, and G. A. Voth, Phys. Rev. Lett. **109**, 134501 (2012).
[10] G. G. Marcus, S. Parsa, S. Kramel, R. Ni, and G. A. Voth, New J. Phys. **16**, 102001 (2014).
[11] K. Gustavsson, J. Einarsson, and B. Mehlig, Phys. Rev. Lett. **112**, 014501 (2014).
[12] R. Ni, N. T. Ouellette, and G. A. Voth, J. Fluid Mech. **743**, R3 (2014).
[13] M. Byron, J. Einarsson, K. Gustavsson, G. Voth, B. Mehlig, and E. A. Variano, Phys. Fluids **27**, 035101 (2015).
[14] R. Ni, S. Kramel, N. T. Ouellette, and G. A. Voth, J. Fluid Mech. **766**, 202 (2015).
[15] C. Siewert, R. P. J. Kunnen, M. Meinke, and W. Schröder, Atmos. Res. **142**, 45 (2014).
[16] G. Bellani, M. L. Byron, A. G. Collignon, C. R. Meyer, and E. A. Variano, J. Fluid Mech. **712**, 41 (2012).
[17] H. Zhang, G. Ahmadi, F.-G. Fan, and J. B. McLaughlin, Int. J. Multiphase Flow **27**, 971 (2001).
[18] P. H. Mortensen, H. I. Andersson, J. J. J. Gillissen, and B. J. Boersma, Phys. Fluids **20**, 093302 (2008).
[19] C. Marchioli, M. Fantoni, and A. Soldati, Phys. Fluids **22**, 033301 (2010).
[20] L. Zhao, C. Marchioli, and H. I. Andersson, Phys. Fluids **26**, 063302 (2014).
[21] N. R. Challabotla, L. Zhao, and H. I. Andersson, J. Fluid Mech. **766**, R2 (2015).
[22] C. Marchioli and A. Soldati, Acta Mech. **224**, 2311 (2013).
[23] J. Kim, P. Moin, and R. Moser, J. Fluid Mech. **177**, 133 (1987).
[24] H. I. Andersson, L. Zhao, and E. Variano, ASME J. Fluids Eng. **137**, 084503 (2015).
[25] H. Brenner, Chem. Eng. Sci. **19**, 703 (1964).
[26] G. B. Jeffery, Proc. R. Soc. A **102**, 161 (1922).
[27] M. Shapiro and M. Goldenberg, J. Aerosol Sci. **24**, 65 (1993).
[28] P. H. Mortensen, H. I. Andersson, J. J. J. Gillissen, and B. J. Boersma, Phys. Fluids **19**, 078109 (2007).
[29] L. Zhao, C. Marchioli, and H. I. Andersson, Phys. Fluids **24**, 021705 (2012).
[30] A. Abbasi Hoseini, F. Lundell, and H. I. Andersson, Int. J. Multiphase Flow **76**, 13 (2015).
[31] N. R. Challabotla, C. Nilsen, and H. I. Andersson, Phys. Lett. A **379**, 157 (2015).
[32] F. Lundell and A. Carlsson, Phys. Rev. E **81**, 016323 (2010).
[33] G. Voth, J. Fluid Mech. **772**, 1 (2015).
[34] N. R. Challabotla, L. Zhao, and H. I. Andersson, Phys. Fluids **27**, 061703 (2015).
[35] G. Haller, Annu. Rev. Fluid Mech. **47**, 137 (2015).
[36] J. H. Bettencourt, C. Lopez, and E. Hernandez-Garcia. J. Phys. A **46**, 254022 (2013).
[37] M. A. Green, C. W. Rowley, and G. Haller, J. Fluid Mech. **572**, 111 (2007).
[38] Y. Yang and D. I. Pullin, J. Fluid Mech. **674**, 67 (2011).

Article 5

Gravity effects on fiber dynamics in wall turbulence

Niranjan Reddy Challabotla, Lihao Zhao & Helge I. Andersson

Flow, Turbulence and Combustion, **In press**, 2016.

Is not included due to copyright

Article 6

On fiber behavior in turbulent vertical channel flow

Lihao Zhao & H.I. Andersson

Chemical Engineering Science, **153**, 75-86, 2016.

Chemical Engineering Science 153 (2016) 75–86

Contents lists available at ScienceDirect

Chemical Engineering Science

journal homepage: www.elsevier.com/locate/ces

On fiber behavior in turbulent vertical channel flow

Niranjan Reddy Challabotla, Lihao Zhao*, Helge I. Andersson

Department of Energy and Process Engineering, Norwegian University of Science and Technology (NTNU), Trondheim, Norway

HIGHLIGHTS

- Dynamics of inertial fibers in turbulent vertical channel flow has been investigated.
- Eulerian–Lagrangian methodology was adopted to simulate fiber orientation and motion.
- The drift velocity of the fibers towards the wall was substantially higher in downward flow.
- Suppressed drift velocity in upward flow resulted in a more uniform fiber distribution.
- Presence of gravity induced preferential alignment of inertial fibers with flow direction at the channel center.

ARTICLE INFO

Article history:
Received 13 January 2016
Received in revised form
17 June 2016
Accepted 3 July 2016
Available online 5 July 2016

Keywords:
Fiber suspension
Turbulent flow
Gravity
Gas–solid flow
Direct Numerical Simulation
Eulerian–Lagrangian approach

ABSTRACT

In the present work, the dynamic behavior of inertial fibers suspended in a turbulent vertical channel flow has been investigated. The three-dimensional turbulent flow field was obtained from the Navier–Stokes equations by means of direct numerical simulation in an Eulerian reference frame. The fibers were modeled as prolate spheroidal particles in a Lagrangian frame and characterized by their inertia and shape. The translation and rotation of the individual fibers were governed by viscous forces and torques as well as by gravity and buoyancy according to Newton's laws of motion. The test matrix comprised four different Stokes numbers (inertia) and three different aspect ratios (shape). The twelve different fiber types were suspended both in a downward and in an upward channel flow. Fiber orientation and velocity statistics were compared with channel flow results in absence of gravity.

The results showed that gravity has a negligible effect for fibers with modest inertia, i.e. low Stokes numbers, whereas gravity turned out to have a major impact on the dynamics of highly inertial fibers. Irrespective of the bulk flow direction, a preferential alignment of the inertial fibers with the gravity force was found in the channel center where fibers have been known to orient randomly in absence of gravity. In the downward channel flow, the drift velocity of the fibers towards the walls was substantially higher for fibers than for spheres and also higher than when gravity was neglected. In the upward flow configuration, the modest drift velocity of inertial spheres was totally quenched for all fibers irrespective of shape. The suppressed drift velocity resulted in a more uniform fiber distribution throughout the channel as compared to the distinct near-wall accumulation in downward flow and in absence of gravity. This suggests that an upward flow configuration should be the preferred choice if a uniform fiber distribution is desired, as in a biomass combustion reactor.

1. Introduction

Turbulent suspension flows of non-spherical particles occur in many industrial, environmental, and biological applications such as in paper making processes (Lundell et al., 2011), fluidized bed reactors (Loranger et al., 2009), biomass combustion (Ma et al., 2007), aerosol transport (Kleinstreuer and Feng, 2013), pneumatic conveying (Hilton and Cleary, 2011), and phytoplankton transport in the ocean (Guasto et al., 2012). Studies of the dynamics of non-spherical particles in turbulent flows play an important role in the advancement of design of industrial processes and better understanding of natural processes. In the literature there exists a large number of studies focusing on spherical particle suspensions in wall-bounded turbulent flows (Kulick et al., 1994; Marchioli et al., 2007; Marchioli and Soldati, 2002; Maxey and Riley, 1983; Mortensen et al., 2007; Nilsen et al., 2013; Rouson and Eaton, 2001). Non-spherical particles suspended in fluid turbulence have received considerably less attention compared to suspensions of spherical particles. In the majority of applications, the non-spherical particle can be closely approximated by a regularly-shaped

---

* Corresponding author.
E-mail address: lihao.zhao@ntnu.no (L. Zhao).

http://dx.doi.org/10.1016/j.ces.2016.07.002
0009-2509/

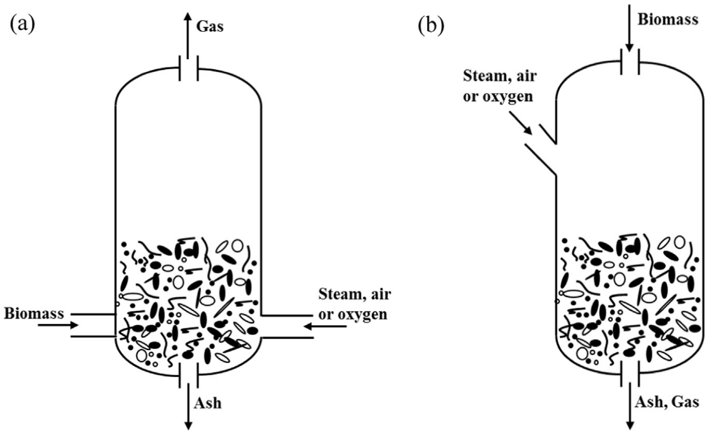

Fig. 1. Two qualitatively different types of entrained flow gasifiers: (a) side feed reactor, and (b) top feed reactor (adapted from Basu (2010)).

axi-symmetric particle, notably a spheroidal particle which is characterized by its shape and inertia quantified by the aspect ratio λ and the response time τ_p, respectively. Following the seminal mathematical analysis by Jeffery (1922) for an ellipsoidal particle suspended in a creeping flow, several researchers (Brenner, 1963, 1964; Gallily and Cohen, 1979; Harper and Chang, 1968) have contributed to the advancement of the theory related to the translational and rotational motion of spheroidal particles in shear flows. In all these studies Stokes-flow conditions were assumed around the particle and both the effects of fluid and particle inertia were thus neglected. Lin et al. (2003) summarized the work related to the dynamics of non-spherical particles in laminar shear flows. In the absence of fluid inertia, particle inertia results in a drift towards tumbling of rods with modest inertia (Lundell and Carlsson, 2010; Subramanian and Koch, 2006) whereas spinning is observed for heavy rods (Lundell and Carlsson, 2010; Nilsen and Andersson, 2013). Computer simulations using a lattice Boltzmann method were used to identify different rotational states of a spheroidal particle as a function of the particle Reynolds number $Re_p = Gd^2\nu^{-1}$ based on the equatorial diameter d and the shear rate G (Huang et al., 2012; Qi and Luo, 2003; Rosén et al., 2014; Yu et al., 2007). Recently Rosén et al. (2015) reported the different rotational states observed for a prolate spheroidal particle due to the combined effects of fluid and particle inertia.

The dynamics of non-spherical particles in turbulent flows is exceedingly more complex than in laminar shear flows. The prevailing approach has been to consider the motion of spherical particles and how they concentrate themselves in the turbulent environment. Recently there is an increased focus on the understanding of the behavior of non-spherical particles in turbulent flows. The dynamics of non-spherical particles in homogeneous isotropic turbulence have been explored in experimental investigations (Bellani et al., 2012; Ni et al., 2015; Parsa et al., 2011) and computational studies (Byron et al., 2015; Fan and Ahmadi, 1995; Gustavsson et al., 2014; Marcus et al., 2014; Ni et al., 2014; Olson, 2001; Parsa et al., 2012; Shin and Koch, 2005).

Experimental studies on non-spherical particles in wall-bounded turbulent flows are scarce (Abbasi Hoseini et al., 2015). Yin et al. (2003) and Zastawny et al. (2012) developed a methodology for modeling the dynamics of non-spherical particle-laden flows by assuming shape and orientation dependent drag and lift-force correlations. Later this methodology has been adopted by Njobuenwu and Fairweather (2014, 2015) to investigate the influence of a wide range of particle shapes and inertia on the translational and rotational behavior of ellipsoidal particles in wall-bounded turbulent flows. More accurate direct numerical simulations (DNSs) of the turbulent flow field coupled with a Lagrangian point-particle tracking methodology were successfully employed by some different research groups to investigate the dynamics of non-spherical inertial particles in wall-bounded turbulent flows. Zhang et al. (2001), and later followed by several others (Challabotla et al., 2015; Marchioli et al., 2010; Mortensen et al., 2008a, b; Zhao and van Wachem, 2013; Zhao et al., 2015) focused on the orientation, transport, and deposition of fibers suspended in a turbulent channel flow over a wide range of particle parameters (aspect ratio λ and inertia τ_p). The fiber inertia resulted in accumulation of fibers in the near-wall region and preferential concentration in the low-speed streaks which characterize wall turbulence. The fibers in the near-wall region moreover tended to preferentially orient themselves in the streamwise direction and this tendency increased with aspect ratio. A first attempt towards fully-resolved simulations of finite-size rod-like particles suspended in a turbulent channel by means of a lattice Boltzmann approach was recently reported by Do-Quang et al. (2014).

The role of gravity is believed to be of practical importance in fiber-suspended turbulent flows. In all industrial applications and experimental studies gravity is inevitably present, but in most of the abovementioned computational investigations the gravity force has been neglected. For example in bio-mass combustion reactors, as depicted in Fig. 1, the injection of biomass fibers either from the top or the bottom might have significant effect on the influence of the combustion efficiency. In order to optimize the reactor design, it is essential to better understand the fiber dynamics in different gravity configurations. Only a few systematic investigations have been carried out with the view to understand the effect of gravity on the dynamics of particle-laden turbulent flows. Gravity effects on spherical particle dispersion and deposition via the crossing trajectory mechanism in a vertical pipe flow were reported by Uijttewaal and Oliemans (1996). A comprehensive and systematic study of gravity and lift force effects on spherical particle velocity and deposition statistics in a turbulent vertical channel flow were reported by Marchioli et al. (2007). Recently, Nilsen et al. (2013) showed that gravity has a significant influence on the slip velocity of inertial spheres. The statistics deduced for the heaviest spherical particles were strongly dependent on the actual gravity configuration. Zhang et al. (2001) studied transport and deposition of ellipsoidal particles in a turbulent channel flow and observed strong effects of gravity at low shearing velocities. Preliminary results from large-eddy simulations (LESs) of a vertical channel flow suspended with needle-like and disk-like particles were very recently presented by Njobuenwu and Fairweather (2014). With the view to accurately predict the particle deposition rate they included a stochastic term to represent Brownian motion and a dispersion term to account for the sub-grid-scale motions of the unresolved turbulence. The orientation and settling velocity statistics over a wide range of ellipsoidal particles in decaying isotropic turbulence were reported by Siewert et al. (2014).

The computational investigations of inertial fiber-like particles embedded in a turbulent channel flow showed distinct preferential concentrations and preferential orientations of the elongated particles which depended on fiber inertia and fiber shape and varied from the wall regions to the core of the channel. However, the presence of gravity was systematically neglected although a gravity force is likely to de-correlate the fiber from the local fluid velocity and either accelerate or decelerate the inertial fibers depending on whether the bulk flow is up or down, i.e. against or along the gravity direction. The present investigation is an extension of the earlier studies by Mortensen et al. (2008a, 2008b) and Zhao et al. (2014) in which the gravity force was neglected. We now include gravity and buoyancy in the fibers' equation of motion in order to perform a systematic study of gravity effects on the fiber orientations, fiber velocities, and slip velocities. The fibers will be characterized both by shape and inertia. Some sample results were presented by Challabotla et al. (2016). Now further results from simulations of upward flow and downward flow in a vertical channel will be compared with results from channel flow simulations in which gravity is neglected. We thereby aim to address the obvious conjecture that inertial fibers are affected oppositely in upward and downward flow configurations.

2. Methodology

The dynamics of rigid fibers suspended in a turbulent vertical channel flow is studied by adopting an Eulerian–Lagrangian approach. The viscous fluid is assumed to be incompressible, isothermal, and Newtonian. The fluid flow in which the rigid fibers are suspended is governed by continuity (mass conservation) and the Navier–Stokes equations,

$$\frac{\partial u_i}{\partial x_i} = 0 \tag{1}$$

$$\rho_f\left(\frac{\partial u_i}{\partial t} + u_j\frac{\partial u_i}{\partial x_j}\right) = -\frac{\partial p}{\partial x_i} + \mu\frac{\partial^2 u_i}{\partial x_j \partial x_j} + \underbrace{\left(-\frac{dP}{dx} \pm \rho_f g\right)}_{\tau_w/h}\delta_{x,i}. \tag{2}$$

In the above equations u_i is the component of the fluid velocity vector in the x_i-direction and p is the fluctuating pressure, while ρ_f and μ are the density and dynamic viscosity of the fluid, respectively. Here, the three coordinate directions $x_i = \langle x, y, z\rangle$ refer to the streamwise, spanwise, and wall-normal directions, as shown in Fig. 2. The last term in the momentum equation (2) represents the driving mean pressure gradient and the gravity force per volume unit. The mean pressure P is supposed to decrease in the streamwise x-direction so that the pressure gradient $dP/dx < 0$ drives the flow in the positive x-direction which is either upwards (GU) or downwards (GD) and corresponds to a negative or a positive gravity force $\rho_f g$, respectively. In both cases the two driving forces are balanced by the wall shear stress τ_w and h is half of the distance between the two parallel channel walls.

The rigid fibers suspended in the continuous fluid are modeled as prolate spheroidal point-particles with aspect ratio $\lambda = b/a > 1$ where a and b are the semi-minor and semi-major axes, respectively. The particular case $\lambda = 1$ represents spherical particles. The mathematical modeling of the spheroidal point-particles follows the methodology outlined by Zhang et al. (2001) and subsequently adopted by Mortensen et al. (2008a, 2008b) and Marchioli et al. (2010). The translational and rotational motions of one single fiber is governed by,

$$m_p\frac{dv_i}{dt} = F_i \tag{3}$$

$$I'_{ij}\frac{d\omega'_j}{dt} + \epsilon_{ijk}\omega'_j I'_{kl}\omega'_l = N'_i, \tag{4}$$

where m_p is the mass of the fiber and ϵ_{ijk} is the Levi-Civita alternating or permutation tensor. Two different Cartesian frames of reference are used. The translational motion of a fiber is governed by Newton's 2nd law of motion (3), which is expressed in the inertial frame $x_i = \langle x_1, x_2, x_3\rangle$ or $\langle x, y, z\rangle$ and the rotational motion is governed by Euler's Eq. (4), which is formulated in the fiber frame $x'_i = \langle x'_1, x'_2, x'_3\rangle$ with its origin at the fiber mass center and the coordinate axes aligned with the principal directions of inertia. Thus, $v_i = dx_i/dt$ denotes the translational fiber velocity in the inertial frame, whereas ω'_i is the angular velocity of the fiber in the particle frame and I'_{ij} is the moment of inertia tensor for the spheroidal fiber.

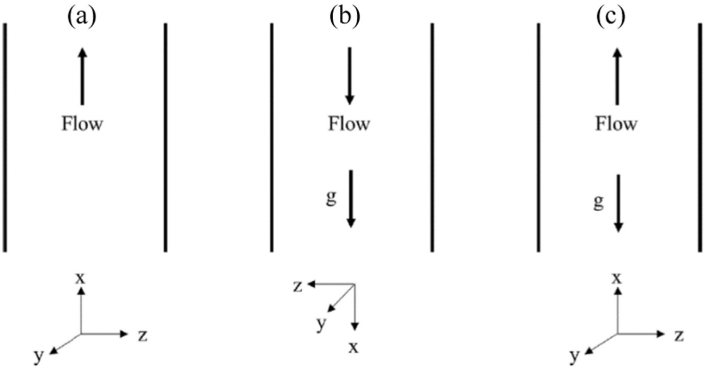

Fig. 2. Gravity configurations: (a) no-gravity flow G0, (b) downward flow GD, and (c) upward flow GU.

If the fibers are sufficiently small so that the neighboring flow can be considered as Stokesian, the force F_i acting on a fiber can be expressed as:

$$F_i = \pi\mu a K_{ij}\,\Delta u_j \pm \left(1-\frac{1}{D}\right) m_p g \delta_{x,i}\,, \tag{5}$$

where $\Delta u_j = u_j - v_j$ is the *slip velocity* defined as the difference between fluid velocity u_j at the fiber location and the fiber velocity v_j and $D=\rho_p/\rho_f$ is the ratio between the fiber and fluid densities. Here, the resistance tensor K_{ij} is represented in the inertial frame and related to the resistance tensor K'_{ij} in the fiber frame as $K_{ij}=A^t_{ik}K'_{kl}A_{lj}$ where A_{ij} denotes the orthogonal transformation matrix which relates the same vector in the two different frames through the linear transformation $x_i=A_{ij}\,x'_j$. The first term on the right-hand side of Eq. (5) represents the hydrodynamic drag force from the surrounding fluid acting on a non-spherical particle as derived by Brenner (1964). This expression for the drag force is valid only when the particle Reynolds number Re_p is low such that the force acting on the fiber is linearly dependent on the slip velocity Δu_j. The second term in Eq. (5) represents the gravity and buoyancy forces. Just as in equation (2), positive and negative gravity correspond to downwards (GD) and upwards (GU) flow, respectively.

Similarly as the drag force in the first part of Eq. (5), the torque N'_i in Eq. (4) is dependent on the relative angular velocity between the fluid and the fiber, but also on the fluid strain-rates, i.e.

$$\begin{aligned}
N'_1 &= \frac{16\pi\mu a^3\lambda}{3\left(\beta_0+\lambda^2\gamma_0\right)}\left[\left(1-\lambda^2\right)S'_{23}+\left(1+\lambda^2\right)\left(\Omega'_1-\omega'_1\right)\right]\\
N'_2 &= \frac{16\pi\mu a^3\lambda}{3\left(\alpha_0+\lambda^2\gamma_0\right)}\left[\left(\lambda^2-1\right)S'_{13}+\left(1+\lambda^2\right)\left(\Omega'_2-\omega'_2\right)\right]\\
N'_3 &= \frac{32\pi\mu a^3\lambda}{3\left(\alpha_0+\beta_0\right)}\left(\Omega'_3-\omega'_3\right).
\end{aligned} \tag{6}$$

The parameters α_0, β_0 and γ_0 depend on the fiber aspect ratio λ. Here, S'_{ij} and Ω'_i denote the fluid strain-rate tensor and rate-of-rotation vector, respectively. These expressions were first derived by Jeffery (1922) for an ellipsoidal particle in creeping flow.

The shape of a fiber is characterized by the aspect ratio λ, whereas the ability of the fiber to adjust to the ambient flow field can be estimated in terms of the fiber response time:

$$\tau_p = \frac{2Da^2\lambda\;\ln\left(\lambda+\sqrt{\lambda^2-1}\right)}{9\nu\sqrt{\lambda^2-1}};\quad St=\frac{\tau_p u_\tau^2}{\nu}, \tag{7}$$

where τ_p was defined by Shapiro and Goldenberg (1993) as a representative time scale of the translational motion of an ellipsoidal particle. The Stokes number St is the non-dimensionalized fiber response time based on the wall variables.

The flow is driven through a vertical plane channel by means of a constant force which comprises the mean pressure gradient dP/dx and gravity $\rho_f g$. The total driving force, i.e. the last term to the right in equation (2), is exactly balanced by the wall-shear stress τ_w. The frictional Reynolds number $Re_\tau = u_\tau h/\nu$ is defined in terms of the wall-friction velocity $u_\tau = \sqrt{\tau_w/\rho_f}$ and the kinematic fluid viscosity $\nu = \mu/\rho_f$.

The instantaneous turbulent flow field is obtained by integration of the governing Navier–Stokes equation (2) subjected to the incompressibility constraint (1). For $Re_\tau = 180$ direct numerical simulations are performed on a $12h \times 6h \times 2h$ computational domain with $192 \times 192 \times 192$ grid points in the streamwise (x), spanwise (y), and wall-normal (z) directions, respectively. In the wall-normal direction the grid is refined towards the channel walls such that Δz^+ varies between 0.9 and 2.86. The grid resolutions in the two homogeneous directions are uniform with $\Delta x^+ = 11.3$ and $\Delta y^+ = 5.6$. The time step used is $\Delta t^+ = 0.036$. Periodic boundary conditions are used in the homogeneous streamwise and spanwise directions and no-slip and impermeability conditions are imposed at the channel walls. The DNS solver used is same as that employed by Gillissen et al. (2007) and Mortensen et al. (2008a, 2008b).

Along with the integration of the flow field Eqs. (1) and (2), the equations for the translational (3) and rotational (4) motion of the fibers are integrated in time with an explicit second-order accurate Adams-Bashforth scheme. The time step used during the integration of the fiber equations is the same as that used for the Navier–Stokes equations. The time rate-of-change of the four Euler parameters is obtained from the three components of the fiber angular velocity ω'_i. After re-normalization, the new values of the Euler parameters completely specify the fiber orientation, i.e. the angle θ_i between the symmetry axis of a fiber and the x_i-axis of the inertial reference frame in which the fluid flow problem is formulated (Eqs. (1) and (2)) and solved (Mortensen et al., 2008a). Spatial derivatives in the two homogeneous directions are computed with a pseudo-spectral method and in the wall-normal direction the derivatives are computed by a second-order central finite-difference method. The flow variables at a fiber location are interpolated by means of a second-order quadratic interpolation scheme. The particle boundary conditions are periodic in the two homogeneous directions. Fiber-wall collisions are fully elastic, similar to the collision model used by Marchioli et al. (2010) and Zhao et al. (2014). This implies that a fiber keeps its linear and angular momentum in the homogeneous directions upon touching the wall. A collision is defined to occur every time that the distance from the center of mass of a fiber to the closest wall becomes less than the semi-minor axis a. The present pragmatic model gives probably an unrealistic representation of the orientation and rotation states after a wall collision; see e.g. (Ozolins and Strautins, 2014; Zhao and van Wachem, 2013). An alternative collision detection rule, for instance based on the impact of one tip of the fiber with the wall, might yield quantitative differences for high-aspect-ratio fibers.

In the present work it is assumed that the fiber suspension is sufficiently dilute so that the one-way coupled Eulerian–Lagrangian approach can be justified, i.e. although the fiber motion is affected by the fluid motion, the feedback from the fibers onto the fluid is negligible. Moreover, particle-particle collisions are rare and can also be neglected. In real situations, however, the flow might be modulated by the presence of inertial particles in areas with high particle concentrations. Attenuation or augmentation of fluid turbulence depends on several factors, such as the density ratio, the local volume fraction, and the particle size; see e.g. Balachandar and Eaton (2010). The modulated turbulence field may in turn affect the particle transport mechanisms, especially in the near-wall region where relatively high particle concentrations can be observed (Li et al., 2001; Zhao et al., 2013). However, the present study is concerned with the effect of gravity on the dynamics of inertial fibers in channel flow turbulence. We therefore neglect any potential effects of particle-fluid interactions and confine ourselves to one-way coupled simulations.

Simulations are performed for fiber Stokes numbers St = 1, 5, 30 and 100 and aspect ratios $\lambda = 1.001$, 3 and 10. The density ratio D is kept the same ($D = 1000$) for all the twelve different fiber classes, whereas the semi-minor axis is varied, as shown in Table 1. The mathematical expressions for the resistance tensor K_{ij} in Eq. (5) and the shape parameters α_0, β_0 and γ_0 in Eq. (6) exhibit singularities for $\lambda = 1$; see e.g. (Zhao et al., 2014). Particles with aspect ratio $\lambda = 1.001$ are therefore considered as representatives of spherical particles. Detailed comparisons with earlier results for truly spherical particles, for instance those of Mortensen et al. (2007), demonstrate a perfect match with the present results for $\lambda = 1.001$.

Table 1
The twelve different fiber classes considered (density ratio $D=1000$). Prolate spheroids with aspect ratio $\lambda=1.001$ represent spherical particles. The particle Reynolds number is defined as $Re_p=D_{eq}\langle\Delta U_x\rangle/\nu$, where D_{eq} is the volume-equivalent fiber diameter.

Stokes number (*St*)	Aspect ratio (λ)	Semi minor axis (a^+)	Channel averaged Re_p			Maximum Re_p		
			GD	G0	GU	GD	G0	GU
1	1.001	0.067	0.0038	0.0018	0.0043	0.0118	0.0083	0.0049
	3	0.049	0.0082	0.0037	0.0091	0.0254	0.0174	0.0107
	10	0.039	0.0099	0.0044	0.0110	0.0324	0.0220	0.0131
5	1.001	0.150	0.0162	0.0078	0.0213	0.0465	0.0291	0.0281
	3	0.110	0.0410	0.0172	0.0456	0.1267	0.0735	0.0622
	10	0.086	0.0514	0.0206	0.0558	0.1682	0.0945	0.1400
30	1.001	0.367	0.1002	0.0257	0.1303	0.1661	0.0501	0.1568
	3	0.269	0.2547	0.0510	0.2879	0.5467	0.2011	0.3581
	10	0.212	0.3126	0.0604	0.3362	0.7378	0.2391	0.4203
100	1.001	0.671	3.4228	0.6460	4.0427	5.2272	1.7165	4.6201
	3	0.491	7.5210	1.3853	8.5917	14.0750	4.5420	9.9174
	10	0.387	8.6628	1.6558	10.008	15.8340	5.5584	11.6150

Following the work by Marchioli et al. (2007) for spherical particles, the three different gravity configurations depicted in Fig. 2 are considered for each of the twelve fiber classes: no gravity (G0), downward flow (GD), and upward flow (GU). This amounts to a total of 3x12 different cases. In each case 200,000 fibers are tracked in the same turbulence field. Fiber statistics are computed by averaging instantaneous data in time from $t^+=5400$ to 10,800 and also in the homogeneous streamwise and spanwise directions. In order to obtain reliable particle statistics, the present simulations were run longer than in earlier studies of fiber suspension flows to enable statistics to be gathered over 5400 viscous time units. This time window compares favorably with the sampling times used by others, e.g. 450 (Marchioli et al., 2007), 2880 (Mortensen et al., 2008a), and 1200 (Marchioli et al., 2010).

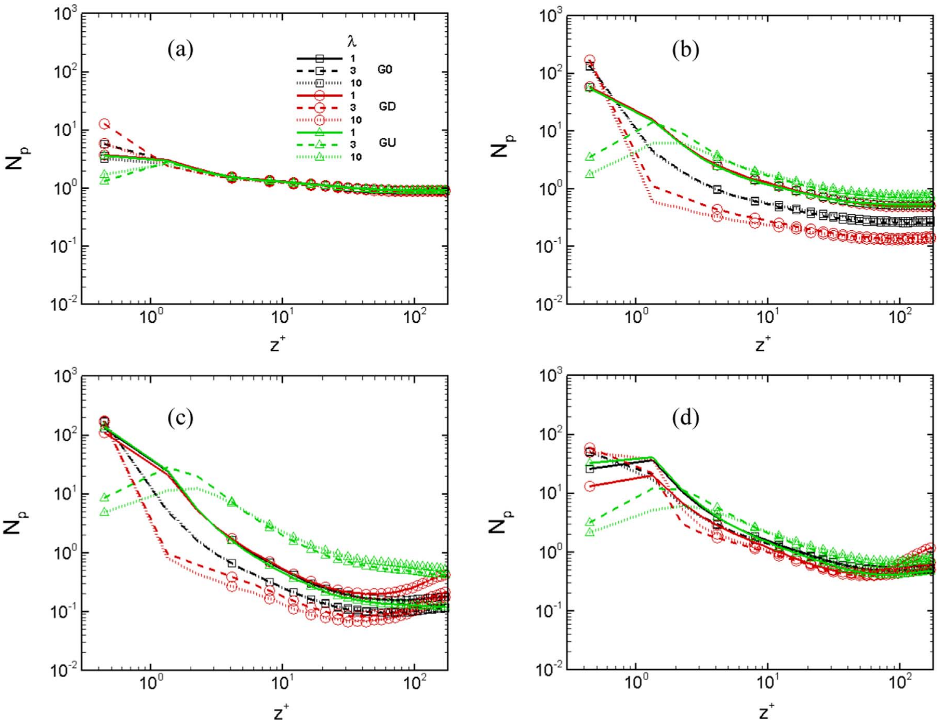

Fig. 3. Statistically averaged particle number density distribution for (a) St=1, (b) St=5, (c) St=30 and (d) St=100. G0: no-gravity flow; GD: downward flow; and GU: upward flow.

3. Results and discussion

The main objective of this work is to present and discuss the effects of gravity on the concentration, velocity and orientation statistics of the rigid fibers suspended in upward (GU) and downward (GD) vertical channel flow. The case without gravity (G0) will serve as a reference. For the particular density ratio $D=1000$, the buoyancy force in Eq. (5) plays a negligible role compared with the gravity force.

To better understand the gravity effects on the dynamics of the fibers suspended in the turbulent channel flow, we first consider the variation of averaged fiber number density $\mathrm{N_p}$ as function of the distance z^+ to the wall, as shown in Fig. 3. Fiber number density profiles are computed at different stages of the simulation by adopting a bin size similar to that of the grid spacing Δz in wall-normal direction (i.e. 192 bins) and by counting the number of fibers in each bin all over the (x, y)-plane. The fiber number density is normalized by the initial fiber number density. The four panels shown in Fig. 3 are for increasing Stokes number St from 1 to 100, and each panel shows the effect of fiber elongation λ for the three different gravity configurations. For the special case of spherical particles ($\lambda=1$), the gravity effects are significant only for particles with $St \geq 30$. In the downflow configuration (GD) an increased particle concentration is observed in the central region of the channel when compared to that in the upflow configuration (GU) and in absence of gravity (G0). This observation for spherical particles is consistent with previous results reported by Marchioli et al. (2007) and Nilsen et al. (2013). It should be noted that the concentration of the more inertial fibers ($St \geq 5$) has not yet reached a steady state, similarly as for spherical particles studied by Marchioli et al. (2008).

In the absence of gravity, inertial fibers are drifting with relatively high streamwise momentum from the center region of the channel towards the wall region and accumulate in low-speed streaks in the wall vicinity (Marchioli et al., 2010; Zhao et al., 2014). This phenomenon results in an excess fiber concentration in the near-wall region. The presence of gravity has apparently no influence on the least inertial fibers (St=1) and all the concentration distributions in Fig. 3(a) overlap except in the immediate vicinity of the wall. One can observe, however, that the flow direction relative to the gravity has a significant effect on the fiber number density distribution for $St \geq 5$ and the effect is remarkably stronger for fibers ($\lambda \geq 3$) than for spheres ($\lambda=1$). Indeed, the particle number density for spheres with St=5 in Fig. 3 (b) is totally unaffected by gravity whereas the $\mathrm{N_p}$–distributions for fibers are not. It is also noteworthy that the fibers are more evenly distributed in the upward flow than in the absence of gravity, whereas a high fiber concentration is observed next to the wall in the downflow case. For the most inertial fibers (St=100), on the other hand, the effect of gravity is reduced and so is the differences between the elongated fibers and spheres. The trends observed for fibers in the presence of gravity are different from the observation for spherical particles reported by Marchioli et al. (2007) and Nilsen et al. (2013). The differences in the fiber number density (N_p) distributions in the different flow configurations are believed to affect other fiber statistics such as the fiber mean and fluctuating velocity components and the fiber orientations. Such alterations will be considered in the following.

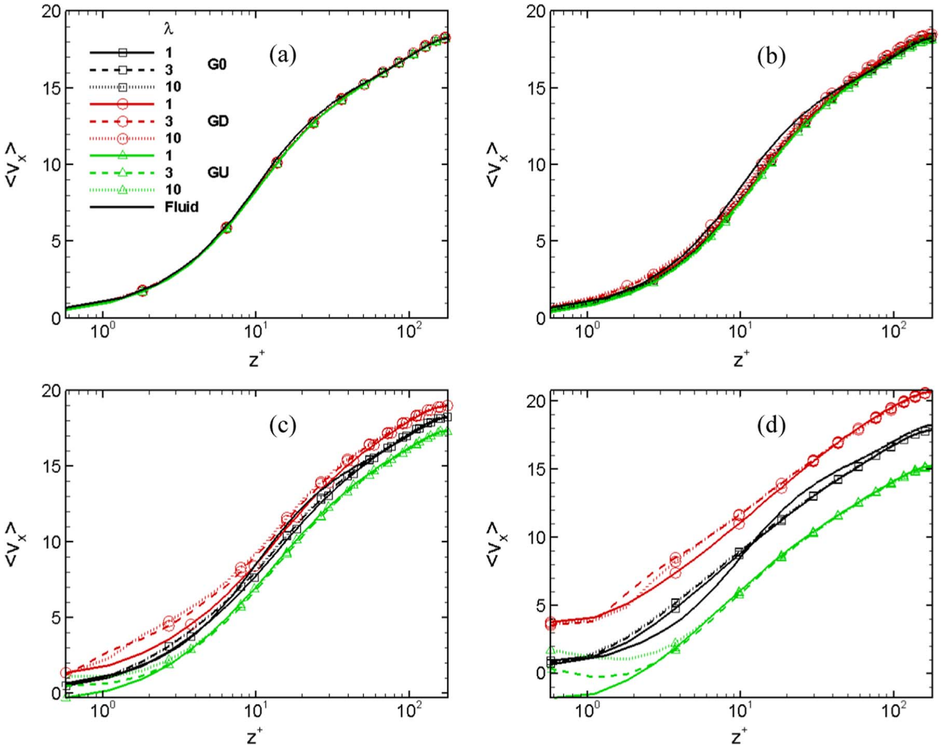

Fig. 4. Mean fiber $\langle v_x \rangle$ and local fluid $\langle u_x \rangle$ streamwise velocities for (a) St=1, (b) St=5, (c) St=30 and (d) St=100. G0: no-gravity flow; GD: downward flow; and GU: upward flow.

The variation of the mean streamwise fiber velocity $\langle v_x \rangle$ from the wall to the center of the channel is shown as a function of the wall-normal coordinate z^+ in the semi-logarithmic plots in Fig. 4. Here, and in the following, all velocities are normalized with the fluid frictional velocity u_τ. The results for fibers without gravity (G0) show an almost negligible effect of the aspect ratio and are in close agreement with the results reported by Mortensen et al. (2008a) and Marchioli et al. (2010). For Stokes number $St=1$, the mean fiber velocities are also practically unaffected by the presence of gravity, irrespective of whether the bulk flow is upwards (GU) or downwards (GD). With increasing inertia, however, the influence of the gravity force becomes gradually more important. The inertial fibers clearly lead the fluid (solid line) in the downflow case and lag behind the fluid in the upward flow. This is primarily due to the increase of the *settling velocity* of a fiber in a fluid at rest with increasing fiber inertia. The fiber velocity next to the wall is always downwards, i.e. positive for downflow and negative for upflow. Similar trends were reported for spherical particles by Marchioli et al. (2007). These results suggest that the presence of a gravity force strongly de-correlates the fiber velocity from the fluid velocity for inertial fibers with St=30 and 100. The effect of fiber elongation on the mean velocity distributions is practically negligible, except for the fibers in the viscous sublayer $z^+ \leq 10$.

The mean wall-normal velocity $\langle v_z \rangle$ of the fibers, the so-called *drift velocity*, plays an important role in the fiber transfer mechanisms towards and away from the channel walls. Fig. 5 shows profiles of the mean fiber wall-normal velocity, $\langle v_z \rangle$, as a function of the wall-normal coordinate, z^+. In absence of gravity, a modest drift velocity can be observed and this drift velocity increases with increasing fiber inertia and reaches a maximum for Stokes number St = 30. The presence of gravity is seen to have only a modest influence on the drift velocity for spherical particles, whereas remarkably strong effects are observed for the elongated particles ($\lambda > 1$). Fibers in the downflow configuration experience a substantially larger drift velocity than the spheres and this phenomenon is most clearly pronounced for St=30 where $\langle v_z \rangle \approx 0.07$. In the upward flow configuration, on the contrary, the drift velocity of the fibers are essentially zero, in contrast with the negative $\langle v_z \rangle$ observed for spherical particles. The negligible drift velocity of the fibers in the upflow configuration GU suggests that these fibers have reached an almost statistically steady state of the fiber number density N_p shown in Fig. 3. Fibers in the downflow configuration (GD), however, have a higher drift velocity towards the channel walls which reflects an increased transport of fibers from the core region and eventually a higher fiber number density in the near-wall region, as shown in Fig. 3. Although the fiber concentration distributions in Fig. 3 are still in a transient stage, the qualitative trends observed with respect to the effects of gravity, inertia and shape are trustworthy. Irrespective of the ultimate fiber distributions, however, the magnitudes of the observed drift velocities in Fig. 5 are believed to decay asymptotically to zero if the simulations were allowed to run even further.

Let us now proceed and look at the difference between the fluid and the fiber velocities, i.e. the slip velocity $\Delta u_i = u_i - v_i$ studied for instance by Mortensen et al. (2008a) and Zhao et al. (2014). The mean velocity slip in the streamwise and wall-normal directions are shown in Figs. 6 and 7, respectively. The mean spanwise slip $\langle \Delta u_y \rangle$ should be zero and this has been used to check (not shown) that the sampling time used in the present study is sufficient to produce reliable statistics. The streamwise mean slip

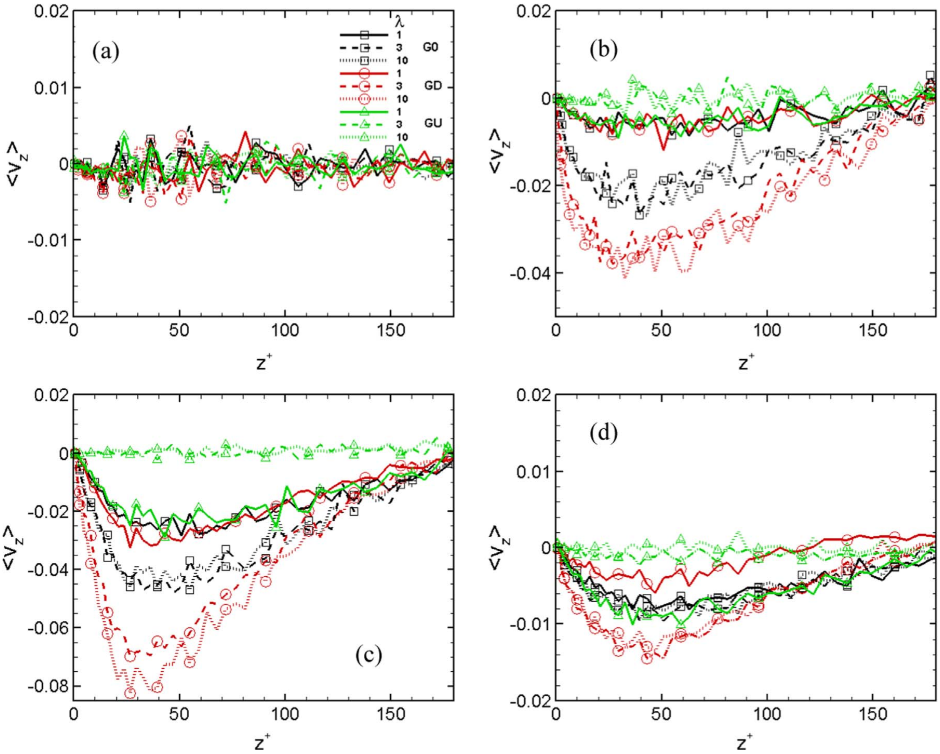

Fig. 5. Mean fiber wall-normal velocities $\langle v_z \rangle$ for (a) St=1, (b) St=5, (c) St=30 and (d) St=100. G0: no-gravity flow; GD: downward flow; and GU: upward flow.

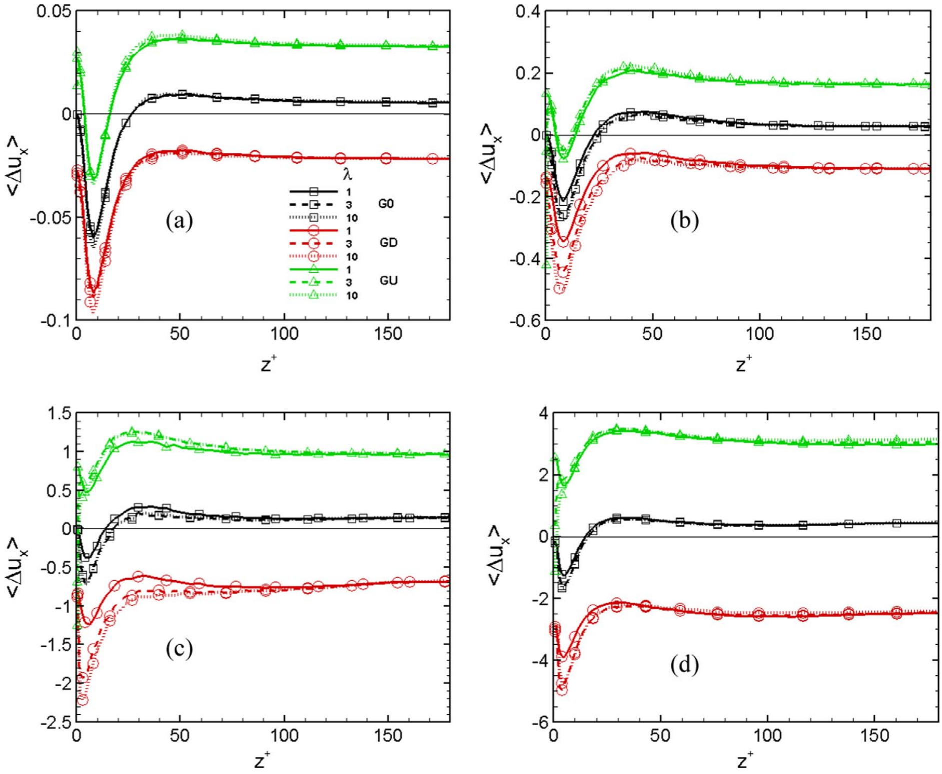

Fig. 6. Mean streamwise slip velocity $\langle \Delta u_x \rangle$ for (a) St=1, (b) St=5, (c) St=30 and (d) St=100. G0: no-gravity flow; GD: downward flow; and GU: upward flow.

$\langle \Delta u_x \rangle$ in Fig. 6 is negative in the near-wall region and slightly positive in the rest of the channel in absence of gravity. This shows that the fibers lead the fluid near the wall and lag behind the fluid in the core region. This effect increases with increasing inertia (St), but is almost independent of shape (λ), similarly as already reported by Mortensen et al. (2008a) and Zhao et al. (2014).

In the downflow configuration (GD), however, the mean streamwise slip velocity $\langle \Delta u_x \rangle$ is negative throughout the entire channel, irrespective of fiber inertia (St) and shape (λ). This is a direct consequence of the settling velocity of the fibers which implies that the fibers everywhere lead the fluid and thus experience a negative viscous drag force which opposes the gravity force in Eq. (5). In the upflow configuration (GU), negative drag persists only in the near-wall region when $\langle \Delta u_x \rangle$ remains negative for low Stokes numbers and thus adds to the gravity effect. For St=30 and above, the mean slip is consistently positive even in the wall vicinity. The viscous fluid therefore tends to drag the fibers along in the positive upward direction and the Stokes drag thereby opposes the gravity force. It is remarkable that the results in Fig. 6 are essentially independent of the aspect ratio. A shape effect can be seen for $z^+ < 100$. The modest shape-dependence is most pronounced in downward flow where fibers ($\lambda > 1$) experience a larger negative slip $\langle \Delta u_x \rangle$ than spheres ($\lambda = 1$).

We have observed a larger slip velocity in presence of gravity. Nevertheless, the particle Reynolds number Re_p is consistently lower than unity, except for the most inertial fibers (see Table 1). The Stokes flow approximation, on which the expressions for the viscous force in Eq. (5) and the torques in Eq. (6) are based, is therefore a reasonable assumption, except for St=100. These latter results can, however, be considered as qualitatively correct and are included here to provide the trends of the effects caused by the different parameters.

The mean slip velocity in the wall-normal direction in Fig. 7 shows no discernible shape dependence in absence of gravity. However, spherical particles exhibit a major non-monotonic dependence on inertia, which reproduces the trend reported by Zhao et al. (2012) when gravity is ignored. Thus, the largest slip velocity is found for St=30 at $z^+ \approx 20$. Spheres as well as fibers with modest inertia in Fig. 7(a, b) are furthermore unaffected by the flow direction. The mean slip velocity $\langle \Delta u_z \rangle$ is negative in the center region of channel which indicates that the fibers are driven by the Stokes drag force towards the wall by sweeping events. In the near-wall region, the positive slip velocity suggests that ejection events are dominating the fiber transport towards the channel center.

As fiber inertia is further increased to St=30 and 100 the gravity starts to play an important role for the mean slip velocity, as shown in Fig. 7(c, d). Whether the bulk flow is upwards or downwards has a major influence on the mean slip velocity $\langle \Delta u_z \rangle$ in the horizontal direction for fibers as well as for spheres. We learned from Fig. 6 that the fibers in the downflow configuration experienced a negative slip velocity which gave rise to upward drag. The positive $\langle \Delta u_z \rangle$ in Fig. 7(c, d) can arise from three different reasons: (1) $v_z < u_z < 0$; (2) $u_z > 0$ and $v_z < 0$; (3) $u_z > v_z > 0$. By revisiting Fig. 5, we recall that the fibers in the central region are moving faster towards the wall than the local fluid by means of sweeps; i.e. case (1). The second combination (2) arises in the near-wall region where the fiber velocity is negative but the fluid

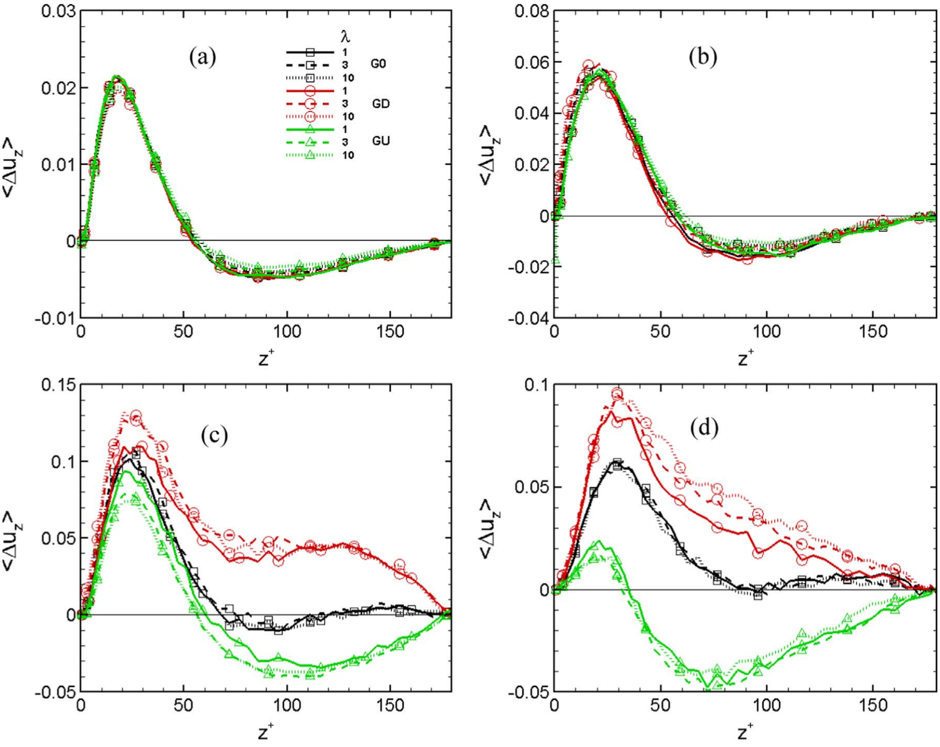

Fig. 7. Mean fiber wall-normal slip velocity $\langle \Delta u_z \rangle$ for (a) St=1, (b) St=5, (c) St=30 and (d) St=100. G0: no-gravity flow; GD: downward flow; and GU: upward flow.

velocity is positive when fluid is ejected away from the wall. If the three different gravity configurations are compared, we observe that the largest slip velocity $\langle \Delta u_z \rangle$ occurs in the downward flow whereas lowest slip velocity is found in upward flow. The particle shape affects the findings only in the downflow configuration such that an increasing aspect ratio λ tends to accentuate the gravity effect.

Based on these findings, together with the results in Figs. 3 and 5, we hypothesize that the presence of gravity affects the *turbophoresis*, i.e. the tendency of inertial particles to move towards regions of lower turbulence intensity (see e.g. Marchioli and Soldati (2002) and references therein). In the case of downward flow, the turbophoresis is augmented so that particle concentration maxima appear both in the channel center and next to the walls. On the other hand, gravity attenuates the turbophoresis effect in the upward flow, which in turn leads to a more even fiber distribution across the channel. This subtle effect of gravity is distinctly different for spheres ($\lambda = 1$) and fibers ($\lambda > 1$).

The fiber-laden vertical channel flow is turbulent and the fiber velocities are therefore fluctuating about their mean values similarly as the fluid velocities. Root-mean-square (rms) values of the streamwise and wall-normal fiber velocity components are shown in Figs. 8 and 9, respectively, for modest (left) and high (right) inertia. For St=5, the present results are almost indistinguishable

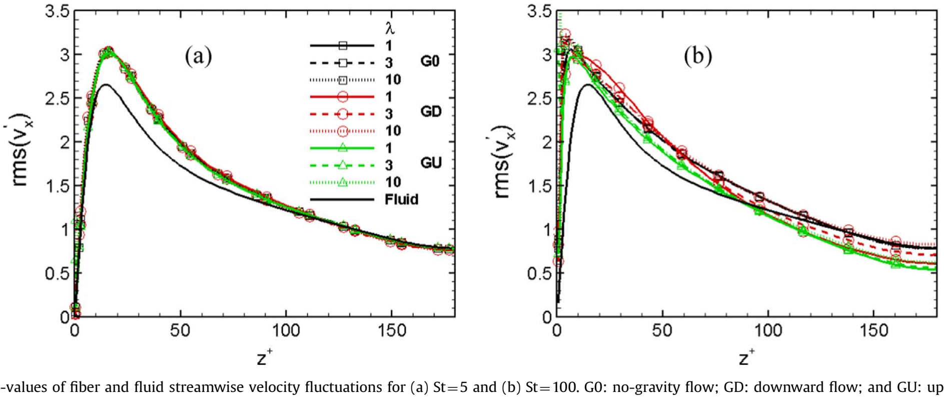

Fig. 8. rms-values of fiber and fluid streamwise velocity fluctuations for (a) St=5 and (b) St=100. G0: no-gravity flow; GD: downward flow; and GU: upward flow.

from the results reported by Mortensen et al. (2008a). The particle rms velocities exceed the corresponding fluid velocity fluctuations in the streamwise direction in Figs. 8(a), whereas rms $(v'_z) <$ rms (u'_z) all the way from the channel walls to the center in Fig. 9(a). The influence of the fiber aspect ratio on the particle intensities is negligible at this Stokes number, also in accordance with the earlier results of Mortensen et al. (2008a). Moreover, the rms-profiles for the three different flow configurations are also overlapping. This implies that also gravity, together with the shape parameter λ, has negligible effects on the fiber velocity fluctuations.

The more inertial fibers with St = 100 behave rather differently, except the streamwise fluctuations in absence of gravity in Fig. 8(b) which exceed the fluid fluctuations in the near-wall region and approach rms (u'_x) in the center. The wall-normal fluctuations in Fig. 9(b) are substantially reduced in comparison with the corresponding fluid velocity fluctuations. These results appear to be independent of the fiber aspect ratio λ and the remarkable reduction of the fiber velocity fluctuations from St = 5 to St = 100 can only be ascribed to fiber inertia.

The presence of gravity affects the velocity fluctuations of the St = 100 fibers such that the streamwise fluctuations are higher in the downflow than in the upflow configuration. Irrespective of flow direction, however, the wall-normal velocity fluctuations are damped compared with the case in which gravity is neglected and the amount of damping depends on aspect ratio.

Let us finally look at how the mean absolute direction cosines depend on fiber shape and gravity. Here, fiber orientation is measured as $\langle|\cos(\theta_i)|\rangle$, referred to as direction cosine hereinafter, and defined in terms of the angle θ_i between the symmetry axis of a fiber and the x_i-axis of the inertial frame. Fig. 10 shows results for fibers with modest inertia to the left and for strong inertia to the right. The former are in close agreement with the results shown by Mortensen et al. (2008a) and Marchioli et al. (2010) also for St = 5 and show the same dependence on the aspect ratio, namely that the elongated fibers tend to align in the streamwise direction ($|\cos(\theta_x)| > 0.5$) in the wall region. Also the recent experiments in a water table flow by Abbasi Hoseini et al. (2015) showed that fibers at $z^+ \approx 14$ oriented themselves in the streamwise direction. Mortensen et al. (2008a) conjectured that the excess streamwise fluid velocity fluctuations in the vicinity of the walls contributed to the preferential streamwise orientation by aligning the fibers in the x-direction. This may also explain the present observation that the orientation of the St = 5 fibers are unaffected by gravity. However, the preferential fiber orientation in the near-wall region ceases in the center of the channel where $|\cos(\theta_x)| \approx |\cos(\theta_y)| \approx |\cos(\theta_z)| \approx 0.5$ in Fig. 10 and reflects a random orientation of the fibers. Here, at $z^+ \sim 180$, the turbulent velocity field is undoubtedly anisotropic. However, the vorticity field is nearly isotropic, as shown by Andersson et al. (2015). We therefore believe that the isotropic fiber orientation is a direct implication of the almost isotropic fluid vorticity.

The very inertial fibers are probably more resistant to turbulent velocity fluctuations and the results for St = 100 to the right in Fig. 10 show a reduced preference for streamwise orientation near the wall. While the alteration of the preferred orientation appears to be an effect of inertia, the orientation of the inertial fibers in the channel center is also affected by gravity. It is noteworthy that these fibers remain almost randomly orientated (as for St = 5) in absence of gravity, whereas a distinct preference for streamwise orientation with $\langle|\cos\theta_x|\rangle$ well above 0.5 are found both in the upflow and downflow configurations. This finding in the almost isotropic core region is consistent with the recent observation by Siewert et al. (2014) that fibers in decaying isotropic turbulence tend to align preferentially in the vertical direction, i.e. aligned with the gravitational acceleration.

4. Concluding remarks

Computer simulations have been performed to explore fiber dynamics in wall-turbulence in presence of the gravity force. The present study therefore represents an extension of the earlier work by Mortensen et al. (2008a, 2008b) and Marchioli et al. (2010) in which gravity was ignored and only fiber inertia and shape were considered. Our results generally show that gravity has a negligible effect on fiber orientation and velocity statistics for fibers with modest inertia, i.e. low Stokes numbers. At higher Stokes numbers, however, gravity turns out to have a major impact on the fiber dynamics. In the downward channel flow, the drift velocity of the fibers towards the walls was substantially higher for fibers than for spheres and also higher than when gravity was neglected. In the upward flow configuration, on the other hand, the modest drift velocity of inertial spheres was totally quenched for all fibers irrespective of shape. The suppressed drift velocity in the upward flow resulted in a more uniform fiber distribution throughout the channel as compared to the distinct near-wall accumulation in downward flow and in absence of gravity.

Inertial fibers have been known to orientate isotropically in the almost isotropic vorticity field in the channel center in absence of gravity. However, we observed a preferential alignment with the gravity force in the vertical channel and irrespective of the bulk flow direction. The conjecture that inertial fibers are affected oppositely in upward and downward flow configuration has therefore been disproved.

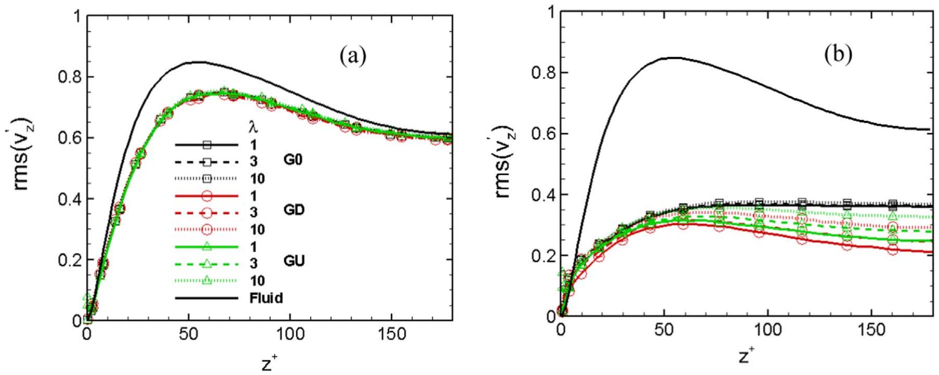

Fig. 9. rms-values of fiber and fluid wall-normal velocity fluctuations for (a) St = 5 and (b) St = 100. G0: no-gravity flow; GD: downward flow; and GU: upward flow.

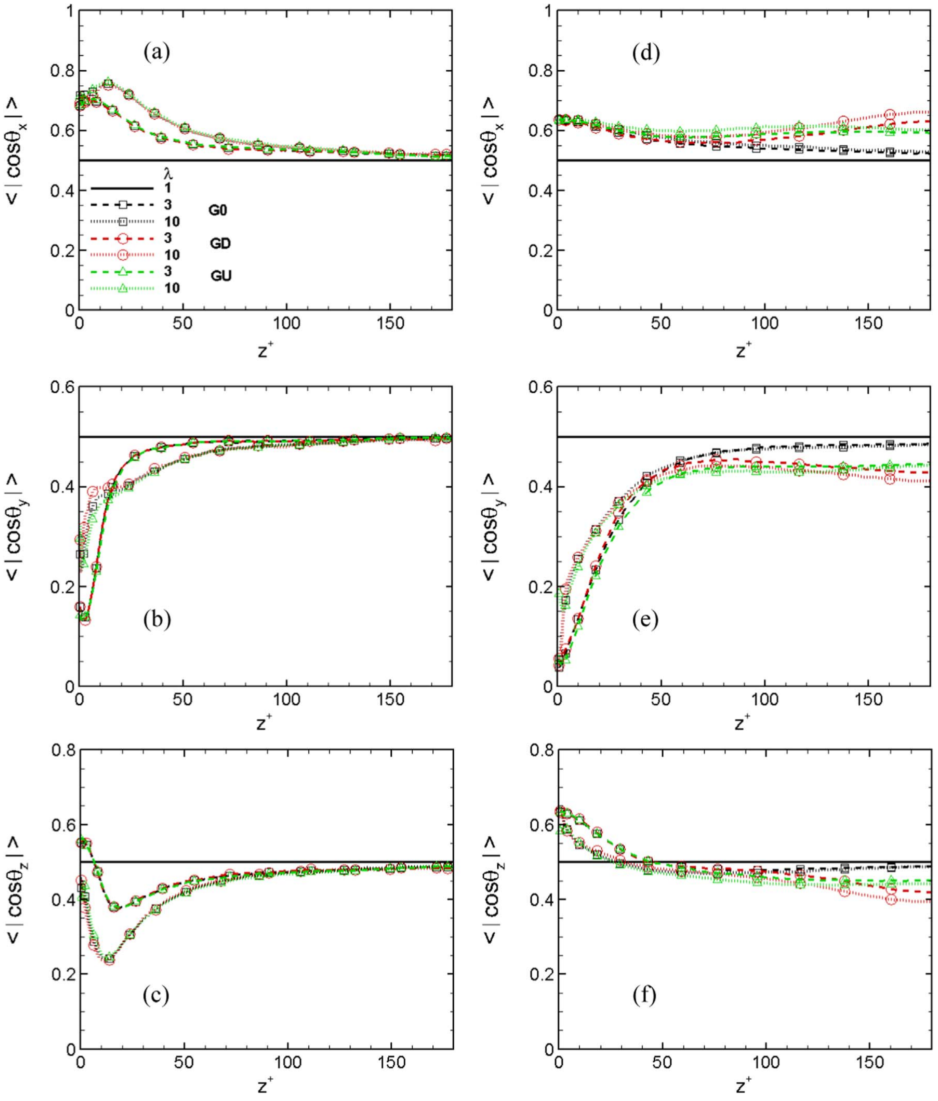

Fig. 10. Absolute direction cosines of the fibers relative to (a, d) streamwise direction; (b, e) spanwise direction; (c, f) wall-normal direction for (a–c) St = 5 and (d–f) St = 100. G0: no-gravity flow; GD: downward flow; and GU: upward flow.

We have learned that the gravity force in Eq. (5) plays a subtle role on the dynamics of inertial fibers in wall-bounded turbulent flows. The present findings strongly suggest that the actual gravity configuration might play an important role in the optimization of industrial processes. If a uniform fiber distribution is desired, as in a biomass combustion reactor (recall Fig. 1), an upward flow configuration should be the preferred choice. On the other hand, a downflow configuration should be attractive with the view to enhance aerosol deposition.

Acknowledgments

This study has been supported by the Research Council of Norway through a research fellowship to N.R.C. (project no 213917/F20 "Turbulent Particle Suspensions") and grants of computing time (Programme for Supercomputing).

References

Abbasi Hoseini, A., Lundell, F., Andersson, H.I., 2015. Finite-length effects on dynamical behavior of rod-like particles in wall-bounded turbulent flow. Int. J. Multiph. Flow. 76, 13–21.

Andersson, H.I., Zhao, L., Variano, E.A., 2015. On the anisotropic vorticity in turbulent channel flows. J. Fluids Eng. 137, 084503.

Balachandar, S., Eaton, J.K., 2010. Turbulent dispersed multiphase flow. Annu. Rev. Fluid Mech. 42, 111–133.

Basu, P., 2010. Chapter 5 - gasification theory and modeling of gasifiers. In: Basu, P. (Ed.), Biomass Gasification and Pyrolysis. BostonAcademic Press, pp. 117–165.

Bellani, G., Byron, M.L., Collignon, A.G., Meyer, C.R., Variano, E.A., 2012. Shape effects on turbulent modulation by large nearly neutrally buoyant particles. J. Fluid Mech. 712, 41–60.

Brenner, H., 1963. The Stokes resistance of an arbitrary particle. Chem. Eng. Sci. 18, 1–25.

Brenner, H., 1964. The Stokes resistance of an arbitrary particle—IV Arbitrary fields of flow. Chem. Eng. Sci. 19, 703–727.

Byron, M., Einarsson, J., Gustavsson, K., Voth, G., Mehlig, B., Variano, E., 2015. Shape-dependence of particle rotation in isotropic turbulence. Phys. Fluids 27, 035101.

Challabotla, N.R., Zhao, L., Andersson, H.I., 2015. Shape effects on dynamics of inertia-free spheroids in wall turbulence. Phys. Fluids 27, 061703.

Challabotla, N.R., Zhao, L., Andersson, H.I., 2016. Gravity effects on fiber dynamics in wall turbulence. Flow., Turbul. Combust., 1–16. http://dx.doi.org/10.1007/s10494-10016-19742-10495.

Do-Quang, M., Amberg, G., Brethouwer, G., Johansson, A.V., 2014. Simulation of finite-size fibers in turbulent channel flows. Phys. Rev. E 89, 013006.

Fan, F.-G., Ahmadi, G., 1995. Dispersion of ellipsoidal particles in an isotropic pseudo-turbulent flow field. J. Fluids Eng. 117, 154–161.

Gallily, I., Cohen, A.-H., 1979. On the orderly nature of the motion of nonspherical aerosol particles. II. Inertial collision between a spherical large droplet and an axially symmetrical elongated particle. J. Colloid Interface Sci. 68, 338–356.

Gillissen, J.J.J., Boersma, B.J., Mortensen, P.H., Andersson, H.I., 2007. On the performance of the moment approximation for the numerical computation of fiber stress in turbulent channel flow. Phys. Fluids 19, 035102.

Guasto, J.S., Rusconi, R., Stocker, R., 2012. Fluid mechanics of planktonic microorganisms. Annu. Rev. Fluid Mech. 44, 373–400.

Gustavsson, K., Einarsson, J., Mehlig, B., 2014. Tumbling of small axisymmetric particles in random and turbulent flows. Phys. Rev. Lett. 112, 014501.

Harper, E.Y., Chang, I.D., 1968. Maximum dissipation resulting from lift in a slow viscous shear flow. J. Fluid Mech. 33, 209–225.

Hilton, J.E., Cleary, P.W., 2011. The influence of particle shape on flow modes in pneumatic conveying. Chem. Eng. Sci. 66, 231–240.

Huang, H., Yang, X., Krafczyk, M., Lu, X.-Y., 2012. Rotation of spheroidal particles in Couette flows. J. Fluid Mech. 692, 369–394.

Jeffery, G.B., 1922. The Motion of Ellipsoidal Particles Immersed in a Viscous Fluid. In: Proceedings of the Royal Society of London. Series A 102, pp. 161–179.

Kleinstreuer, C., Feng, Y., 2013. Computational analysis of non-spherical particle transport and deposition in shear flow with application to lung aerosol dynamics—a review. J. Biomech. Eng. 135, 021008.

Kulick, J.D., Fessler, J.R., Eaton, J.K., 1994. Particle response and turbulence modification in fully developed channel flow. J. Fluid Mech. 277, 109–134.

Li, Y., McLaughlin, J.B., Kontomaris, K., Portela, L., 2001. Numerical simulation of particle-laden turbulent channel flow. Phys. Fluids 13, 2957–2967.

Lin, J., Shi, X., Yu, Z., 2003. The motion of fibers in an evolving mixing layer. Int. J. Multiph. Flow. 29, 1355–1372.

Loranger, E., Canonne, M., Daneault, C., Chabot, B., 2009. Effect of fibres on fluidized bed expansion parameters. Chem. Eng. J. 152, 530–536.

Lundell, F., Carlsson, A., 2010. Heavy ellipsoids in creeping shear flow: transitions of the particle rotation rate and orbit shape. Phys. Rev. E 81, 016323.

Lundell, F., Söderberg, L.D., Alfredsson, P.H., 2011. Fluid mechanics of papermaking. Annu. Rev. Fluid Mech. 43, 195–217.

Ma, L., Jones, J.M., Pourkashanian, M., Williams, A., 2007. Modelling the combustion of pulverized biomass in an industrial combustion test furnace. Fuel 86, 1959–1965.

Marchioli, C., Fantoni, M., Soldati, A., 2010. Orientation, distribution, and deposition of elongated, inertial fibers in turbulent channel flow. Phys. Fluids 22, 033301.

Marchioli, C., Picciotto, M., Soldati, A., 2007. Influence of gravity and lift on particle velocity statistics and transfer rates in turbulent vertical channel flow. Int. J. Multiph. Flow. 33, 227–251.

Marchioli, C., Soldati, A., 2002. Mechanisms for particle transfer and segregation in a turbulent boundary layer. J. Fluid Mech. 468, 283–315.

Marchioli, C., Soldati, A., Kuerten, J.G.M., Arcen, B., Tanière, A., Goldensoph, G., Squires, K.D., Cargnelutti, M.F., Portela, L.M., 2008. Statistics of particle dispersion in direct numerical simulations of wall-bounded turbulence: results of an international collaborative benchmark test. Int. J. Multiph. Flow. 34, 879–893.

Marcus, G.G., Parsa, S., Kramel, S., Ni, R., Voth, G.A., 2014. Measurements of the solid-body rotation of anisotropic particles in 3D turbulence. New J. Phys. 16, 102001.

Maxey, M.R., Riley, J.J., 1983. Equation of motion for a small rigid sphere in a nonuniform flow. Phys. Fluids 26, 883–889.

Mortensen, P.H., Andersson, H.I., Gillissen, J.J.J., Boersma, B.J., 2007. Particle spin in a turbulent shear flow. Phys. Fluids 19, 078109.

Mortensen, P.H., Andersson, H.I., Gillissen, J.J.J., Boersma, B.J., 2008a. Dynamics of prolate ellipsoidal particles in a turbulent channel flow. Phys. Fluids 20, 093302.

Mortensen, P.H., Andersson, H.I., Gillissen, J.J.J., Boersma, B.J., 2008b. On the orientation of ellipsoidal particles in a turbulent shear flow. Int. J. Multiph. Flow. 34, 678–683.

Ni, R., Kramel, S., Ouellette, N.T., Voth, G.A., 2015. Measurements of the coupling between the tumbling of rods and the velocity gradient tensor in turbulence. J. Fluid Mech. 766, 202–225.

Ni, R., Ouellette, N.T., Voth, G.A., 2014. Alignment of vorticity and rods with Lagrangian fluid stretching in turbulence. J. Fluid Mech. 743, R3.

Nilsen, C., Andersson, H.I., 2013. Chaotic rotation of inertial spheroids in oscillating shear flow. Phys. Fluids 25, 013303.

Nilsen, C., Andersson, H.I., Zhao, L., 2013. A Voronoï analysis of preferential concentration in a vertical channel flow. Phys. Fluids 25, 115108.

Njobuenwu, D.O., Fairweather, M., 2014. Effect of shape on inertial particle dynamics in a channel flow. Flow. Turbul. Combust. 92, 83–101.

Njobuenwu, D.O., Fairweather, M., 2015. Dynamics of single, non-spherical ellipsoidal particles in a turbulent channel flow. Chem. Eng. Sci. 123, 265–282.

Olson, J.A., 2001. The motion of fibres in turbulent flow, stochastic simulation of isotropic homogeneous turbulence. Int. J. Multiph. Flow. 27, 2083–2103.

Ozolins, A., Strautins, U., 2014. Simple models for wall effect in fiber suspension flows. Math. Model. Anal. 19, 75–84.

Parsa, S., Calzavarini, E., Toschi, F., Voth, G.A., 2012. Rotation rate of rods in turbulent fluid flow. Phys. Rev. Lett. 109, 134501.

Parsa, S., Guasto, J.S., Kishore, M., Ouellette, N.T., Gollub, J.P., Voth, G.A., 2011. Rotation and alignment of rods in two-dimensional chaotic flow. Phys. Fluids 23, 043302.

Qi, D., Luo, L.-S., 2003. Rotational and orientational behaviour of three-dimensional spheroidal particles in Couette flows. J. Fluid Mech. 477, 201–213.

Rosén, T., Do-Quang, M., Aidun, C.K., Lundell, F., 2015. The dynamical states of a prolate spheroidal particle suspended in shear flow as a consequence of particle and fluid inertia. J. Fluid Mech. 771, 115–158.

Rosén, T., Lundell, F., Aidun, C.K., 2014. Effect of fluid inertia on the dynamics and scaling of neutrally buoyant particles in shear flow. J. Fluid Mech. 738, 563–590.

Rouson, D.W.I., Eaton, J.K., 2001. On the preferential concentration of solid particles in turbulent channel flow. J. Fluid Mech. 428, 149–169.

Shapiro, M., Goldenberg, M., 1993. Deposition of glass fiber particles from turbulent air flow in a pipe. J. Aerosol Sci. 24, 65–87.

Shin, M., Koch, D.L., 2005. Rotational and translational dispersion of fibres in isotropic turbulent flows. J. Fluid Mech. 540, 143–173.

Siewert, C., Kunnen, R.P.J., Meinke, M., Schröder, W., 2014. Orientation statistics and settling velocity of ellipsoids in decaying turbulence. Atmos. Res. 142, 45–56.

Subramanian, G., Koch, D.L., 2006. Inertial effects on the orientation of nearly spherical particles in simple shear flow. J. Fluid Mech. 557, 257–296.

Uijttewaal, W.S.J., Oliemans, R.V.A., 1996. Particle dispersion and deposition in direct numerical and large eddy simulations of vertical pipe flows. Phys. Fluids 8, 2590–2604.

Yin, C., Rosendahl, L., Knudsen Kær, S., Sørensen, H., 2003. Modelling the motion of cylindrical particles in a nonuniform flow. Chem. Eng. Sci. 58, 3489–3498.

Yu, Z., Phan-Thien, N., Tanner, R.I., 2007. Rotation of a spheroid in a Couette flow at moderate Reynolds numbers. Phys. Rev. E 76, 026310.

Zastawny, M., Mallouppas, G., Zhao, F., van Wachem, B.G.M., 2012. Derivation of drag and lift force and torque coefficients for non-spherical particles in flows. Int. J. Multiph. Flow. 39, 227–239.

Zhang, H., Ahmadi, G., Fan, F.G., McLaughlin, J.B., 2001. Ellipsoidal particles transport and deposition in turbulent channel flows. Int. J. Multiph. Flow. 27, 971–1009.

Zhao, F., van Wachem, B.G.M., 2013. Direct numerical simulation of ellipsoidal particles in turbulent channel flow. Acta Mech. 224, 2331–2358.

Zhao, L., Andersson, H.I., Gillissen, J.J.J., 2013. Interphasial energy transfer and particle dissipation in particle-laden wall turbulence. J. Fluid Mech. 715, 32–59.

Zhao, L., Challabotla, N.R., Andersson, H.I., Variano, E.A., 2015. Rotation of nonspherical particles in turbulent channel flow. Phys. Rev. Lett. 115, 244501.

Zhao, L., Marchioli, C., Andersson, H.I., 2014. Slip velocity of rigid fibers in turbulent channel flow. Phys. Fluids 26, 063302.

Zhao, L.H., Marchioli, C., Andersson, H.I., 2012. Stokes number effects on particle slip velocity in wall-bounded turbulence and implications for dispersion models. Phys. Fluids 24, 021705.

Article 7

Orientation and rotation dynamics of tracer triaxial ellipsoidal particles in wall turbulence

Niranjan Reddy Challabotla, Lihao Zhao & Helge I. Andersson

Submitted to *Physics of Fluids*.

Orientation and rotation dynamics of triaxial ellipsoidal tracers in wall turbulence

Niranjan Reddy Challabotla[1], Lihao Zhao[1,2] and Helge I. Andersson[1]

[1] *Department of Energy and Process Engineering,*
Norwegian University of Science and Technology (NTNU)
7491 Trondheim, Norway.

[2] *Department of Engineering Mechanics, Tsinghua University, 10084 Beijing, China*

Abstract. The rotational dynamics of triaxial ellipsoidal particles in turbulent channel flow have been explored. The non-inertial particles were traced in a Lagrangian way in an Eulerian flow field that resulted from a direct numerical simulation. Although the tracer particles translated along with the local fluid they did not adhere to the local fluid rotation. The triaxial ellipsoids were characterized by two independent shape parameters that both were varied from 0.1 to 10. In spite of the anisotropic turbulence in the channel center the tumbling of the particles closely resembled earlier results in homogeneous isotropic turbulence. The orientation of the particles varied substantially from the center to the near-wall region where triaxial particles tended to align their major axis in the mean flow direction and their minor axis in the wall-normal direction. These preferential alignments caused the ellipsoid to tumble as a rod about the major axis and like a disk about the minor axis. These observations show the dual nature of triaxial ellipsoids embedded in real turbulence.

I. INTRODUCTION

Non-spherical particles suspended in a fluid flow are frequently encountered, for instance aerosols inhaled into the human respiratory system or cellulose fibre suspensions in paper making. A better understanding of the complex dynamics of non-spherical particles is necessary to make advances in the management of such particle-fluid systems. The vast majority of earlier studies have focused on the dynamics of non-spherical particles by approximating the actual particle shape as an axisymmetric ellipsoid, i.e. either prolate (rod-like) or oblate (disk-like) spheroids; see e.g.[1, 2]. Attempts to study the dynamical behaviour of non-axisymmetric particles are scarce and so far limited either to simple shear flows or isotropic turbulence.

Jeffery[3] derived analytical expressions for the torque acting on a triaxial ellipsoidal particle immersed in creeping shear flow. He also showed that inertia-free axisymmetric particles rotate in closed periodic orbits, so-called Jeffery orbits, which in addition to their aspect ratio are dependent on the initial orientation of the tracer particles. Numerical examples reported by Gierszewski and Chaffey[4] showed that the motion of a non-axisymmetric particle in a simple shear flow is qualitatively different from that of an axisymmetric particle. Hinch and Leal[5] showed that any deviations from axisymmetric spheroidal geometry resulted in a substantial change in the particle's rotational motion and found that the motion of a triaxial ellipsoid with comparable axes is doubly periodic. The existence of chaotic rotational motion of triaxial particles in simple shear flows was reported for non-inertial particles[6] and for inertial particles.[7] Even slight imperfections of a spheroidal shape can produce substantial effects on the rotational particle dynamics.[8] They also demonstrated that the tumbling of the particle may indeed be periodic, doubly periodic, or possibly chaotic, depending on particle shape and initial orientation.

Recently, Chevillard and Meneveau[9] generalized results of Parsa, et al.[10] by reporting orientation statistics and rotation rates of tracer triaxial ellipsoidal particles suspended in homogeneous isotropic turbulence (HIT). To the present authors' best knowledge, no other study has reported on rotation dynamics of triaxial particles in a turbulent environment. We anticipate that the orientational and rotational behaviour of triaxial ellipsoids are completely different in anisotropic wall turbulence than in HIT. To explore these differences, we simulate triaxial tracer particles suspended in fully-developed turbulent channel flow. This work represents a generalization of our simulations of axisymmetric tracer particles by Challabotla, et al.[11] and aims to uncover the influence of triaxiality on the particle dynamics.

II. METHODOLOGY

A. Mathematical modelling

We adopt an Eulerian-Lagrangian approach to study the dynamics of triaxial ellipsoidal tracer particles suspended in a fully-developed turbulent channel flow. The continuous fluid phase is governed by the incompressible Navier-Stokes equations. The continuous fluid phase is represented in an Eulerian inertial frame (x, y, z) which spans the computational domain in streamwise x, spanwise y and wall-normal z directions. A Lagrangian particle is represented in the particle-frame (x′, y′, z′) with its origin in the particle center-of-mass such that the coordinate axes are aligned with the principal directions of the triaxial particle (see Figure 1). The particle orientation is represented by four Euler parameters which are derived from the three Euler angles. The variables are transformed from one frame of reference to the other using an orthogonal transformation matrix A_{ij}, e.g. $x_i = A_{ij}x'_j$. See [12, 13] for details.

A triaxial ellipsoidal particle with semi-axes a, b and c is defined as

$$\frac{x'^2}{a^2}+\frac{y'^2}{b^2}+\frac{z'^2}{c^2}=1. \tag{1}$$

The geometrical shape is completely characterized by means of the two aspect ratios parameters $\lambda_1 = b/a$ and $\lambda_2 = c/a$. This parametrization represents a direct generalization of that used in our earlier studies of axisymmetric ellipsoids with two equal semi-axes a = b,[11, 13, 14] whereas Chevillard and Meneveau[9] instead adopted the reciprocal parameters λ_1^{-1} and λ_2^{-1}.

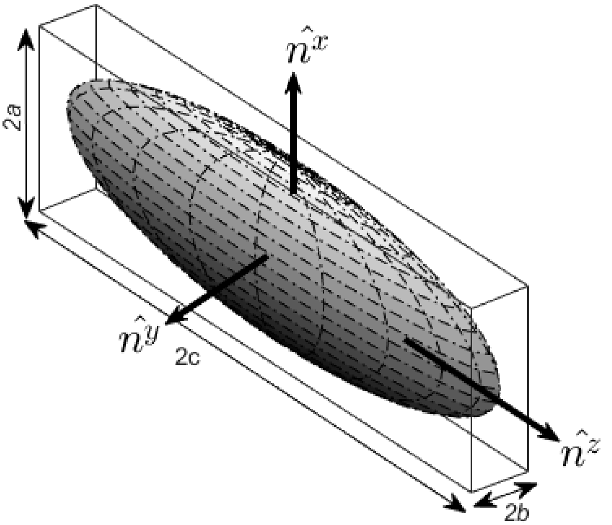

FIG. 1. A triaxial ellipsoidal particle with three semi-axes *a*, *b* and *c*. The particle unit orientation vectors $\hat{n}^x, \hat{n}^y$ and $\hat{n}^z$ completely define the orientation of the particle.

In absence of particle inertia, the translational motion of the triaxial particles coincides with the fluid flow whereas the rotational motion adjusts itself such that the Jeffery-torques[3] vanish exactly at every instant of time, i.e.

$$\begin{aligned} \omega_x' &= \left(\frac{\lambda_1^2 - \lambda_2^2}{\lambda_1^2 + \lambda_2^2}\right) S_{yz}' + \Omega_x' \\ \omega_y' &= \left(\frac{\lambda_2^2 - 1}{\lambda_2^2 + 1}\right) S_{xz}' + \Omega_y' \\ \omega_z' &= \left(\frac{1 - \lambda_1^2}{1 + \lambda_1^2}\right) S_{yx}' + \Omega_z' \end{aligned} \tag{2}$$

where the primes indicate that the variables are referred to the particle frame-of-reference. This set of equations demonstrate the coupling between the particle rotation vector ω_i' and fluid rotation vector Ω_i' and the fluid strain rate tensor S_{ij}' in the particle frame. We follow the same approach as that used by Challabotla, et al.[11] and deduce the time evolution of ω_i' from equation (2) as the tracer particles are carried passively along with the local fluid. Chevillard and Meneveau[9] adopted an alternative approach and integrated an equation for the time rate-of-change of the unit orientation vector $\hat{\mathbf{n}}$ derived by Junk and Illner[15] using Lagrangian time histories of the velocity gradient tensor.

The rate of rotation or *tumbling* of a particle's orientation vectors is defined as the sum of rotation about the two other semi-axis, as in Chevillard and Meneveau[9]. For example, the rotation rate of the particle unit orientation vector $\hat{n}^x$ is

$$\langle \dot{\hat{n}}^x \dot{\hat{n}}^x \rangle = \langle \omega'_z \omega'_z \rangle + \langle \omega'_y \omega'_y \rangle \, . \tag{3}$$

The particle *enstrophy* $\langle \omega'_i \omega'_i \rangle$ defined as

$$\langle \omega'_i \omega'_i \rangle = \langle \omega'_x \omega'_x \rangle + \langle \omega'_y \omega'_y \rangle + \langle \omega'_z \omega'_z \rangle \tag{4}$$

is a scalar measure of the overall rotation.

B. Computational details

The frictional Reynolds number based on the channel half-height h and the friction velocity u_τ is $Re_\tau = 180$. The friction velocity is defined in terms of the wall shear stress τ_w as $u_\tau = (\tau_w/\rho)^{1/2}$ where τ_w is balancing the prescribed driving mean pressure gradient. All variables are normalized by viscous scales for velocity (u_τ), length (ν/u_τ), and time (ν/u_τ^2). The size of the computational domain is $12h \times 6h \times 2h$ in the streamwise, spanwise and wall-normal directions, respectively, and 192 grid points are used in each coordinate direction. The grid resolution in the streamwise and spanwise directions become $\Delta x^+ = 11.3$ and $\Delta y^+ = 5.6$, while the non-uniform grid spacing in the wall-normal direction varies from $\Delta z^+ = 0.9$ next to the walls to 2.86 in the channel center. The time integration is performed with a constant time step $\Delta t^+ = 0.036$. Periodic boundary conditions are used in the two homogeneous directions and no-slip and impermeability conditions are imposed at the channel walls. These numerical parameters are the same as those used in our recent simulations.[11, 14, 16]

The size of the triaxial particles is smaller than the Kolmogorov length scale and the particle suspension is assumed to be sufficiently dilute to justify one-way coupled simulations where any feedback from the particles on the fluid phase, as well as particle-particle collisions, can be neglected. A particle is assumed to collide with a wall if the particle center comes closer to the wall than a distance equal to the semi-axis a. The rarely occurring collisions are modelled as fully elastic so that the particle maintains its linear and angular momentum in the two homogeneous directions after a collision.

Simulations are performed for a total of 25 different particle shapes by varying both particle aspect ratios λ_1 and λ_2 in the range from 0.1 to 10. 500 000 particles of each shape, all with semi-axis $a^+ = 0.36$ are randomly injected into the same turbulence field at time $t^+ = 0$. Orientational and rotational particle statistics are computed by averaging instantaneous data in time between $720\nu/u_\tau^2$ and $2520\nu/u_\tau^2$ as well as in the homogeneous streamwise and spanwise directions.

III. RESULTS AND DISCUSSIONS

In this section we first present results that show how the tumbling rate depends on particle shape (λ_1, λ_2) and how the tumbling behaviour changes from the channel center ($z^+ = 180$) to the wall region ($z^+ = 10$). We thereafter explore how the triaxial ellipsoids align with and rotate about the coordinate axes of the Eulerian reference frame.

A. Tumbling rates in the Lagrangian reference frame

Figure 2 shows the variance of the rate of rotation of the three particle orientation vectors together with the particle enstrophy in the channel center as a function of the two particle aspect ratios. The rate of rotation of the orientation vector $\hat{n}^x$ in Figure 2(a) shows that the tumbling rate about this principal axis varies symmetrically about the diagonal $\lambda_1 = \lambda_2$ that represents axisymmetric ellipsoids, i.e. spheroidal particles. The tumbling rate increases monotonically from 0.10 in the lower left corner ($\lambda_1 = \lambda_2 << 1$) to 0.22 in the upper right corner ($\lambda_1 = \lambda_2 >> 1$) along this diagonal, i.e. from long rod-like to flat disk-like particles. These data are consistent with recent results for inertia-free spheroids in the center of a channel flow due to Zhao, et al.[14]. The results are moreover in close agreement with similar results for axisymmetric particles in HIT reported[9, 10, 17] with a value of about 0.09 for long rods, 0.17 for spheres, and 0.24 for thin disks. This dependence of the tumbling rate on particle shape has been explained by the alignment between the spheroid's orientation vector and the fluid vorticity; see e.g.[14, 17, 18]. For the triaxial particles, we observe that the rotation rate $\hat{n}^x$ in the first quadrant (Q1) resembles that of oblate spheroids and in the third quadrant (Q3) that of prolate spheroids. This is to be expected since $\hat{n}^x$ is along the shortest and longest semi-axis in Q1 and Q3, respectively. However, the intermediate semi-axis *a* is in the $\hat{n}^x$ - direction along the diagonal line $\lambda_2 = (\lambda_1)^{-1}$ with $c > a > b$ in Q2 and $c < a < b$ in Q4. Such triaxial ellipsoids can be categorized by the single shape parameter $\Lambda \equiv \lambda_2 = (\lambda_1)^{-1}$ and the data plotted in Figure 2(a) show only little variation with Λ from ≈ 0.16 for spherical particles ($\Lambda = 1$) with a slightly increasing trend with increasing asphericity $|\Lambda|$.

From Figure 2(b), we can observe that the rotation rate of $\hat{n}^y$ along the diagonal line $\lambda_2 = (\lambda_1)^{-1}$ varies similarly as along the diagonal $\lambda_2 = \lambda_1$ in Figure 2(a). Particles in Q4 have the major axis in the $\hat{n}^y$ -direction and rotate similarly as prolate spheroids and particles in Q2 have their minor axis along the y'- direction and thus rotate similarly as oblate spheroids. Chevillard and Meneveau[9] pointed out that the rotation rate about $\hat{n}^z$ as a function of λ_1 and λ_2 is identical with the rotation rate of $\hat{n}^y$ as function of λ_2 and λ_1 for symmetry reasons. However, for the sake of completeness, computed data for the rotation rate of $\hat{n}^z$ are shown in Figure 2(c). This plot appears as an almost perfect mirror image of that in Figure 2(b) and accordingly serves as verification of our implementation of the triaxial tracer particle model.

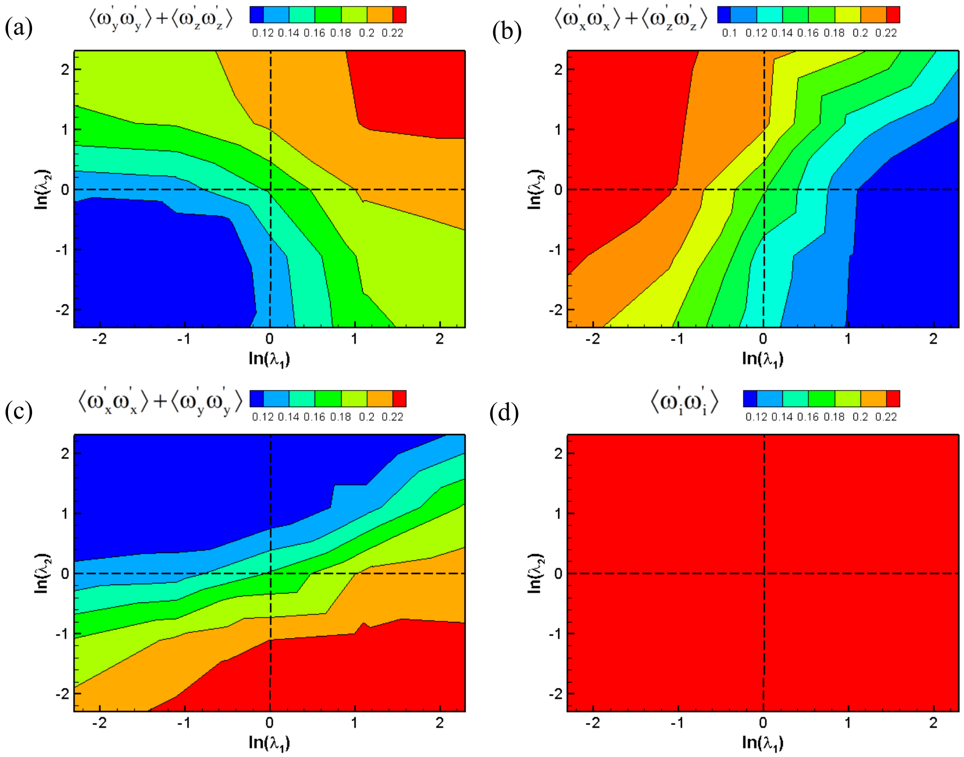

FIG. 2. Variance of tumbling and rotation rates at the channel center $z^+ = 180$ normalized by the local Kolmogorov time scale $(\nu/\varepsilon)^{1/2}$. Rate of rotation of particle orientation vectors (a) $\hat{n}^x$, b) $\hat{n}^y$, (c) $\hat{n}^z$ and (d) particle enstrophy $\langle\omega'_i\omega'_i\rangle$. The plots are for convenience divided into four quadrants Qi and the colour-coding is the same in all the plots.

According to the results in Figure 2, we can infer that triaxial ellipsoids may exhibit a dual nature, i.e. tumbling like a disk about one axis and as a rod about another axis. Fourth-quadrant ($\lambda_1 > 1 > \lambda_2$) particles, for instance, tumble weakly about $\hat{n}^y$ in Figure 2(b) (rod-like behaviour) but vigorously about $\hat{n}^z$ in Figure 2(c) (disk-like wobbling). This hybrid rotational nature is a unique feature of triaxial particles and will be further explored in the remainder of the paper.

Figure 2(d) shows the kinetic energy associated with the particle's overall rotation defined in equation (4), the so-called particle enstrophy. The enstrophy of axisymmetric tracer ellipsoids, i.e. $\lambda_2 = \lambda_1$, has recently been observed to be almost independent of particle aspect ratio and only marginally higher for rods than for disks and attain almost the same level (≈ 0.25) in isotropic turbulence[17] as in a channel center.[14]

The present results are from the center region of a turbulent channel flow where the velocity field is known to be anisotropic. Nevertheless, the results in Figure 2(a, b) closely resemble the corresponding results obtained by Chevillard and Meneveau[9] in HIT. These striking similarities might therefore seem surprising in view of the anisotropic velocity field that prevails in the channel center and suggest that particle rotation is primarily affected by fluid rotation (i.e. vorticity) which is almost isotropic midway between the two parallel channel walls.[19]

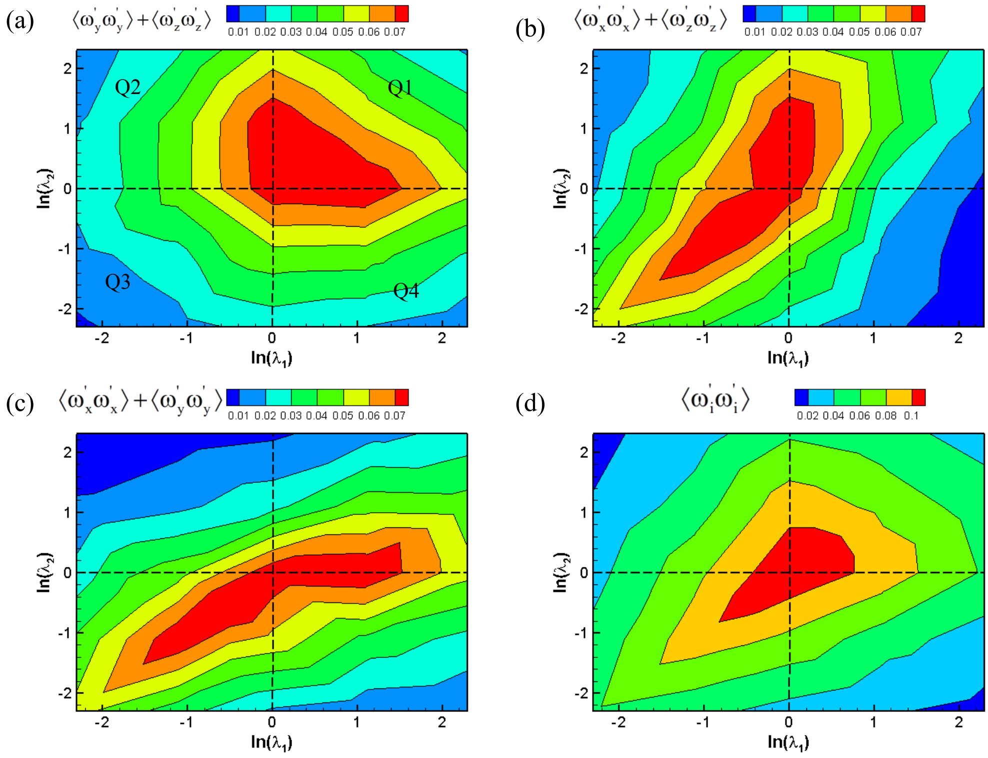

FIG. 3. Variance of tumbling and rotation rates in the near-wall region at $z^+ \approx 10$ normalized by the viscous time scale time (ν / u_τ^2). Rate of rotation of particle orientation vectors (a) $\hat{n}^x$, b) $\hat{n}^y$, (c) $\hat{n}^z$ and (d) particle enstrophy $\langle \omega_i'\omega_i' \rangle$. Notice the different colour-coding in (d).

Figure 3 shows the rate of rotation of the particle orientation vectors (tumbling rates) and the particle enstrophy at z^+ = 10. The turbulent velocity and vorticity fields are highly anisotropic at this particular location in the buffer region of the turbulent boundary layer. While the particle enstrophy in the channel center was almost independent of particle shape in

Figure 2(d), the enstrophy in the wall region in Figure 3(d) exhibits a distinct maximum for spherical particles. The particle enstrophy is strongly damped as the particles become increasingly aspherical, as for the axisymmetric particles along the diagonal line $\lambda_1 = \lambda_2$. This is consistent with the results reported by Zhao, et al.[14] that the rotational energy is substantially reduced both for disk-like (Q1) and rod-like (Q3) spheroids in wall turbulence. This damping with increasing particle asphericity was ascribed to the well-known preferential particle orientation observed in water-table flow experiments[20, 21] as well as in channel flow computer simulations.[11, 12, 14, 22]

The damping of the particle enstrophy with increasing asphericity is significantly stronger for non-axisymmetric particles than for spheroids. This can be seen by comparing the data along the diagonal line $\lambda_2 = (\lambda_1)^{-1}$ with the enstrophy along the diagonal $\lambda_2 = \lambda_1$ in Figure 3(d). The ability of an anisotropic ellipsoid to adhere to the rotation of the local fluid is thus reduced with increasing departure from sphericity and this tendency is more pronounced for non-axisymmetric particles than for spheroids.

The tumbling rates about the three particle axes in Figures 3(a, b, c) are distinctly different from those at the channel center in Figure 2(a, b, c) and nearly spherical particles ($\lambda_1 \approx \lambda_2 \approx 1$) tumble more than the others. In the channel center, however, disks tumbled more than rods about their symmetry axis and non-axisymmetric ellipsoids tumbled primarily about their shortest semi-axis. In spite of the striking differences between Figure 2 and Figure 3, disk-like particles are still more amenable to tumble than rods (see Figure 3(a)), but maximum tumbling occurs for modest asphericity and not for infinitely thin disks ($\lambda_1 \approx \lambda_2 \rightarrow \infty$) as in Fig. 2(a).

The highest tumbling rates about $\hat{n}^y$ are observed for $\lambda_2 > \lambda_1 \approx 1$ and for $\lambda_1 \approx \lambda_2 < 1$ in Figure 3(b). Such triaxial ellipsoids are close to being axisymmetric ($c > b \approx a$ and $c \approx b < a$, respectively) and tumble intensively about a short axis. This contrasts with the rotational behaviour in the channel center where the highest tumbling rate about $\hat{n}^y$ occurred for highly triaxial particles, i.e. $\Lambda >> 1$. Once again, the variation of the tumbling rate about $\hat{n}^z$ in Figure 3(c) appears as a mirror image of that in Figure 3(b).

B. Orientation and rotation in the Eulerian reference frame

The rotational dynamics of any non-spherical particle is believed to depend on how the particle orient itself in a turbulent flow field. The different states of particle rotation are therefore distinctly different in isotropic turbulence and anisotropic wall turbulence. Orientation statistics of axisymmetric particles in wall turbulence have been reported by several authors, e.g.[11, 13, 14, 23]. Chevillard and Meneveau[9] investigated how triaxial tracers oriented relative to the local fluid vorticity vector and to the eigendirections of the strain-rate tensor in HIT. They reported results for particle shapes along the two diagonals $\lambda_2 = \lambda_1$ and $\lambda_2 = (\lambda_1)^{-1}$. In the present study, however, we focus on orientation statistics of triaxial ellipsoids with axes c > a > b along the diagonal $\Lambda = \lambda_2 = (\lambda_1)^{-1} > 1$ in the second quadrant of Figures 2 and 3. The particle's major axis is thus in the z'-direction and the minor axis is in the y'-direction of the particle frame-of-reference. The direction cosines based on the angles θ_x, θ_y, θ_z between the principle axes of a particle and the coordinate axes x, y, z of the inertial frame-of-reference define the particle's orientation in the channel.

Figure 4 shows the variation of the orientation of the particles' major axis ($\hat{n}^z$) to the left and minor axis ($\hat{n}^y$) to the right all the way from the wall at $z^+ = 0$ to the channel center. Results for moderate ($\Lambda = 3$) and high ($\Lambda = 10$) triaxiality are compared with results for axisymmetric ellipsoids, i.e. spheroids, along the diagonal $\lambda_2 = \lambda_1$ in Q3 characterized here by the single parameter $\lambda \equiv \lambda_2^{-1} = \lambda_1^{-1}$. In the center of the channel, the direction cosines are all close to 0.5 which reflects randomly oriented particles. Although Chevillard and Meneveau[9] found that triaxial tracers were preferentially oriented relative to properties of the local flow field, the particle orientation relative to any fixed direction is randomized due to the isotropy of the turbulence field. In the center of the channel flow, however, a weak preference of the triaxial particles to align their major axis in the x-direction can be observed with $<|\cos\theta_x|>$ slightly above 0.5. This is obviously an effect of the modest anisotropy of the turbulence in the channel center where the velocity fluctuations in the streamwise directions are larger than in the other directions. Moreover, the spanwise vorticity fluctuations are slightly higher than those in the two other directions [19]. The modest preference for alignment with the mean flow direction (x) rather than with the direction of mean vorticity and largest vorticity fluctuations (y) is different from observations in completely isotropic turbulence where rod-like particles align with the vorticity direction.

The tendency of triaxial ellipsoids to align their major axis in the x-direction becomes gradually more pronounced as the wall is approached and closely resembles the trend observed for rod-like particles. Similarly, the minor axis of the triaxial ellipsoids tends to align in the wall-normal direction, just like disk-like spheroids orient their symmetry axis perpendicular to the wall. These dual tendencies become even more pronounced for $\Lambda = 10$ than for $\Lambda = 3$.

The strongest tendency of the major axis of the triaxial ellispoids to align with the mean flow direction occurs in the buffer region ($z^+ \approx 15$) for $\Lambda = 3$ and in the viscous sub-layer ($z^+ \approx 5$) for $\Lambda = 10$ whereas the preferential wall-normal orientation of the minor axis prevails all the way to the wall. All trends observed are the same for triaxial ellipsoids parameterized by Λ and axisymmtric ellipsoids parameterized by λ, but the shape dependence is most pronounced for the triaxial particles.

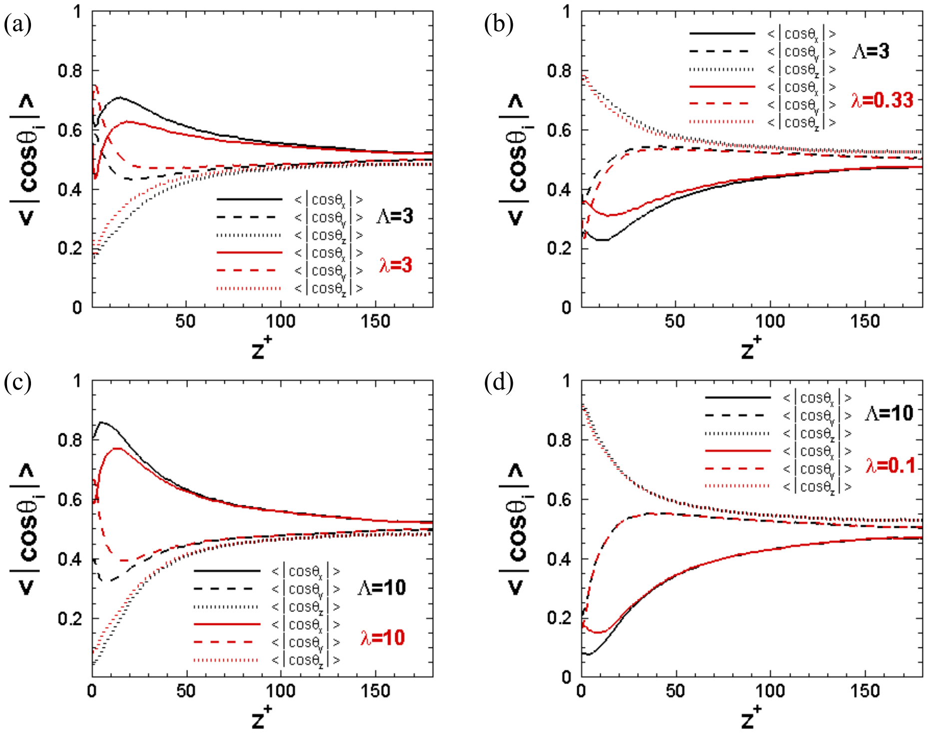

FIG. 4. Mean absolute direction cosines of the particle major axis ($\hat{n}^z$) and minor axis ($\hat{n}^y$) with respect to the inertial frame-of-reference for (a, b) Λ=3 and (c, d) Λ=10. (a, c) particle major axis ($\hat{n}^z$) and (b, d) particle minor axis ($\hat{n}^y$). Results for corresponding axisymmetric particles are also plotted.

Voth[24] pointed out that neutrally buoyant spheroidal particles undergo periodic motions called Jeffery orbits in simple shear flow. Here, oblate spheroids that brings their symmetry axis near the wall-normal direction will spend a long time in this orientation before tumbling, and this leads to the observed orientation in Figure 4(d) for $\lambda = 0.1$. The orientation of three-axial ellipsoids with $\Lambda = 10$ is almost indistinguishable from that of oblate spheroids, thereby suggesting that the same reasoning also applies for asymmetric particles.

The hybrid nature of the orientational statistics in Figure 4, namely that the major axis orientates as a rod-like particle and the minor axis as a disk-like particle, is consistent with the dual nature of the various tumbling rates shown in Figures 2 and 3. The different modes of orientation and rotation are determined by the two geometrical parameters λ_1 and λ_2 as well as by the anisotropy of the ambient flow field.

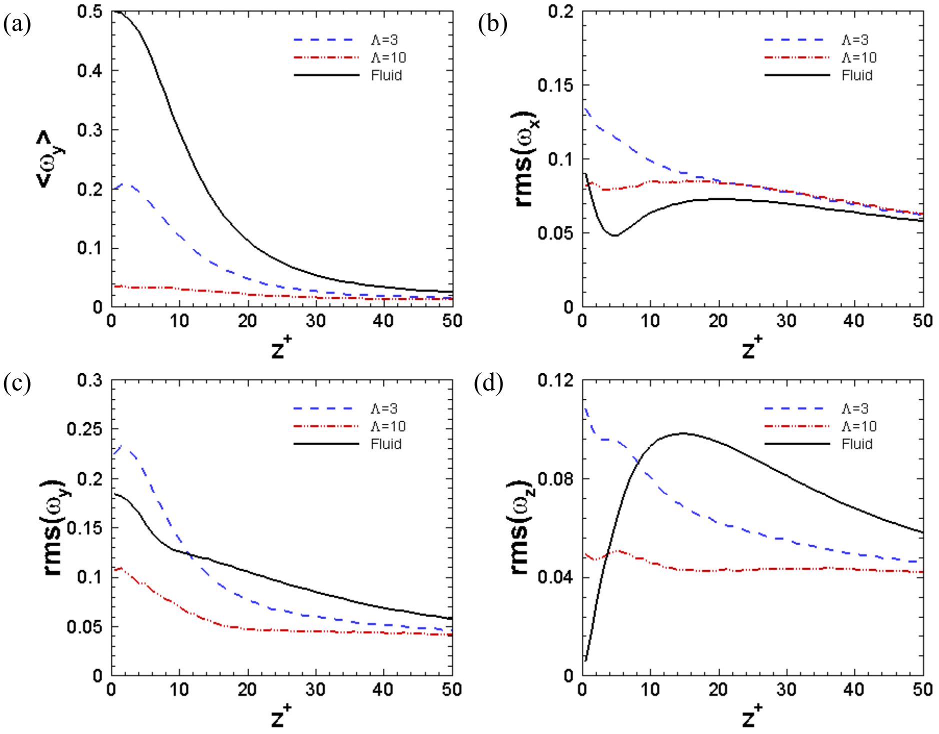

FIG. 5. Mean and fluctuating particle angular velocity components ω_i for $\Lambda = 3$ and $\Lambda = 10$ in the inertial frame of the reference. The corresponding fluid angular velocity components Ω_i are shown as black solid lines. (a) mean spanwise angular velocity $<\omega_y>$ and angular velocity fluctuations in the (b) streamwise direction rms(ω'_x); (c) spanwise direction rms(ω'_y); (d) wall-normal direction rms(ω'_z).

The spanwise component $<\omega_y>$ of the mean angular velocity is shown in Figure 5(a), whereas the two other mean spin components are zero in the present flow configuration for symmetry reasons. It has been reported that the mean spanwise component $<\omega_y>$ of axisymmetric tracer particles is damped compared to spherical particles and this trend is strongly dependent on the particle aspect ratio λ.[11, 22] The same monotonic trend can be observed also for the triaxial particles with $\Lambda = \lambda_2 = (\lambda_1)^{-1}$, but with an even stronger damping of $<\omega_y>$ with increasing triaxiality Λ. The $\Lambda = 10$ particles rotate at a rate ≈ 0.04, i.e. below 10 per cent of the normalized rotation rate 0.5 of tracer spheres. Recall that spherical tracers adhere to the local fluid rotation due to their isotropic shape. This finding suggests that strong alignment of the major axis in the streamwise direction and of the minor axis in the wall-normal direction tends to reduce $<\omega_y>$ in the near-wall region. In the logarithmic layer ($z^+ > 30$), however, the results for $\Lambda = 3$ and $\Lambda = 10$ are surprisingly close. The shape matters most in the vicinity of the channel walls, and this observation is indeed consistent with the orientation statistics in Figure 4.

Figures 5(b, c, d) show the effect of particle shape on the particle's angular velocity fluctuations. Similar to axisymmetric tracer particles, we observe that triaxial particles exhibit stronger fluctuations of the streamwise angular velocity ω_x than fluid vorticity fluctuations (tracer spheres), as shown in Figure 5(b). This cannot be caused by the particle's preferential sampling of high-vorticity regions since tracer particles do not concentrate preferentially. The stronger angular velocity fluctuations can probably be attributed to the preferentially alignment of particle's major axis in the streamwise x-direction, as shown in Figures 4(a, c). From Figure 5(c) we can observe that the angular velocity fluctuations in spanwise direction for $\Lambda = 10$ particles are consistently lower than for $\Lambda = 3$ and for spheres in the near-wall region. This reduction is probably associated with the strong preferential alignment of the minor axis of these particles in the wall-normal direction which makes them less susceptible to the intense fluid vorticity fluctuations. For $\Lambda = 3$, however, the preferential orientation is weaker (see Figure 4b) and these particles therefore rotate faster as a result of the vigorous near-wall turbulence.

As mentioned in Section IIIA, triaxial particles rotate and orient similarly as rod-like or disk-like particles depending on the direction considered and the two particle aspect ratios. However, in the laboratory frame, triaxial ellipsoids rotate in a more complex way because each component of the angular rotation vector in the inertial frame is a combination of three components in the particle frame. This makes the rotation of triaxial particles in the laboratory frame difficult to foresee and interpret since the relevant combination of angular rotation rates also largely depends on the particle orientations. We can therefore conclude that the dynamics of triaxial particles is similar to that of one type of axisymmetric particles in a certain direction, but resembles that of another type of axisymmetric particles in another direction in both the Lagrangian particle frame and in the Eulerian laboratory frame, but the underlying physical mechanisms are different. Moreover, the degree of these similarities between triaxial and axisymmetric particles depends on the actual aspect ratios λ_1 and λ_2.

IV. CONCLUDING REMARKS

Results aimed to show the orientational and rotational behaviour of triaxial tracer particles in turbulent channel flow have been presented. The results were obtained by tracing inertia-free ellipsoids in numerically simulated channel flow turbulence. The particle aspect ratios λ_1 and λ_2 were varied independently from 0.1 to 10 to cover the two-dimensional parameter space. The tumbling rates observed in the channel center closely resembled tumbling of triaxial ellipsoids in homogeneous isotropic turbulence reported by Chevillard and Meneveau[9]. The particle enstrophy turned out to be almost independent of particle shape. In the near-wall region, however, the particle enstrophy was highest for spherical particles and diminished with increasing asphericity. The reduction of the enstrophy was by far more pronounced for triaxial ellipsoids than for axisymmetric particles. We also inferred that triaxial ellipsoids exhibited a dual nature, namely tumbling like a disk about one axis and as a rod about another axis.

The orientation of triaxial ellipsoids with $\lambda_2 = \lambda_2^{-1} > 1$ varied substantially from the channel center to the wall. The tendency of these triaxial particles to align their major axis in the mean flow direction and their minor axis in the wall-normal direction is another manifestation of the hybrid nature of the dynamics of triaxial particles: their major axis orients as a rod-like particle and their minor axis as a disk-like particle. The strong alignment of the major axis in the streamwise direction and of the minor axis in the wall-normal direction in the near-wall region gave rise to a substantial reduction of the mean angular rotation rate. Similar to axisymmetric tracers we observed that triaxial particles exhibited stronger fluctuations of the streamwise angular velocity than tracer spheres. This finding can also be caused by the preferentially alignment of particle's major axis in the streamwise x-direction.

Shape has been observed to have stronger influence on the rotational behaviour of triaxial ellipsoids than for axisymmetric ellipsoids (i.e. spheroids) considered by Challabotla, et al.[11]. The observed trends are believed to result from the preferential orientation of the triaxial particles in the anisotropic wall turbulence. Particle inertia is known to dramatically alter the orientational and rotational behaviour of spheroidal particles, see e.g.[14]. A worthwhile extension of the present work would be to solve Euler's equations of rotational motion rather than equation (2) in order to explore how inertia affects the motion of triaxial ellipsoids.

ACKNOWLEDGEMENTS

This investigation has been supported by the Research Council of Norway through research grants No 213917 "Turbulent Particle Suspensions" and No 250744 "Turbulent Plankton Interactions" as well as computational resources through grant No NN2649K (Programme for Supercomputing).

REFERENCES

[1] H. I. Andersson, and A. Soldati, "Anisotropic particles in turbulence: status and outlook," Acta Mech. **224**, 2219 (2013).
[2] G. A. Voth, and A. Soldati, "Anisotropic Particles in Turbulence," Annu. Rev. Fluid Mech. **49**, In Press (2017).
[3] G. B. Jeffery, "The Motion of Ellipsoidal Particles Immersed in a Viscous Fluid," Proc. R. Soc. Lond. A **102**, 161 (1922).
[4] P. J. Gierszewski, and C. E. Chaffey, "Rotation of an isolated triaxial ellipsoid suspended in slow viscous flow," Canad. J. Phys. **56**, 6 (1978).
[5] E. J. Hinch, and L. G. Leal, "Rotation of small non-axisymmetric particles in a simple shear flow," J. Fluid Mech. **92**, 591 (1979).
[6] A. L. Yarin, O. Gottlieb, and I. V. Roisman, "Chaotic rotation of triaxial ellipsoids in simple shear flow," J. Fluid Mech. **340**, 83 (1997).
[7] F. Lundell, "The effect of particle inertia on triaxial ellipsoids in creeping shear: From drift toward chaos to a single periodic solution," Phys. Fluids **23**, 011704 (2011).
[8] J. Einarsson, B. M. Mihiretie, A. Laas, S. Ankardal, J. R. Angilella, D. Hanstorp, and B. Mehlig, "Tumbling of asymmetric microrods in a microchannel flow," Phys. Fluids **28**, 013302 (2015).

[9] L. Chevillard, and C. Meneveau, "Orientation dynamics of small, triaxial–ellipsoidal particles in isotropic turbulence," J. Fluid Mech. **737**, 571 (2013).
[10] S. Parsa, E. Calzavarini, F. Toschi, and G. A. Voth, "Rotation rate of rods in turbulent fluid flow," Phys. Rev. Lett. **109**, (2012).
[11] N. R. Challabotla, L. Zhao, and H. I. Andersson, "Shape effects on dynamics of inertia-free spheroids in wall turbulence," Phys. Fluids **27**, 061703 (2015).
[12] C. Marchioli, L. Zhao, and H. I. Andersson, "On the relative rotational motion between rigid fibers and fluid in turbulent channel flow," Phys. Fluids **28**, 013301 (2016).
[13] P. H. Mortensen, H. I. Andersson, J. J. J. Gillissen, and B. J. Boersma, "Dynamics of prolate ellipsoidal particles in a turbulent channel flow," Phys. Fluids **20**, 093302 (2008).
[14] L. Zhao, N. R. Challabotla, H. I. Andersson, and E. A. Variano, "Rotation of Nonspherical Particles in Turbulent Channel Flow," Phys. Rev. Lett. **115**, 244501 (2015).
[15] M. Junk, and R. Illner, "A New Derivation of Jeffery's Equation," J. math. fluid mech. **9**, 455 (2006).
[16] J. J. J. Gillissen, B. J. Boersma, P. H. Mortensen, and H. I. Andersson, "On the performance of the moment approximation for the numerical computation of fiber stress in turbulent channel flow," Phys. Fluids **19**, 035102 (2007).
[17] M. Byron, J. Einarsson, K. Gustavsson, G. Voth, B. Mehlig, and E. Variano, "Shape-dependence of particle rotation in isotropic turbulence," Phys. Fluids **27**, 035101 (2015).
[18] K. Gustavsson, J. Einarsson, and B. Mehlig, "Tumbling of Small Axisymmetric Particles in Random and Turbulent Flows," Phys. Rev. Lett. **112**, (2014).
[19] H. I. Andersson, L. Zhao, and E. A. Variano, "On the anisotropic vorticity in turbulent channel flows," ASME J. Fluids Eng. **137**, 084503 (2015).
[20] A. Abbasi Hoseini, F. Lundell, and H. I. Andersson, "Finite-length effects on dynamical behavior of rod-like particles in wall-bounded turbulent flow," Int. J. Multiphase Flow **76**, 13 (2015).
[21] M. Kvick, K. Håkansson, F. Lundell, L. Prahl Wittberg, and D. Söderberg, "Streak formation and fibre orientation in near wall turbulent fibre suspension flow," Ercoftac Bulletin **84**, 19 (2010).
[22] C. Marchioli, and A. Soldati, "Rotation statistics of fibers in wall shear turbulence," Acta Mech **224**, 2311 (2013).
[23] C. Marchioli, M. Fantoni, and A. Soldati, "Orientation, distribution, and deposition of elongated, inertial fibers in turbulent channel flow," Phys. Fluids **22**, 033301 (2010).
[24] G. A. Voth, "Disks aligned in a turbulent channel," J. Fluid Mech. **772**, 1 (2015).

Appendix

Appendix 1

Rotation of inertial triaxial ellipsoidal particles in wall turbulence

Niranjan Reddy Challabotla

2016.

In the present appendix, we reported the rotational behaviour of inertial triaxial ellipsoidal particles suspended in turbulent channel flow. A triaxial ellipsoidal particle with semi-axes a, b and c is characterized by means of the two aspect ratio parameters $\lambda_1 = b/a$ and $\lambda_2 = c/a$. Particle orientation is represented using Euler parameters and Euler angles as described for spheroidal particles in chapter 2. The methodology adopted to investigate translational and rotational motion of inertial triaxial particles is described briefly below:

The translational motion of the particle is governed by Newton's 2nd law as:

$$\mathrm{m_p}\frac{\mathrm{dv_i}}{\mathrm{dt}} = \pi\mu\mathrm{a}\left(\mathrm{R}_{\mathrm{Eul}}^{\mathrm{T}}\mathrm{K}'_{\mathrm{ij}}\mathrm{R}_{\mathrm{Eul}}\right)\Delta\mathrm{u_j} \tag{1}$$

The resistance tensor of an ellipsoid $\mathrm{K}'_{\mathrm{ij}}$ is a diagonal matrix given by (Oberbeck, 1876):

$$\mathrm{K}'_{\mathrm{ij}} = \begin{pmatrix} k_{\mathrm{x'x'}} & 0 & 0 \\ 0 & k_{\mathrm{y'y'}} & 0 \\ 0 & 0 & k_{\mathrm{z'z'}} \end{pmatrix} = 16\pi abc \begin{pmatrix} \dfrac{1}{\chi_0 + a^2\alpha_0} & 0 & 0 \\ 0 & \dfrac{1}{\chi_0 + b^2\beta_0} & 0 \\ 0 & 0 & \dfrac{1}{\chi_0 + c^2\gamma_0} \end{pmatrix}. \tag{2}$$

The shape parameters χ_0, α_0, β_0, and γ_0 are given by the following semi-integrals (Brenner, 1964):

$$\begin{aligned} \chi_0 &= abc\int_0^\infty \frac{d\lambda}{\varDelta} \\ \alpha_0 &= abc\int_0^\infty \frac{d\lambda}{\left(a^2+\lambda\right)\varDelta} \\ \beta_0 &= abc\int_0^\infty \frac{d\lambda}{\left(b^2+\lambda\right)\varDelta} \\ \gamma_0 &= abc\int_0^\infty \frac{d\lambda}{\left(c^2+\lambda\right)\varDelta} \\ \text{with } \varDelta &= \sqrt{\left(a^2+\lambda\right)\left(b^2+\lambda\right)\left(c^2+\lambda\right)}. \end{aligned} \tag{3}$$

These shape parameters for triaxial ellipsoidal particles are computed by using numerical integration. In the case of spheroidal particles, there exist analytical expression for shape parameters as shown in Table 2.1 in chapter 2.

Rotational motion of particle is governed in particle reference frame by Euler's equations as,

$$I'_{ij}\frac{d\omega'_j}{dt} + \epsilon_{ijk}\omega'_j I'_{kl}\omega'_l = N'_i \tag{4}$$

Moment of inertia tensor I'_{ij} for an ellipsoidal particle along the principal axes is given as,

$$\begin{pmatrix} I_{x'x'} & 0 & 0 \\ 0 & I_{y'y'} & 0 \\ 0 & 0 & I_{z'z'} \end{pmatrix} = \frac{4}{15}\pi\rho_p abc \begin{pmatrix} b^2+c^2 & 0 & 0 \\ 0 & a^2+c^2 & 0 \\ 0 & 0 & b^2+a^2 \end{pmatrix}. \tag{5}$$

The torque components N'_i for a triaxial ellipsoidal particle in creeping shear flow derived by Jeffery (1922):

$$\begin{pmatrix} N'_x \\ N'_y \\ N'_z \end{pmatrix} = \begin{pmatrix} \dfrac{16\pi\mu abc}{3\left(b^2\beta_0 + c^2\gamma_0\right)}\left[\left(b^2-c^2\right)S_{yz}{}' + \left(b^2+c^2\right)\left(\Omega_x{}' - \omega'_x\right)\right] \\ \dfrac{16\pi\mu abc}{3\left(c^2\gamma_0 + a^2\alpha_0\right)}\left[\left(c^2-a^2\right)S_{xz}{}' + \left(c^2+a^2\right)\left(\Omega_y{}' - \omega'_y\right)\right] \\ \dfrac{16\pi\mu abc}{3\left(a^2\alpha_0 + b^2\gamma_0\right)}\left[\left(a^2-b^2\right)S_{xz}{}' + \left(a^2+b^2\right)\left(\Omega_z{}' - \omega'_z\right)\right] \end{pmatrix} \tag{6}$$

The ability of an inertial particle to adjust to the ambient flow field can be estimated in terms of a particle response time τ_p. Shapiro and Goldenberg (1993) introduced a translational relaxation time based on the orientation-averaged resistance tensor $\bar{\bar{K}} = 3(k_{x'x'}^{-1} + k_{y'y'}^{-1} + k_{z'z'}^{-1})$. This is believed to be a relevant time scale for isotropically oriented particles and has been used by Mortensen et al. (2008); Challabotla et al. (2015) and others in their studies of axisymmetric spheroids. We now adopt the same definition of an equivalent response time for the triaxial ellipsoidal particles. By means of the elements of the translational resistance tensor in equation (2) , we can compute τ_p as,

$$\tau_p \equiv \frac{4D\pi abc}{3\nu}\frac{1}{\bar{\bar{K}}} \tag{7}$$

where D is the ratio between the particle and fluid density. A Stokes number St is then be defined as the ratio between τ_p and the viscous timescale $\tau_v = \nu / u_\tau^2$ based on the friction velocity u_τ and thus representative of the near-wall turbulence.

Simulation parameters used in the current DNS solver are same as adopted in article 7. Simulations are performed for a total of 25 different particle shapes by varying both particle aspect ratios λ_1 and λ_2 in the range from 0.1 to 10., all for Stokes number St = 30. Rotational particle statistics are computed by averaging instantaneous data in time between $5400\nu/u_\tau^2$ and $7920\nu/u_\tau^2$ and also in the homogeneous streamwise and spanwise directions. The rate of rotation or *tumbling* of a particle's orientation vectors and particle enstrophy are defined same as in article 7.

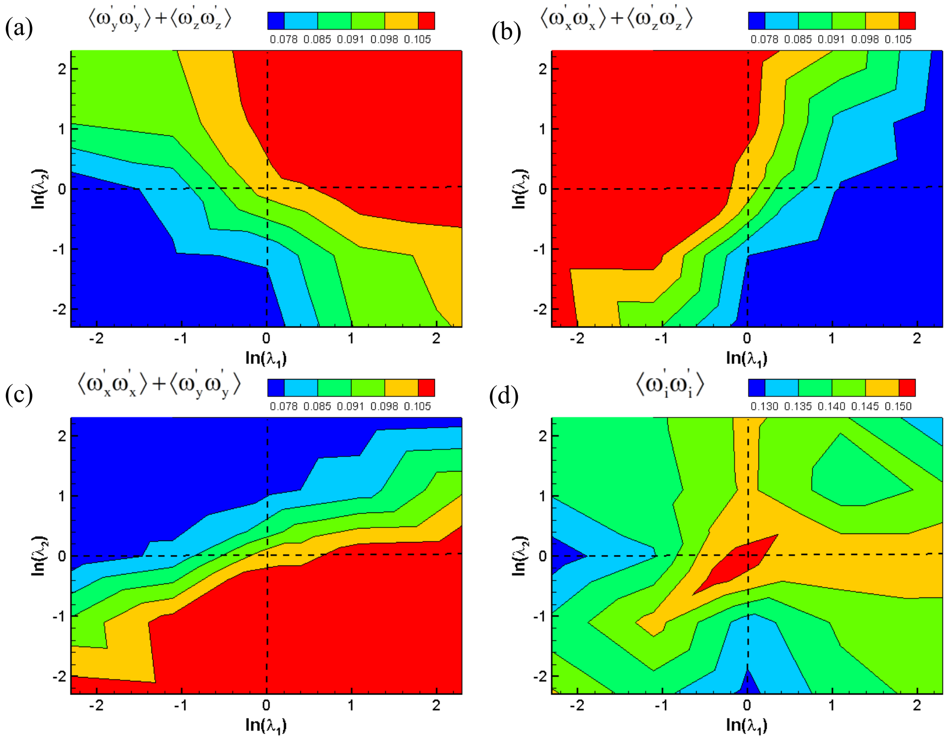

FIG. 2. Variance of tumbling and rotation rates at the channel center $z^+ = 180$ normalized by the local Kolmogorov time scale $(\nu/\varepsilon)^{1/2}$. Rate of rotation of particle orientation vectors (a) $\hat{n}^x$, b) $\hat{n}^y$, (c) $\hat{n}^z$ and (d) particle enstrophy $\langle \omega_i' \omega_i' \rangle$.

Figure 2 shows the variance of the rate of rotation of the three particle orientation vectors together with the particle enstrophy in the channel center as a function of the two particle aspect ratios. The results for axisymmetric particles along the line $\lambda_1 = \lambda_2$ are consistent with recent results for inertial spheroids in the center of a channel flow reported by Zhao et al. (2015). The rotation rates of inertial particles are damped along all three principal axes as compared to the tracer particles shown in article 7. This has been reported for spheroidal particles by attributing to the different preferential alignment of inertial particles compared to tracer particles. Inertial triaxial ellipsoidal particle enstrophy shown in Figure 2(d) is dependent on the particle aspect ratios, which is different from the constant particle enstrophy observed for tracer particles.

Figure 3 shows the rate of rotation of the particle orientation vectors (tumbling rates) and the particle enstrophy at $z^+ = 10$. The particle enstrophy in Figure 3(d) is strongly damped as the particles become increasingly aspherical. Such damping effect of particle rotation can be ascribed to the well-known preferential particle orientation observed in the near-wall turbulence. The tumbling rates about the three particle axes in Figures 3(a, b, c) are distinctly different from those at the channel center in Figure 2(a, b, c).

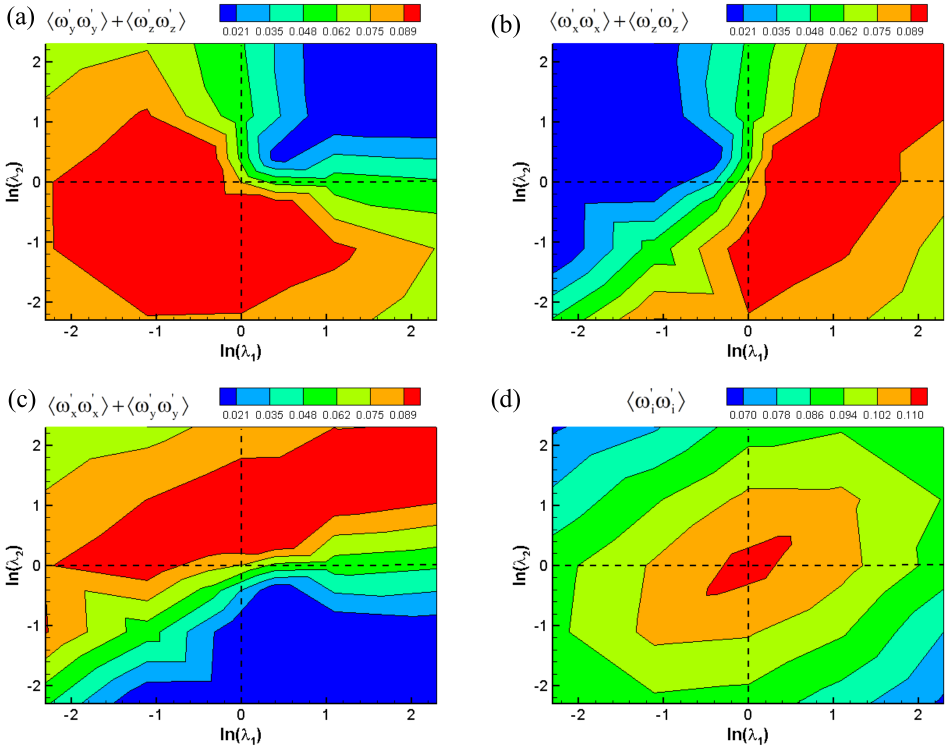

FIG. 3. Variance of tumbling and rotation rates in the near-wall region at $z^+ \approx 10$ normalized by the viscous time scale time (ν/u_τ^2). Rate of rotation of particle orientation vectors (a) $\hat{n}^x$, b) $\hat{n}^y$, (c) $\hat{n}^z$ and (d) particle enstrophy $\langle \omega_i' \omega_i' \rangle$.

REFERENCES

Brenner, H., 1964. The Stokes resistance of an arbitrary particle—IV Arbitrary fields of flow. Chemical Engineering Science 19, 703-727.

Challabotla, N.R., Zhao, L., Andersson, H.I., 2015. Orientation and rotation of inertial disk particles in wall turbulence. Journal of Fluid Mechanics 766, R2.

Jeffery, G.B., 1922. The Motion of Ellipsoidal Particles Immersed in a Viscous Fluid. Proceedings of the Royal Society of London. Series A 102, 161-179.

Mortensen, P.H., Andersson, H.I., Gillissen, J.J.J., Boersma, B.J., 2008. Dynamics of prolate ellipsoidal particles in a turbulent channel flow. Physics of Fluids 20, 093302.

Oberbeck, A., 1876. Ueber stationäre Flüssigkeitsbewegungen mit Berücksichtigung der inneren Reibung. Journal für die reine und angewandte Mathematik 81, 62-80.

Shapiro, M., Goldenberg, M., 1993. Deposition of glass fiber particles from turbulent air flow in a pipe. Journal of Aerosol Science 24, 65-87.

Zhao, L., Challabotla, N.R., Andersson, H.I., Variano, E.A., 2015. Rotation of Nonspherical Particles in Turbulent Channel Flow. Physical Review Letters 115, 244501.